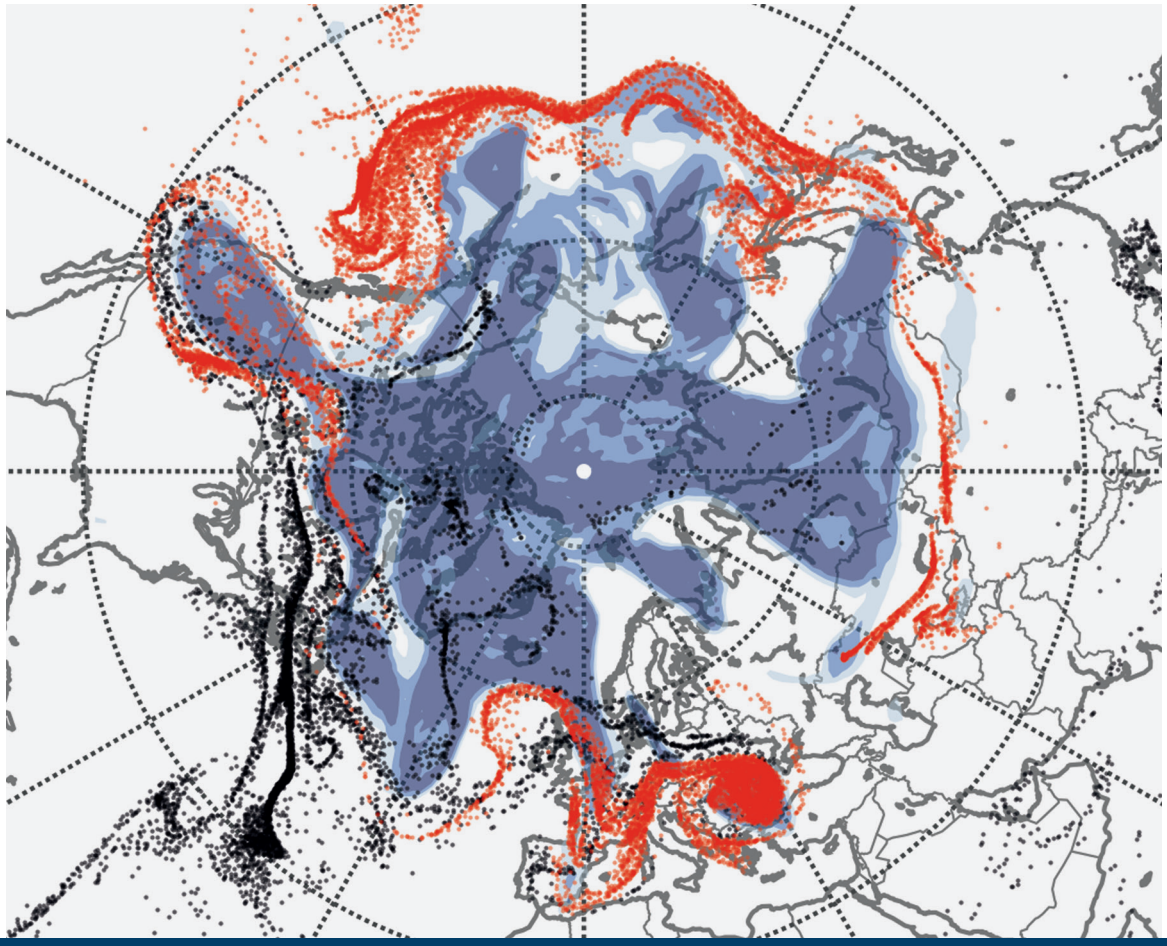

Examining transport in the Upper Troposphere – Lower Stratosphere with the infrared limb imager GLORIA

Lukas Krasauskas

Energie & Umwelt / Energy & Environment
Band / Volume 606
ISBN 978-3-95806-691-5

Mitglied der Helmholtz-Gemeinschaft

JÜLICH
Forschungszentrum

Schriften des Forschungszentrums Jülich
Reihe Energie & Umwelt / Energy & Environment Band / Volume 606

Forschungszentrum Jülich GmbH
Institut für Energie- und Klimaforschung (IEK)
Stratosphäre (IEK-7)

Examining transport in the Upper Troposphere – Lower Stratosphere with the infrared limb imager GLORIA

Lukas Krasauskas

Schriften des Forschungszentrums Jülich
Reihe Energie & Umwelt / Energy & Environment Band / Volume 606

ISSN 1866-1793 ISBN 978-3-95806-691-5

Bibliografische Information der Deutschen Nationalbibliothek.
Die Deutsche Nationalbibliothek verzeichnet diese Publikation in der
Deutschen Nationalbibliografie; detaillierte Bibliografische Daten
sind im Internet über http://dnb.d-nb.de abrufbar.

Herausgeber und Vertrieb:	Forschungszentrum Jülich GmbH Zentralbibliothek, Verlag 52425 Jülich Tel.: +49 2461 61-5368 Fax: +49 2461 61-6103 zb-publikation@fz-juelich.de www.fz-juelich.de/zb
Umschlaggestaltung:	Grafische Medien, Forschungszentrum Jülich GmbH
Druck:	Grafische Medien, Forschungszentrum Jülich GmbH
Copyright:	Forschungszentrum Jülich 2023

Schriften des Forschungszentrums Jülich
Reihe Energie & Umwelt / Energy & Environment, Band / Volume 606

D 468 (Diss. Wuppertal, Univ., 2023)

ISSN 1866-1793
ISBN978-3-95806-691-5

Vollständig frei verfügbar über das Publikationsportal des Forschungszentrums Jülich (JuSER)
unter www.fz-juelich.de/zb/openaccess.

Contents

List of Figures

List of Tables

Abstract

The Gimballed Limb Observer for Radiance Imaging of the Atmosphere (GLORIA) is an airborne infrared limb imager that can measure temperature and trace gas concentration data in the Upper Troposphere and Lower Stratosphere (UTLS) with high vertical resolution (upo to 200 m). In addition to standard 1-D retrievals, a unique 3-D data set can be obtained by flying around the observed air mass and performing a tomographic retrieval. Such data sets have high horizontal resolution (up to 20 km $\times$ 20 km) as well and can give insight into many important small-scale processes in UTLS, such as mixing, filamentation and internal gravity wave propagation.

A 3-D tomographic retrieval is a highly challenging and computationally expensive inverse modelling problem. It typically requires an introduction of some general knowledge of the atmosphere (regularisation) due to its underdetermined nature. The quality of 3-D data strongly depends on regularisation. In this thesis, a consistent, physically motivated (no ad-hoc parameters) regularisation scheme based on spatial derivatives of first order and Laplacian is introduced. As shown by a case study with synthetic data, this scheme, combined with newly developed irregular grid retrieval methods, improves both upon the quality and the computational cost of 3D tomography. It also eliminates grid dependence and the need to tune parameters for each use case. The few physical parameters required can be derived from in situ measurements and model data. Tests show that an 82% reduction in the number of grid points and a 50% reduction in total computation time, compared to previous methods, could be achieved without compromising results. An efficient Monte Carlo technique was also adopted for accuracy estimation of the new retrievals.

The new methods were used to analyse data from the WAVE Driven Isentropic Exchange (WISE) measurement campaign in 2017. A Rossby wave breaking event was observed with the GLORIA instrument during two research flights two days apart. Both standard 1-D retrievals and a 3-D tomographic retrieval of trace gas volume mixing ratios were applied. The tomographic retrieval revealed complex vertical structures in stratospheric tracers (ozone and nitric acid) with multiple vertically stacked filaments related to several previous Rossby wave breaking events. Many of those features could not otherwise be observed in such detail. With the help of backward trajectory calculations, much the observed tracer structure could be understood as stirring and mixing of air masses of tropospheric and stratospheric origins (age-of-air concept), but there were still unexpected aspects to this structure, such as the non-isentropic nature of filaments. Also, a strong nitric acid enhancement was observed just above the tropopause. It was demonstrated that lightning activity was a possible cause for this enhancement. Air masses that had been transported horizontally from low-latitude troposphere to high-latitude stratosphere were identified with air with tropospheric signatures. The 1-D retrievals showed signatures of enhanced mixing between stratospheric and tropospheric air near the polar jet with some transport of water vapour into stratosphere. In the late stage of the RW breaking event, air masses seen in the previously discussed flight were stretched to very thin filament (horizontal thickness was down to 30 km at some altitudes) containing air rich in stratospheric tracers. The air masses of the filament showed signatures of mixing, but the tracer structure observed as part of the 3-D tomographic retrieval was still traceable in the filament.

Kurzfassung

Der Gimballed Limb Observer for Radiance Imaging of the Atmosphere (GLORIA) ist ein flugzeuggetragener bildgebender Infrarot-Horizontsondierer, der Temperatur- und Spurengaskonzentrationsdaten in der oberen Troposphäre und unteren Stratosphäre (UTLS) mit hoher vertikaler Auflösung (bis zu 200 m) messen kann. Zusätzlich zu den standardmäßigen 1-D-Rekonstruktionen kann ein einzigartiger 3-D-Datensatz gewonnen werden, indem die beobachtete Luftmasse umflogen und eine tomographische Rekonstruktion durchgeführt wird. Solche Datensätze haben eine hohe horizontale Auflösung (bis zu 20 km $\times$ 20 km) und können einen Einblick in viele wichtige kleinräumige Prozesse in UTLS geben, wie z.B. Vermischung, Filamentierung und Schwerewellenausbreitung.

Die 3D-Tomographie ist ein äußerst anspruchsvolles und rechenintensives Problem der inversen Modellierung. Aufgrund ihrer unterbestimmten Natur erfordert sie in der Regel die Einführung eines gewissen Vorwissens (a priori) über die Atmosphäre (Regularisierung). Die Qualität der 3-D-Daten hängt stark von der Regularisierung ab. In dieser Arbeit wird ein konsistentes, physikalisch motiviertes (keine Ad-hoc-Parameter) Regularisierungsschema eingeführt, das auf räumlichen Ableitungen erster Ordnung und dem Laplace-Operator basiert. Wie eine Fallstudie mit synthetischen Daten zeigt, verbessert dieses Schema in Kombination mit neu entwickelten Methoden zur Gewinnung unregelmäßiger Gitter sowohl die Qualität als auch die Rechenkosten der 3D-Tomographie. Es beseitigt auch die Abhängigkeit von regelmäßigen Gittern und die Notwendigkeit, die Regularisierungs-Parameter für jeden Anwendungsfall anzupassen. Die wenigen erforderlichen physikalischen Parameter können aus in-situ-Messungen und Modelldaten abgeleitet werden. Tests haben gezeigt, dass die Anzahl der Gitterpunkte um 82% und die Gesamtrechenzeit um 50% im Vergleich zu früheren Methoden reduziert werden konnte, ohne dass die Ergebnisse beeinträchtigt wurden. Ein effizientes Monte-Carlo-Verfahren wurde auch für die Schätzung der Genauigkeit der neuen Rekonstruktionen umgesetzt.

Die neuen Methoden wurden zur Analyse von Daten aus der WAVE Driven Isentropic Exchange (WISE)-Messkampagne im Jahr 2017 verwendet. Während zweier Forschungsflüge im Abstand von zwei Tagen wurde mit dem GLORIA-Instrument ein Rossby-Wellenbrechen beobachtet. Es wurden sowohl standardmäßige 1-D-Rekonstruktionen als auch eine tomografische 3-D-Rekonstruktion für das Volumenmischungsverhältnis von verschiedenen Spurengasen durchgeführt. Die tomografische Auswertung ergab komplexe vertikale Strukturen in stratosphärischen Spurengasen (Ozon und Salpetersäure) mit mehreren vertikal gestapelten Filamenten, die mit mehreren früheren Rossby-Wellenbrech-Ereignissen in Verbindung stehen. Solche Strukturen konnten sonst nicht in diesem Detailgrad beobachtet werden. Mit Hilfe der inversen Modellierung konnte ein Großteil der beobachteten Spurengas-Struktur als Verwirbelung und Vermischung von Luftmassen troposphärischen und stratosphärischen Ursprungs identifiziert werden (Age-of-Air-Konzept), aber es gab immer noch unerwartete Aspekte, wie die nicht-isentrope Natur der Filamente. Außerdem wurde eine starke Salpetersäureanreicherung knapp oberhalb der Tropopause beobachtet. Es wurde nachgewiesen, dass Blitzaktivität eine mögliche Ursache für diese Anreicherung ist. Luftmassen, die horizontal von der Troposphäre der niedrigen Breiten in die Stratosphäre der hohen Breiten transportiert worden waren, wurden mit Luft mit troposphärischen Signaturen identifiziert. Die 1-D Daten zeigten Anzeichen für eine verstärkte Vermischung zwischen stratosphärischer und troposphärischer Luft in der Nähe des Polarjets beiWasserdampf in die Stratosphäre transportiert wurde. In der Spätphase des Rossby-Wellenbrechens wur-

den die Luftmassen, die bei dem zuvor beschriebenen Flug beobachtet wurden, zu einem sehr dünnen Filament gestreckt (die horizontale Dicke betrug in einigen Höhen weniger als 30 km), das Luft mit einem hohen Anteil an stratosphärischen Spurengasen enthielt. Obwohl die Luftmassen des Filaments Anzeichen von Vermischung aufwiesen, war die Spurengas-Struktur, die im Rahmen der 3-D-tomographischen Rekonstruktion beobachtet wurde, im Filament noch nachweisbar.

Chapter 1

Introduction

Air radiance spectroscopy is a very universal technique for observation of the atmosphere. The spectrum and intensity of infrared radiation emitted by an atmospheric trace gas depends strongly on temperature and the type of the gas (Figure 1.1b). Measuring in the part of the infrared spectrum, where the atmosphere is generally transparent, one can deduce both the temperature of the observed air parcel and concentrations of many of the constituent gases. As air-radiance measurements do not depend on solar radiation, these parameters can be acquired at any time of the day.

There are three basic observation geometries for infrared emission spectroscopy. The zenith sounders are ground or aircraft based instruments that look upwards, nadir sounders are typically satellite based and look vertically downwards. A limb sounder, on the other hand, is an aircraft or satellite based instrument that measures radiation coming from a direction close to the horizon. Due to the exponential profile of the density of the atmosphere, most of the air molecules encountered along each line of sight (LOS) are located around the lowest altitude point of that LOS, called the *tangent point* (see Figure 1.1a). Therefore, most of the air radiance reaching the instrument from a particular direction comes from $\approx$ 200km long, almost horizontal stretch of LOS around the tangent point, the entirety of which lies very close to the tangent point altitude. Limb sounder measurements are hence integrated mostly horizontally along viewing direction, in stark contrast to zenith and nadir sounders, that observe and integrate vertically. As a consequence, limb sounders have a much better

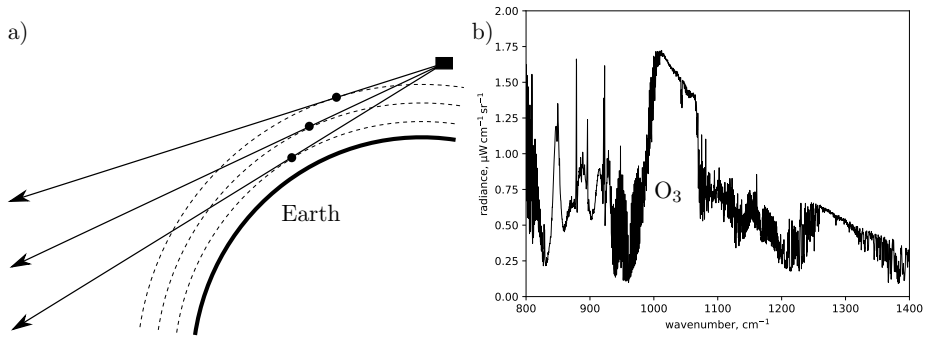

Figure 1.1: Panel a) – Limb observation geometry. Rectangle represents instrument, highlighted dots represent tangent points. Panel b) – air radiance spectrum recorded by the GLORIA instrument flying at the altitude of 12.8 km, with tangent point altitude of 10 km. The labelled spectral feature is due to O_3.

vertical resolution by design compared to the other two observation geometries. This makes them especially well suited for observing atmospheric features with rich vertical structure, such as trace gas concentrations and internal gravity waves. The downside of limb sounding is the poor (horizontal) resolution in the viewing direction, due to the horizontal integration mentioned above.

Infrared limb sounding has been successfully employed by a number of satellite instruments. They include the Limb Infrared Monitor for the Stratosphere (LIMS; Gille and Russel III, 1984) and Stratospheric and Mesospheric Sounder (SAMS; Drummond et al., 1980) that flew aboard the Nimbus 7 satellite from 1978 to 1994, the Cryogenic Limb Array Etalon Spectrometer (CLAES; Roche et al., 1993) that operated on board the Upper Atmosphere Research Satellite from 1991 to 2005, the Cryogenic Infrared Spectrometers and Telescopes for the Atmosphere instrument (CRISTA) that flew on board the Space Shuttle in 1994 and 1997(Offermann et al., 1999; Riese et al., 1999), the Michelson Interferometer for Passive Atmospheric Sounding (MIPAS) that flew on the ENVISAT satellite from 2002 to 2012 (Steck et al., 2005; Carlotti et al., 2001), the High Resolution Dynamics Limb Sounder (HIRDLS) that was operating on the Aura satellite from 2005 until 2008 (Gille et al., 2003) and the SABER (Sounding of the Atmosphere using Broadband Emission Radiometry; Mlynczak, 1997) instrument on the TIMED satellite operating since 2001. The high resolution global

data sets of temperature and a high number of trace gas concentrations provided by these missions had an important role in advancing research into the chemistry and dynamics of upper and middle atmosphere and gravity waves. Modified versions of the MIPAS and CRISTA instruments were also operated on research aircraft: the MIPAS-STR (Woiwode et al., 2012) and CRISTA-NF (Kullmann et al., 2004) instruments. They were well suited for observations of lower altitudes and higher resolution than their satellite counterparts.

In this work, we present data acquired by the Gimballed Limb Observer for Radiance Imaging of the Atmosphere (GLORIA) (Riese et al., 2014; Friedl-Vallon et al., 2014), which has been flying aboard the Russian M-55 Geophysica and the German High Altitude and Long Range Research Aircraft (HALO). GLORIA is an airborne imaging infrared spectrometer and a successor of both CRISTA-NF and MIPAS-STR. It employs a 2-D detector array and has the ability to be panned so that it can observe in the horizontal directions ranging from 45° to 132° with respect to carrier aircraft heading. Panning allows for a very large number of measurements in a wide variety of directions to be taken along the flight path. GLORIA can be used to retrieve temperature and volume mixing ratios of a number of tracers, including ozone, water vapour, nitric acid (HNO_3), trichlorofluoromethane (CFC-11), chlorine nitrate ($ClONO_2$), and peroxyacetyl nitrate (PAN) among others. The vertical resolution of best GLORIA retrievals is about 0.25 km, and best possible resolution in the two horizontal directions reaches 20 km $\times$ 20 km in the case of 3-D retrieval discussed below.

Reconstructing atmospheric quantities from limb sounder measurements is, in general, a complex inverse modelling problem. A typical approach used for most limb sounders combines the measurements taken from the same (or similar) location and azimuth with different elevations to retrieve a vertical atmospheric profile of, e.g., trace gas species. The early work used the so-called *onion-peeling* technique (e.g. Russell and Drayson, 1972), which is based on retrieving atmospheric quantities at the highest of the observed altitudes first, and then using this data for retrievals at the lower altitudes. This method is very computationally efficient, but prone to instabilities, especially at the higher levels (Rodgers, 2000). It led to adoption of the more robust Tikhonov regularisation (Tikhonov and Arsenin, 1977). Data products obtained from such one-dimensional retrievals have good sampling in the vertical

direction and the horizontal direction perpendicular to the LOS. Resolution along line of sight is much poorer (e.g. von Clarmann et al., 2009). One of the ways to improve this, is to adopt a tomographic approach, i.e., to combine several measurements of the same air mass taken from different directions. This is easiest to achieve for satellites that measure in their orbital plane. They end up sampling the same air parcels from different points in their orbits with different observation elevations. A set of such measurements can be combined to perform a 2-D tomographic retrieval (e.g. Carlotti et al. 2001 for MIPAS, Livesey and Read 2000 for the Microwave Limb Sounder). For the GLORIA airborne limb sounder, which generally looks to the side of the flight path, multiple observations of the same air mass can be realised with the help of instrument panning or, for best results, by flying the aircraft around the air volume to be observed while panning. The measurements then have to be combined in three dimensions to improve the horizontal resolution along the line of sight, which makes such a tomographic retrieval a very complex mathematical problem. The lines of sight in different directions span a huge volume , only a small part of which has tangent points and can hence be well-resolved. Two major issues arise here. Firstly, a problem of retrieving atmospheric quantities in such a large volume from the measurements is mathematically highly underdetermined. Additional information based on prior (i.e. not coming from GLORIA measurements) knowledge about the atmosphere has to be introduced into the retrieval using the mathematical technique called *regularisation*. The quality of the retrieval depends strongly on the choice of regularisation. A 3-D retrieval based on Tikhonov regularisation scheme was developed by Ungermann et al. (2010b, 2011), using some concepts originally employed for seismology (Nolet, 1985). This technique serves the purpose of ruling out very pathological, oscillatory retrieval results, but requires fine tuning of several unphysical ad-hoc parameters and subsequent validation. This is both labour intensive and computationally expensive (many test runs of the retrieval just to optimise regularisation). Furthermore, the use of unphysical parameters can often restrict the retrieval to very simple regularisation schemes, as more complex and potentially more effective ones need too much hand-tuning and optimisation. The second major issue with 3-D retrieval is its computational cost. To make use of the instrument potential to deliver high resolution, the grid used to represent the atmosphere in the retrieval must be dense in

all three dimensions (at least in the regions where the best instrument resolution is available), and at the same time cover large volumes mentioned earlier. Using a regular grid over the whole volume is completely infeasible, but even employing variable-density ordered grids results in up to 10^6 grid points. The amount of radiances measured by GLORIA for such 3-D tomography case is also in excess of of 10^6, some of the matrices needed for calculations are larger than $10^6 \times 10^6$ as a result. Dealing with problems of this size is only possible by, among other techniques, exploiting matrix sparsity[1] and using efficient iterative methods for equation solving, e.g. conjugate gradients (Ungermann et al., 2010a). Even then computing clusters (often called supercomputers) are still required to perform tomography, as more usual stand-alone computers have neither sufficient memory, nor the computing power. At the start of the work described in this thesis, the resolution of tomographic retrievals was in many cases limited by the available computing resources on supercomputers, which reduced our ability to study the very finest structures observable by GLORIA, such as short internal gravity waves or thin trace gas filaments. Addressing the two issues of a tomographic retrieval discussed here constitutes a large part of this thesis (see below the list of main questions of the thesis for more details).

GLORIA is mostly used for observing the Upper Troposphere – Lower Stratosphere (UTLS) region. This region is heavily influenced by both stratospheric and tropospheric air masses and is characterised by sharp gradients in tracer volume mixing ratios, many of which GLORIA can measure with much better resolution than satellite based instruments. The composition of the UTLS plays a key role in stratosphere-troposphere exchange (STE) (e.g. Gettelman et al., 2011), has a large effect on radiative forcing (e.g. Forster and Shine, 1997; Riese et al., 2012) and hence climate change and variability. Rossby wave (RW) activity in general is one of the major processes that shapes the dynamics and structure of UTLS (Salby, 1984). It is known to steepen the tracer gradients and act as a horizontal transport barrier (McIntyre and Palmer, 1983, 1984) and facilitate STE (Waugh et al., 1994; Günther et al., 2008). The tendency of RW breaking events to create complex spatial distributions of tracers, such as very thin filamentary structures, has been known for some time both from theoretical

[1] A matrix is called *sparse* if most of its elements are zero.

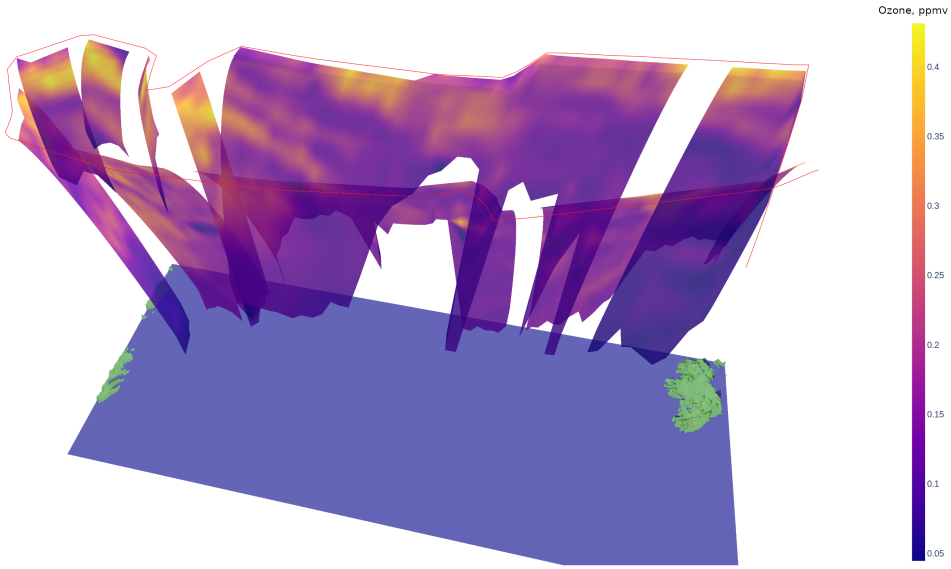

Figure 1.2: Visualisation of 2-D ozone data product (data from 1-D retrievals along flight path) for WISE campaign flight, 7 October 2017. Note the curved surface on which ozone concentration is retrieved. Tangent points of observations lie on this surface, which extends from $\sim$6 km to $\sim$14 km altitude. Hexagonal flight pattern in the west was flown for 3-D tomography (not shown here).

work (Polvani and Plumb, 1992; Scott and Cammas, 2002) and studies combining modelling with in situ aircraft measurements (e.g. Waugh et al. 1994, Kunkel et al. 2019) or satellite data (Bacmeister et al., 1999; Pan et al., 2009). Observing these events remains very challenging: satellite instruments have global coverage, but typically lack resolution (vertical resolution in the UTLS is particularly problematic) for the characteristically small scales involved in wave breaking, while in situ observations from aircraft are very highly resolved and accurate, but their spatial coverage is limited to the flight path of the carrier aircraft.

Aircraft-based limb sounders provide the very attractive middle ground between satellites and in situ with better resolution than the former and much better spatial coverage than the latter. They are typically used to acquire a set of atmospheric profiles along the aircraft flight path that can be subsequently retrieved and combined into a data set on a 2-D slice of the atmosphere. For instance, the CRISTA-NF limb sounder aboard the Geophysica research

aircraft provided 2-D data products of multiple tracer volume mixing ratios with vertical resolution of ≈0.5 km and horizontal sampling of ≈12.5 km (Kullmann et al., 2004). It was used, among other scientific objectives, to observe filaments in UTLS after Rossby wave breaking near the subtropical jet (Weigel et al., 2010; Ungermann et al., 2013). GLORIA offers further-improved vertical resolution and, most importantly, the qualitatively new 3-D data sets. Filamentation and mixing are inherently 3-D processes, their full analysis requires resolving the dimensions of features in all spatial directions. These are immediately available when working with 3-D data, while in situ data often involves complex theory or model based argumentation to compensate for the sparse measurements.

In this thesis, a 3-D tomography-based case study of RW breaking is presented (Chapter 4). The observations introduced there were made as part of Wave Driven Isentropic Exchange (WISE) measurement campaign in Shannon, Ireland in September-October 2017. Two flights on 7 and 9 October observed different stages of a RW breaking event.

The methodical part of the thesis (Chapters 2 and 3) aims to address the following two questions (based on the material published in Krasauskas et al., 2019):

- **What effect does the regularisation have on retrieval results? How can one ensure that this effect comes from physically meaningful assumptions, rather than ad-hoc mathematical manipulations?**

  We aim to develop regularisation with parameters that are physical quantities obtainable from in situ observations, model data and theoretical considerations. It can then be used both to simplify the retrieval parameter determination and enable the use of more complex regularisation schemes. Physical parameters are also grid independent, which allows them to be directly compared between different retrieval resolutions or different case studies, decreasing the work needed for regularisation optimisation even further and eliminating some of the effects that retrieval grid might have on the results. These novel methods are developed in Section 2.2. The new regularisation parametrisation framework also allows to combine differential operators of first and second order, which helps to improve the retrieved data quality (Chapter 3).

- **Can the computational cost of tomographic retrieval be reduced by using irregular grids?**

  Reducing the number of grid points as far as possible, while maintaining high resolution where it is required, is crucial for keeping the computational costs of retrieval at a feasible level. Generally, limb sounders achieve highest resolution in areas with the highest tangent point density. For 1-D retrievals, this fact is exploited very directly by simply placing the retrieval grid points at the tangent points. Such a grid results in the retrieved profile not being a vertical line (see Figure 1.1 or 1.2), and representing instead the true locations where the most of the information acquired by the limb sounder comes from. Such tangent point grids are not possible in 3-D, since one cannot adequately represent the 3-D structure of atmospheric quantities with their values at tangent points only. Before the work described in this thesis started, rectilinear[2] grids were used to process GLORIA 3-D data. The main idea in their use is to make grid density higher where the tangent point density is high, but still having a good representation of atmospheric structures irrespective of their shape or orientation. However, rectilinear grids are still very limiting and, in the case of GLORIA 3-D tomography, result in many unnecessary points, e.g. at high altitudes above tangent point-rich areas. Irregular grids were not used so far because the mathematical methods required to deal with them in this context are a lot more complex that those for ordered grids. Developing irregular grid differentiation algorithms that would not introduce unacceptable amounts of retrieval noise proved to be particularly challenging. A working irregular grid implementation (Section 2.3) was developed nevertheless, and validated against the old, less computationally efficient techniques (Chapter 3).

The scientific part of the thesis (Chapter 4) aims to address the following questions:

- **What is the 3-D distribution of air masses of stratospheric and tropospheric origin around the polar jet? How is it affected by Rossby wave breaking?**

[2]Rectilinear grid in Cartesian coordinates (x, y, z) is defined by taking a set of x values, a set of y values and a set of z values and placing a grid point at any possible combination of the three

Can this distribution be understood from the perspective of stratosphere-troposphere exchange (STE) and known dynamical processes?

The tomographic retrieval of an air mass in a Rossby wave breaking region near the polar jet acquired as part of the WISE measurement campaign on 7 October 2017 is presented in Chapter 4 and studied in detailed with the help of backward trajectory analysis. This region of UTLS is known for particularly complex structure, existing measurements there are lacking either in spatial coverage, or vertical resolution, or both. GLORIA 3-D data products of stratospheric tracer (ozone, nitric acid) volume mixing rations provide detailed insights into stirring and mixing between air masses of stratospheric and tropospheric origin, that can then be compared to backward trajectory data.

- **How strong are the mixing processes in the UTLS around the polar jet? How are they influenced by Rossby wave breaking?**

  The GLORIA data from the WISE campaign measurement flights on 7 and 9 October 2017 is presented in Chapter 4. These flights were designed to capture the same air masses in different stages of the breaking event. In situ observations were only moderately successful in that, as it is very difficult to match exactly the same potential temperature level with the aircraft. GLORIA provides a larger altitude range below flight altitude. An air mass of stratospheric origin was observed before and after it had been stretched into a thin filament. Tracer-tracer correlations from different regions and different stages of Rossby wave breaking were examined in detail to identify mixing regions and extent.

The structure of the thesis is as follows. The introduction is followed by Chapter 2, which deals with the theory of 3-D tomography. The first section of the chapter introduces the reader to the inverse modelling approach to remote sensing retrievals and outlines some of its main challenges. The subsequent sections introduce newly developed methods for 3-D tomography. These methods are then put to the test in Chapter 3, where 3-D tomographic retrieval with simulated measurements is used to validate the new techniques and compare them to current

state-of-the-art. Finally, the new methods are put to real use in Chapter 4, which contains the full scientific evaluation of two research flights of the WISE measurement campaign.

Chapter 2

Principles of 3-D tomographic retrievals

This chapter presents the theoretical background and mathematical methods required to derive 3-D tomographic data products from limb sounder measurements. A novel regularisation method based on exponential covariance is introduced as well as newly developed methods for working with irregular grids. They enable highly-resolved 3-D tomography at significantly reduced computational cost, compared to established techniques, as well as a flexible, physically motivated (as opposed to previous trial-and-error based approaches) method to set regularisation parameters. The final section introduces computationally efficient Monte Carlo based diagnostics calculation technique and develops numerical methods needed to apply it to 3-D problems. This chapter is mostly based on the results published in Krasauskas et al. (2019).

2.1 Inverse modelling for atmospheric measurements

This section outlines the general inverse modelling approach and its main challenges. The issues that will be addressed in detail in this thesis are briefly outlined in the end of the section.

Let the vector $\boldsymbol{y} \in \mathbb{R}^m$ be a set of m remote measurements taken with a remote sensing

instrument, and let vector $\boldsymbol{x} \in \mathbb{R}^n$, the *atmospheric state vector*, represent the values of some atmospheric quantities on a finite grid. It is natural to represent the measurements as a set of discrete values, because that is how the instrument records them. The atmospheric state could also be represented as a continuum (i.e. a set of several functions $g_i : V \to \mathbb{R}$ representing physical quantities, where $V \subset \mathbb{R}^3$ is some volume in the atmosphere), which we will do in the subsequent sections, where it is advantageous for analytical calculations and preserving generality of the results. In practise, however, large inverse modelling problems generally require numerical calculations, and dealing with discrete representation is inevitable at some stage, so we choose to introduce it from the beginning.

The goal of the measurement data *retrieval* is to obtain the atmospheric state $\boldsymbol{x}$ from the measurements $\boldsymbol{y}$. In remote sensing, it is typically very hard or impossible to develop a direct deterministic physical model $B : \mathbb{R}^m \to \mathbb{R}^n$, $\boldsymbol{y} \mapsto \boldsymbol{x}$ that would obtain $\boldsymbol{x}$ from $\boldsymbol{y}$, but it is much easier to develop a *forward model* $F : \mathbb{R}^n \to \mathbb{R}^m$, $\boldsymbol{x} \mapsto \boldsymbol{y}$ that models the measurement process obtaining $\boldsymbol{y}$ given $\boldsymbol{x}$. Although the particular problems in developing these models would differ from instrument to instrument, there are several general reasons why the forward model approach is easier to implement. Firstly, if one knows the state of a physical system that emits a signal, one can usually determine what signal was emitted in a non-ambiguous manner, but the same signal could be emitted in multiple states. Secondly, remote sensing instruments typically detect a superposition of multiple signals coming from multiple source locations. In the forward model, generation and propagation of each signal can usually be modelled separately, and then their superposition at the measurement apparatus can be worked out. Obtaining individual signals for each superposed state based on their superposition is most often very difficult or impossible.

Therefore, remote sensing data retrievals are often performed using the *inverse modelling* approach. Its main idea is to develop a forward model $\boldsymbol{F} : \mathbb{R}^n \to \mathbb{R}^m$, $\boldsymbol{x} \mapsto \boldsymbol{y}$ that contains all (or almost all) the necessary physics of the problem, and then develop a mathematical algorithm that will use $\boldsymbol{F}$ to solve the *inverse problem*, i.e. determine the atmospheric state $\boldsymbol{x}$ from measurement $\boldsymbol{y}$. The inverse modelling step can make use of the relevant statistics of the atmospheric states, but there are typically no direct physical calculations necessary.

In the case of an ideal measurement, the inverse problem would be reduced to inferring $\boldsymbol{x}$ from $F(\boldsymbol{x}) = \boldsymbol{y}$. The real measurements are, however, subject to errors. If we represent the combined error of the measurement and the forward model by the unknown vector $\boldsymbol{\epsilon} \in \mathbb{R}^m$, the inverse problem can be written as

$$F(\boldsymbol{x}) = \boldsymbol{y} + \boldsymbol{\epsilon} \tag{2.1}$$

This cannot be directly solved as an equation, because such an equation would be, in general, ill-posed.[1] There are two issues that prevent it from being well-posed. Firstly, with a fixed value of $\boldsymbol{\epsilon}$, it may not have a solution. If $\boldsymbol{y}_{\mathrm{id}} \in \mathbb{R}^m$ represents the (unknown) true signal that the instrument is trying to measure, then, by construction of the problem, $\exists\, \boldsymbol{x} \in \mathbb{R}^n$ such that $F(\boldsymbol{x}) = \boldsymbol{y}_{\mathrm{id}}$, but if we replace $\boldsymbol{y_{id}}$ with the real, finite-precision measurement $\boldsymbol{y}$ this will not necessarily be true. We could remedy this by assuming that the likeliest value of $\boldsymbol{\epsilon}$ is 0, and large errors are increasingly less likely. Then we can solve for the likeliest value of $\boldsymbol{x}$, i.e. $\boldsymbol{x}$ that minimises

$$\min_{\boldsymbol{x}} \|F(\boldsymbol{x}) - \boldsymbol{y}\| \tag{2.2}$$

The second problem, which applies to both equation (2.1) and (2.2), is that the solution might not be (and usually is not) unique. If practise, this issue is usually not limited to having a few similar solutions to choose from. The expression (2.2) can often be minimized by a large variety of radically different atmospheric states $\boldsymbol{x}$, most of which are completely unphysical. This happens because remote sensing measurements $\boldsymbol{y}$, taken separately from any other knowledge we might have, are not sufficient to determine the atmospheric state $\boldsymbol{x}$. External information about $\boldsymbol{x}$ needs to be introduced into retrieval to pick a reasonable solution. One of the ways of doing that is introducing an *a priori* atmospheric state $\boldsymbol{x}_{\mathrm{apr}}$ which represents the best of our knowledge about the atmosphere before the measurement was performed. In the case of atmospheric measurements, one could obtain such a state from a suitable climatology or model data. One could then proceed in a manner similar to the way

[1] In mathematical physics, a problem is well-posed if it has a unique solution, and this solution is stable, i.e. if the vectors $\boldsymbol{a}_1$ and $\boldsymbol{a}_2$ represent input parameters of the problem, and the vectors $\boldsymbol{x}_1$ and $\boldsymbol{x}_2$ represent the corresponding results, then $\lim_{\boldsymbol{a}_1 \to \boldsymbol{a}_2} \boldsymbol{x}_1 = \boldsymbol{x}_2$; otherwise the problem is ill-posed.

we handled the measurement error: we assume that before the measurement the most likely $\boldsymbol{x}$ value was $\boldsymbol{x}_{\text{apr}}$, and that $\boldsymbol{x}$ values get increasingly unlikely as they get further from *a priori*, so the likeliest of all values that minimise (2.2) would minimise

$$\min_{\boldsymbol{x}} \|\boldsymbol{x} - \boldsymbol{x}_{\text{apr}}\| \tag{2.3}$$

One must also take into account that, in general, not all the measurements might be equally noisy, some might be correlated. Also, various atmospheric parameters, such as temperature, pressure or trace gas concentrations are almost certainly correlated between the neighbouring grid points. Therefore, we cannot restrict ourselves to Euclidean norms in equations (2.2) and (2.3), a more general approach is needed. One would also like to cast the problem in a form that would make it tractable for large-scale numerical calculations. One can achieve these goals as follows. Let us treat $\boldsymbol{x}$ as random vector with mean $\boldsymbol{x}_{\text{apr}}$ and covariance given by the real symmetric positive definite *covariance matrix* $\mathbf{S}_{\text{a}}$ (i.e. the matrix with components $\{\mathbf{S}_{\text{a}}\}_{ij} = \{\mathbf{S}_{\text{a}}\}_{ji} = \text{cov}\,(\boldsymbol{x}_i, \boldsymbol{x}_j)$. Then the entropy of $\boldsymbol{x}$ is maximised when it has multivariate normal distribution (proved e.g. by Tarantola, 2013). Hence by treating $\boldsymbol{x}$ as a random vector with this distribution, we impose the smallest restriction possible while still introducing external information into the retrieval by means of the covariance matrix $\mathbf{S}_{\text{a}}$. Also, the probability density of $\boldsymbol{x}$ is then

$$f_{\boldsymbol{x}}\left(\hat{\boldsymbol{x}}\right) \sim \exp\left(-\frac{1}{2}\left(\hat{\boldsymbol{x}} - \boldsymbol{x}_{\text{apr}}\right)^T \mathbf{S}_{\text{a}}^{-1}\left(\hat{\boldsymbol{x}} - \boldsymbol{x}_{\text{apr}}\right)\right) \tag{2.4}$$

Here and later on "$\sim$" denotes proportionality, as we have not normalised the probability density function. If we now assume that the forward model is exact, we can similarly introduce a random vector $\boldsymbol{y}$ with mean $\boldsymbol{F}(\boldsymbol{x})$ and covariance matrix $\mathbf{S}_{\epsilon}$, and its probability density would then be

$$f_{\boldsymbol{y}}\left(\hat{\boldsymbol{y}}\right) \sim \exp\left(-\frac{1}{2}\left(\hat{\boldsymbol{y}} - \boldsymbol{F}\left(\boldsymbol{x}\right)\right)^T \mathbf{S}_{\epsilon}^{-1}\left(\hat{\boldsymbol{y}} - \boldsymbol{F}\left(\boldsymbol{x}\right)\right)\right) \tag{2.5}$$

By Bayes' theorem, the a posteriori probability density of $\hat{\boldsymbol{x}}$ given the measurement $\hat{\boldsymbol{y}}$ is

$$f_{\boldsymbol{x}|\boldsymbol{y}}\left(\hat{\boldsymbol{x}}\right) = \frac{f_{\boldsymbol{x}}\left(\hat{\boldsymbol{x}}\right)\, f_{\boldsymbol{y}|\hat{\boldsymbol{x}}=\boldsymbol{x}}\left(\boldsymbol{y}\right)}{\int f_{\boldsymbol{x}}\left(\boldsymbol{u}\right) f_{\boldsymbol{y}|\hat{\boldsymbol{x}}=\boldsymbol{u}}\left(\boldsymbol{y}\right) \mathrm{d}\boldsymbol{u}} \sim \exp\left(-\frac{1}{2} J\left(\hat{\boldsymbol{x}}\right)\right) \tag{2.6}$$

where

$$J\left(\boldsymbol{x}\right) = \left(\boldsymbol{y} - \boldsymbol{F}\left(\boldsymbol{x}\right)\right)^T \mathbf{S}_\epsilon^{-1} \left(\boldsymbol{y} - \boldsymbol{F}\left(\boldsymbol{x}\right)\right) + \left(\boldsymbol{x} - \boldsymbol{x}_{\mathrm{apr}}\right)^T \mathbf{S}_{\mathrm{a}}^{-1} \left(\boldsymbol{x} - \boldsymbol{x}_{\mathrm{apr}}\right) \tag{2.7}$$

We can now solve the inverse problem, i.e. find the most likely atmospheric state $\boldsymbol{x}$ given measurement $\boldsymbol{y}$, by minimising $J\left(\boldsymbol{x}\right)$. In principle, given a forward model $\boldsymbol{F}$, a priori $\boldsymbol{x}_{\mathrm{apr}}$, and explicit expressions of $\mathbf{S}_\epsilon^{-1}$ and $\mathbf{S}_{\mathrm{a}}^{-1}$, one can tackle (2.7) numerically with the help of a suitable iterative minimisation algorithm. In this work we will make use of the iterative solver for (2.7) integrated into the Jülich Rapid Spectral Simulation Code Version 2 (Ungermann et al., 2010b, 2011, JURASSIC2). It is based on the Levenberg-Marquardt (Marquardt, 1963) algorithm for iteration and conjugate gradients solver (Hestenes and Stiefel, 1952) for the linear equation systems that need to be solved within each iteration. Retrieval can typically be performed in no more than 5 Levenberg-Marquardt iterations. The conjugate gradient algorithm has the computational cost of $O(N^2)$ per iteration, and usually obtains a solution in much less than N iterations for a square linear equation system with N unknowns. These methods also speed up significantly in practice if working with sparse matrices (i.e. matrices that have very small proportion of non-zero entries). They share a common feature of avoiding costly matrix-matrix multiplication entirely and relying solely on vector-vector and matrix vector multiplications.

Equation (2.7) is an important result and several variations thereof are found in many works on inverse modelling (Rodgers, 2000; Tarantola, 2013; Tikhonov and Arsenin, 1977, e.g.) with slightly differing approaches to derivation. The derivation presented here is often called the Bayesian interpretation, because of the probabilistic interpretation of $J\left(\boldsymbol{x}\right)$ by means of Bayesian inference. It solves the problems of $\boldsymbol{F}\left(\boldsymbol{x}\right) = \boldsymbol{y}$ not having an exact solution and the approximate solutions being not unique. However, the quality of the solution, as well as the computational cost of solving (2.7) depend heavily on the choice of the *precision matrices*[2]

[2]Precision matrix is defined as an inverse of a covariance matrix

$\mathbf{S}_\epsilon^{-1}$ and $\mathbf{S}_\mathrm{a}^{-1}$.

$\mathbf{S}_\epsilon^{-1}$ represents the statistics of the measurement errors and is therefore means of providing information about the instrument to the inverse modelling framework. More details about $\mathbf{S}_\epsilon^{-1}$ used in this work can be found in Section 3.1. $\mathbf{S}_\mathrm{a}^{-1}$ is one way to introduce a priori information about the atmosphere into the retrieval. For example, one of the most important qualities of a plausible atmospheric state, which is often not present in unphysical solutions of (2.1), is the spatial continuity or smoothness of atmospheric parameters; i.e. the values of an atmospheric parameter (e.g. temperature) are strongly positively correlated for two grid points that are close to each other. Such correlations are represented by the off-diagonal terms of $\mathbf{S}_\mathrm{a}$. Constructing a suitable $\mathbf{S}_\mathrm{a}^{-1}$ therefore requires some kind of statistical model for the atmosphere or an alternative interpretation of (2.7). This issue will be discussed in detail in Section 2.2.2.

The tomographic retrievals discussed in this work are typically large, with $\boldsymbol{x}$ and $\boldsymbol{y}$ having $10^5 - 10^6$ elements. Computational cost of many common mathematical operations becomes prohibitively large for such problems. For example, explicit inversion of a $10^6 \times 10^6$ matrix requires $O\left(10^{18}\right)$ operations and is hence unfeasible. We need to restrict ourselves to vector addition, vector-vector multiplication and matrix-vector multiplication where the matrix is ideally sparse for such large problems, much like in the solution of (2.7) itself. Our precision matrices $\mathbf{S}_\epsilon^{-1}$ and $\mathbf{S}_\mathrm{a}^{-1}$ must therefore be constructed directly, rather than by inversion of the corresponding covariance matrix, and be sparse.

Finally, to express $\boldsymbol{x}$, and $\boldsymbol{x}_\mathrm{apr}$ as vectors, an efficient way of discretising an atmospheric volume has to be found and algorithms for calculating the necessary mathematical operations (volume integrals, derivatives, etc.) on this grid have to be worked out. Ordered grids simplify some of the required calculations, but the restrictions they impose on grid point placement often result in many grid points being placed where they are not actually needed, thus wasting computational resources. In this work, the methods required for working with completely unrestricted, irregular grids are developed (Section 2.3.1) and the resulting reductions in the processing time and memory consumption are demonstrated.

2.2 Regularisation

Subsection 2.2.1 further explains the motivation behind the second term for the equation (2.7), often called the *regularisation term*, and several popular approaches for its explicit evaluation. The advantages and shortcomings of the different methods are discussed and the approach chosen for the tomographic retrievals in this thesis, which is based on exponential covariance in the atmosphere, is outlined there. Subsection 2.2.2 then shows in detail how the regularisation term can be evaluated in the case of exponential covariance function.

2.2.1 Regularisation methods and motivation

Recall that in the previous section we made the assumption that the atmospheric state vector $\boldsymbol{x}$, if treated as a random variable, had mean $\boldsymbol{x}_{\mathrm{apr}}$ and covariance $\mathbf{S}_{\mathrm{a}}$. Then, based on maximum entropy criterion, we further assumed that it has multivariate normal distribution. If we could find such $\boldsymbol{x}_{\mathrm{apr}}$ and $\mathbf{S}_{\mathrm{a}}$ for which the two assumptions were highly accurate, the equation (2.6) would give the correct probability density for $\boldsymbol{x}$, thus providing a very complete solution for the inverse problem. This approach is called *optimal estimation* (Rodgers, 2000) and is often used in inverse modelling. If, however, one wants to perform high resolution 3-D retrievals in the atmosphere, like those of the GLORIA limb sounder, the existing climatologies and model data sets are not highly resolved enough to calculate the full covariance of the distribution of atmospheric states $\boldsymbol{x}$. It is also not clear to what accuracy this distribution would actually resemble the multivariate normal distribution, or how to maintain reasonable computational cost while using a highly complex covariance relation. Therefore, we treat $\mathbf{S}_{\mathrm{a}}$ as a rough approximation of the covariance of the atmosphere instead and make no claims that (2.6) gives the correct probability density. Instead, we just expect our simple covariance relation to deliver a plausible most likely state $\boldsymbol{x}$ close to the real optimal solution that could in theory be found having full knowledge of the statistics of the atmosphere.

Another popular method to construct $\mathbf{S}_{\mathrm{a}}^{-1}$ is called *Tikhonov regularisation* (Tikhonov and Arsenin, 1977). It adopts a more utilitarian interpretation of equation (2.7). In the same formalism as before, a solution of the inverse problem with Tikhonov regularisation could be

written as

$$J(\boldsymbol{x}) = \|\boldsymbol{F}(\boldsymbol{x}) - \boldsymbol{y}\|^2 + \|\boldsymbol{\Gamma}(\boldsymbol{x} - \boldsymbol{x}_{\text{apr}})\|^2, \tag{2.8}$$

which can be viewed as (2.7) with $\mathbf{S}_\epsilon^{-1} = \mathbf{I}$ (the identity matrix), and $\mathbf{S}_\text{a}^{-1} = \boldsymbol{\Gamma}^T\boldsymbol{\Gamma}$, where $\boldsymbol{\Gamma}$ is the Tikhonov matrix. In the Tikhonov approach, minimisation of $J(\boldsymbol{x})$ can be regarded as joint minimisation of the two terms in the right-hand side of equation (2.8), where minimising the first term ensures that $\boldsymbol{x}$ matches the observations, and minimising the second term, often called the *regularisation term*, suppresses solutions with unwanted properties. These properties are determined by the choice of $\boldsymbol{\Gamma}$. If one wishes to ensure simply that $\boldsymbol{x}$ is sufficiently close to $\boldsymbol{x}_{\text{apr}}$ in an Euclidean sense, one can just choose $\Gamma = \alpha\mathbf{I}$, with the *regularisation parameter* $\alpha \in \mathbb{R}$ chosen ad-hoc, usually by trial-and-error. If one wants to ensure spatial continuity of physical quantities represented by $\boldsymbol{x}$, one can choose a difference operator as (part of) $\boldsymbol{\Gamma}$. As an example, consider a state vector $\boldsymbol{x}$ that represents a single physical quantity f on a regular rectangular grid with vertical grid constant h_z, and label the components of $\boldsymbol{x}$ according to locations of the grid points, i.e. $x_{\boldsymbol{r}} = f(\boldsymbol{r})$. Also let $\boldsymbol{e}_x$, $\boldsymbol{e}_y$, $\boldsymbol{e}_z$ be an orthonormal set of vectors with $\boldsymbol{e}_z$ vertical. Then the vertical difference operator can be written in matrix for as

$$\{\mathbf{L}_z\}_{\boldsymbol{r}\boldsymbol{r}'} = \frac{1}{h_z}\begin{cases} 1 & \boldsymbol{r} = \boldsymbol{r}' \notin \partial V \\ -1 & \boldsymbol{r}' - \boldsymbol{r} = h_z\boldsymbol{e}_z \\ 0 & \text{otherwise} \end{cases} \tag{2.9}$$

where ∂V denotes the upper grid boundary. One can define analogous operators in x and y directions similarly. Different regularisation operators could then be combined, like in the following example,

$$\mathbf{S}_\text{a}^{-1} = \boldsymbol{\Gamma}^T\boldsymbol{\Gamma} = \alpha_0^2\mathbf{I} + \alpha_h^2\mathbf{L}_x^T\mathbf{L}_x + \alpha_h^2\mathbf{L}_y^T\mathbf{L}_y + \alpha_v^2\mathbf{L}_z^T\mathbf{L}_z \tag{2.10}$$

to rule out all $\boldsymbol{x}$ that are discontinuous or strongly divergent from $\boldsymbol{x}_{\text{apr}}$. α_0, α_v and α_h are real parameters analogous to α used before. Note that we have used the same regularisation parameter α_h for both horizontal directions, but the typical length scales in the atmosphere

are very different in vertical and horizontal, hence a separate parameter α_v is needed.

The Tikhonov regularisation described above is relatively easy to implement, it results in a sparse $\mathbf{S}_{\mathrm{a}}^{-1}$ allowing fast evaluation of $J(\boldsymbol{x})$ and it serves the purpose of ruling out many unphysical solutions. On the other hand, direct application of this regularisation has some important disadvantages for the work described in this thesis. Firstly, explicit construction of difference operators is easy on regular rectangular grids (as shown by the simple example (2.9)), and it is not difficult to extend the same ideas to many other ordered grids (e.g. rectilinear grid, grids based on spherical coordinates), but a more constructive approach is required for dealing with the irregular grid that we intend to use. Secondly, the constants α_0, α_v and α_h are grid-dependent and do not have any physical significance, i.e. are not related to the properties of the atmosphere in any simple fashion. They usually have to be manually tuned for each use case. If one wishes to use a regularisation based on second order derivatives (their advantages are demonstrated in Chapter 3), one has to determine even more of these regularisation parameters. This requires a systematic way to obtain them.

One way of to deal with the complexities of irregular grids is to treat the relevant physical quantities of the atmosphere (temperature, trace gas concentrations, etc.) as continuous scalar fields in some volume V (i.e. functions $f : V \subset \mathbb{R}^3 \to \mathbb{R}, \boldsymbol{r} \mapsto f(\boldsymbol{r})$) for as long as possible, perform analytical manipulations on them and discretise the result of these manipulations. To that end, let us assume for the moment that the state vector $\boldsymbol{x}$ represents a single atmospheric quantity $f_{\boldsymbol{x}}$. Mathematically, this means that if $G \subset V \subset \mathbb{R}^3$ is the finite grid in the volume V on which $\boldsymbol{x}$ is defined, then the components of $\boldsymbol{x}$ are the real numbers $f_{\boldsymbol{x}}(\boldsymbol{g})$ for all $\boldsymbol{g} \in G$. Let us also denote the difference between this quantity and its a priori by $\phi(\boldsymbol{r}) = f_{\boldsymbol{x}}(\boldsymbol{r}) - f_{\boldsymbol{x}_{\mathrm{apr}}}(\boldsymbol{r})$. Then we can define the covariance operator C in the volume V by

$$\mathrm{C}\,\phi\,(\boldsymbol{r}) = \int_{\boldsymbol{r'} \in V} \phi\,(\boldsymbol{r'})\, C_k\,(\boldsymbol{r},\, \boldsymbol{r'})\,\mathrm{d}V, \tag{2.11}$$

where $C_k : V \times V \to \mathbb{R}$ is the *covariance kernel*. Then we can treat the scalar fields $\phi\,(\boldsymbol{r})$ and

$\varphi(\boldsymbol{r})$ as elements of a Hilbert space with the product

$$\langle \phi,\, \varphi \rangle = \int_V \phi(\boldsymbol{x})\, \mathrm{C}^{-1} \varphi(\boldsymbol{x})\, \mathrm{d}V. \tag{2.12}$$

It induces the norm $\|\phi\|^2 = \langle \phi,\, \phi \rangle$, which is represented, in our discrete numerical approach, by the second term of (2.7)

$$(\boldsymbol{x} - \boldsymbol{x}_{\mathrm{apr}})^T\, \mathbf{S}_{\mathrm{a}}^{-1}\, (\boldsymbol{x} - \boldsymbol{x}_{\mathrm{apr}}) \approx \|\phi\|^2 = \langle \phi,\, \phi \rangle = \int_V \phi(\boldsymbol{x})\, \mathrm{C}^{-1} \phi(\boldsymbol{x})\, \mathrm{d}V. \tag{2.13}$$

The approximate equality is due to the inevitable error of discretisation. (2.13) implies that if one can find a covariance kernel $\mathrm{C}_k(\boldsymbol{r},\, \boldsymbol{r'})$ that can give plausible covariance in the atmosphere at least for small $\|\boldsymbol{r} - \boldsymbol{r'}\|$ and has an analytical inverse operator C_k^{-1} that can be expressed in a manner simple enough for numerical evaluation, then one can compute the discretised regularisation term (LHS of (2.13)) simply by numerical evaluation of a volume integral.

Using the result above, the approach to regularisation used in this thesis can be outlined. We choose, in a sense, an intermediate path between optimal estimation and Tikhonov regularisation. We will use $\mathbf{S}_{\mathrm{a}}^{-1}$ which is an actual precision matrix and not just an ad-hoc construction as the Tikhonov matrices $\mathbf{\Gamma}$, but represents a simple, analytically invertible covariance relation rather than being an estimation of the full covariance relation between all grid points. The analytical inverse (the continuous equivalent of $\mathbf{S}_{\mathrm{a}}^{-1}$) can then be discretised for numerical evaluation of the regularisation term. Therefore, there is no need to numerically invert large matrices or construct complex ad-hoc operators for irregular grids. We chose the exponential covariance relation for the work described in this thesis. Its definition, inversion and the physical parameters that are used to make the relation representative of the real atmosphere are discussed in the next section, together with an overview of advantages of this method.

2.2.2 The exponential covariance

Let us first consider an atmosphere that is isotropic and has the same physical and statistical properties everywhere. Then one would expect $C_k(\boldsymbol{r}, \boldsymbol{r'}) = g(\|\boldsymbol{r} - \boldsymbol{r'}\|)$ with some

monotonously decreasing function $g : [0, \infty) \to [0, \infty)$. The most common kernel used in literature for fluid dynamics, meteorology and similar applications is the parametric Matérn covariance kernel (introduced, e.g., by Lim and Teo (2009))

$$C_\nu\left(\boldsymbol{r}, \boldsymbol{r}'\right) = \sigma^2 \frac{2^{1-\nu}}{\Gamma\left(\nu\right)} \left(\sqrt{2\nu}\frac{d}{L}\right)^\nu K_\nu \left(\sqrt{2\nu}\frac{d}{L}\right), \tag{2.14}$$

where $d = \|\boldsymbol{r} - \boldsymbol{r}'\|$, σ and L are the standard deviation and typical length scale of structures (correlation length), respectively, of the atmospheric quantity in question. K_ν is the modified Bessel function of the second kind, $\Gamma(\nu)$ is the Gamma function. Exponential and Gaussian covariance kernels are special cases of the kernel (2.14), with $\nu = 0.5$ and $\nu = 1$ respectively. We choose the exponential covariance

$$C_k\left(\boldsymbol{r}, \boldsymbol{r}'\right) = \sigma^2 \exp\left(-\frac{\|\boldsymbol{r} - \boldsymbol{r}'\|}{L}\right), \tag{2.15}$$

as it the Matérn with $\nu = 0.5$ (values close to that values that are typically used for fluid problems) and allows for analytic derivation of the subsequently required quantities. Also, having a significant number of parameters to estimate theoretically, we could not make a good use of the flexibility provided by the free parameter of the Matérn covariance in any case.

It can be shown (Tarantola, 2013) that the norm associated with the covariance (2.15) can be closely approximated by (neglecting some boundary terms)

$$\|\phi\|^2 = \frac{1}{8\pi\sigma^2} \int_{\boldsymbol{r}\in V} \left[\frac{\phi^2}{L^3} + \frac{2\left(\nabla\phi\right)^2}{L} + L\left(\Delta\phi\right)^2\right] \mathrm{d}V. \tag{2.16}$$

In a more realistic picture of the atmosphere, the correlation length L depends on altitude and strongly depends on direction: correlation between vertically separated air parcels is much weaker than between air parcels separated by the same distance horizontally. We propose to deal with anisotropy and variable L by performing a coordinate transformation such that L would be isotropic and constant in resulting coordinates. In particular, let $U, V \subset \mathbb{R}^3$ and consider a bijective map $\boldsymbol{\xi} : V \to U$ such that both $\boldsymbol{\xi}$ and its inverse $\boldsymbol{\xi}^{-1}$ are twice differentiable

on their respective domains and have non-zero first and second derivatives everywhere. Then, using integration by substitution and basic vector calculus identities, equation (2.16) can be written as

$$\begin{aligned}\|\phi\|^2 = \int_{\boldsymbol{\xi}^{-1}(V)} \frac{|\det(\mathrm{D}\boldsymbol{\xi})|}{8\pi\sigma^2}\Bigg(\frac{(\phi(\boldsymbol{\xi}))^2}{L^3} + \frac{2\|\boldsymbol{\delta}(\phi(\boldsymbol{\xi}))\|^2}{L} + \\ L\,\mathrm{Tr}^2\Big[(\mathrm{D}\boldsymbol{\xi})^{-T}\left[\mathrm{D}^2\phi(\boldsymbol{\xi}) - \boldsymbol{\delta}(\phi(\boldsymbol{\xi}))\cdot\mathrm{D}^2\boldsymbol{\xi}\right](\mathrm{D}\boldsymbol{\xi})^{-1}\Big]\Bigg)\mathrm{d}U,\end{aligned} \tag{2.17}$$

where

$$\boldsymbol{\delta}(\phi(\boldsymbol{\xi})) = (\mathrm{D}\boldsymbol{\xi})^{-T}\nabla(\phi(\boldsymbol{\xi}))\,. \tag{2.18}$$

Here $(\mathrm{D}\boldsymbol{\xi})_{ij} = \partial\xi_i/\partial u_j$ is the Jacobian matrix, and we define the matrix $(\mathrm{D}^2 f)_{ij} = (\partial^2 f)/(\partial u_i \partial u_j)$. $\boldsymbol{\xi}$ can be chosen so that all its spatial derivatives could be computed analytically, and $\nabla(\phi(\boldsymbol{\xi}))$, $\mathrm{D}^2(\phi(\boldsymbol{\xi}))$ are the derivatives of ϕ in the transformed space, so numerical evaluation of (2.17) is similar in complexity to that of (2.16), the only notable difference being the need to compute the mixed derivatives $\partial^2\phi/(\partial u_i\partial u_j)$, $i \neq j$ if $\mathrm{D}\boldsymbol{\xi}$ is not diagonal. A large and relevant class of suitable maps $\boldsymbol{\xi}$ can be defined, for example, by assuming that the correlation lengths in vertical and horizontal direction are smooth functions of altitude $L_v(z)$, $L_h(z)$ (we use Cartesian coordinates $(x,\, y,\, z)$ where z axis is vertical). Then the map

$$\boldsymbol{\xi}^{-1}(x,\, y,\, z) = \frac{1}{L}\left(xL_h(z),\, yL_h(z),\, \int_0^z L_v(z')\mathrm{d}z'\right) \tag{2.19}$$

defines a corresponding transformation. A transformation of this form could be used, for example, to perform regularisation in tropopause-based coordinates and use different correlation lengths for troposphere and stratosphere. For the study described in Chapter 3, we only introduce anisotropy (i.e. L_v and L_h are different, but do not depend on altitude) and

equation (2.17) becomes

$$\begin{aligned}\|\Phi\|^2 = \frac{1}{8\pi\sigma^2}\Bigg[&\frac{1}{L_h^2 L_v}\int_V \phi^2 \mathrm{d}V \\ +\frac{2}{L_h}\int_V \frac{L_h}{L_v}\left(\frac{\partial\phi}{\partial x}\right)^2 &+ \frac{L_h}{L_v}\left(\frac{\partial\phi}{\partial y}\right)^2 + \frac{L_v}{L_h}\left(\frac{\partial\phi}{\partial z}\right)^2 \mathrm{d}V \\ +L_v\int_V \left(\frac{L_h}{L_v}\frac{\partial^2\phi}{\partial x^2} + \frac{L_h}{L_v}\frac{\partial^2\phi}{\partial y^2} + \frac{L_v}{L_h}\frac{\partial^2\phi}{\partial z^2}\right)^2 &\mathrm{d}V\Bigg].\end{aligned} \tag{2.20}$$

This general expression can now be discretised for use in the retrieval. We can represent the scalar field $\phi(\boldsymbol{r})$ by the atmospheric state vector $\boldsymbol{x}-\boldsymbol{x}_{\mathrm{apr}}$ and then calculate a discrete approximation to the integral in (2.20). This can then be interpreted as $(\boldsymbol{x}-\boldsymbol{x}_{\mathrm{apr}})^T \mathbf{S}_{\mathrm{a}}^{-1}(\boldsymbol{x}-\boldsymbol{x}_{\mathrm{apr}})$ as seen from equation (2.13). For example, if a matrix $\mathbf{L}_z$ represents a finite difference scheme to calculate the derivative in z direction, i.e. $(\mathbf{L}_z\boldsymbol{x})_j \approx \frac{\partial\phi}{\partial z}|_{\boldsymbol{r}=\boldsymbol{r}_j}$, and the diagonal matrix $\mathbf{V}$ represents the volumes of grid cells ($\mathbf{V}_{ii}$ being one quarter of the volume of all grid cells containing grid point $\boldsymbol{r}_i$, see section 2.3.3 for details), then

$$\begin{aligned}\sum_i (\mathbf{V}\mathbf{L}_z\boldsymbol{x})_i &\approx \int_V \frac{\partial\phi}{\partial z}\mathrm{d}V \\ \boldsymbol{x}^T\mathbf{L}_{\mathrm{z}}^T\mathbf{V}\mathbf{L}_z\boldsymbol{x} &\approx \int_V \left(\frac{\partial\phi}{\partial z}\right)^2 \mathrm{d}V.\end{aligned} \tag{2.21}$$

Other terms of the integral in (2.20) can be computed similarly. Using the notation of equation (2.21), with $(\mathbf{L}_{zz}\boldsymbol{x})_j \approx \frac{\partial^2\phi}{\partial z^2}|_{\boldsymbol{r}=\boldsymbol{r}_j}$ and $\mathbf{L}_x$, $\mathbf{L}_y$, $\mathbf{L}_{xx}$, $\mathbf{L}_{yy}$ defined similarly, we construct the precision matrix

$$\begin{aligned}\mathbf{S}_{\mathrm{a}}^{-1} = \frac{1}{8\pi\sigma^2}\Bigg[&\frac{\mathbf{V}}{L_h^2 L_v} + \frac{2}{L_h}\Bigg\{\frac{L_h}{L_v}\mathbf{L}_x^T\mathbf{V}\mathbf{L}_x + \frac{L_h}{L_v}\mathbf{L}_y^T\mathbf{V}\mathbf{L}_y \\ &+ \frac{L_v}{L_h}\mathbf{L}_z^T\mathbf{V}\mathbf{L}_z\Bigg\} + L_v\mathbf{L}_\Delta^T\mathbf{V}\mathbf{L}_\Delta\Bigg]\end{aligned} \tag{2.22}$$

with

$$\mathbf{L}_\Delta = \frac{L_h}{L_v}\mathbf{L}_{xx} + \frac{L_h}{L_v}\mathbf{L}_{yy} + \frac{L_v}{L_h}\mathbf{L}_{zz}. \tag{2.23}$$

To actually implement the calculation of (2.22) on an irregular grid, we introduce a triangulation for that grid, an interpolation algorithm (both described in section 2.3.1), a method for

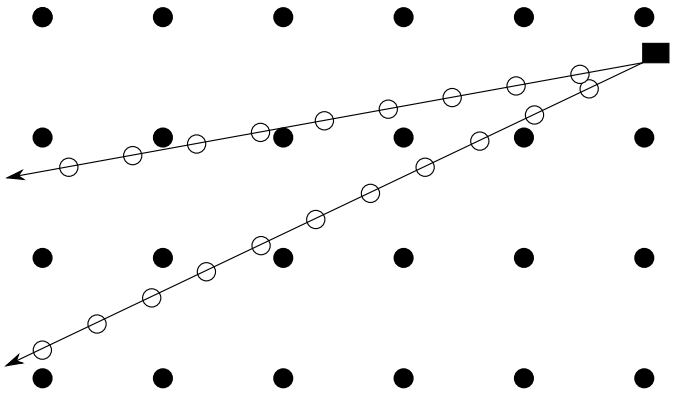

Figure 2.1: Interpolation on lines of sight. Black discs represent retrieval grid points. Empty circles – points along the LOS where atmospheric quantities need to be known (interpolated) in order to perform radiative transfer calculations along that LOS. Black rectangle represents the measurement instrument.

calculating the spatial derivatives $\nabla\phi$ and $\Delta\phi$ which was newly developed to suit the needs of inverse modelling (section 2.3.2), and a way to compute volume integrals (section 2.3.3). The estimation of the physical parameters in equation (2.20) is discussed in Chapter 3.

2.3 Irregular grid

If the retrieval is to be performed on any particular type of grid, a numerically efficient and accurate interpolation method on this grid is required in order to determine the state along the lines of sight needed for the radiative transfer calculation from the state on the atmospheric grid (Figure 2.1). Since we also wish to numerically evaluate the regularisation term (2.20), algorithms for numerical differentiation and volume integration are required. Each of the following subsections deal with one of these issues.

2.3.1 Delaunay triangulation and interpolation

We aim to perform a retrieval on an arbitrary, finite grid. This section explains how vertically stretched Delaunay triangulation with linear interpolation is employed for that purpose.

To maintain generality and compatibility with arbitrary grids, we partition the retrieval volume into Euclidean simplexes (tetrahedrons in our 3-D case) with vertices at grid points.

Many such partitions exist, but it is beneficial to ensure that the number of very elongated tetrahedrons, that increase interpolation and volume integration errors, are kept to a minimum. The standard technique to achieve this is to use a Delaunay triangulation (Delaunay (1934), Boissonnat and Yvinec (1998)), which maximizes the minimum solid angle of any tetrahedron employed. Recall, also, from section 2.2.2 that atmospheric quantities in UTLS and the stratosphere above tend to have much more variation vertically than they do horizontally within similar length scales. This difference can be quantified by comparing horizontal and vertical correlation lengths L_h and L_v. Hence, stretching the space vertically by means of coordinate transformation $(x, y, z) \mapsto (x, y, \eta z)$ with $\eta \sim L_h/L_v$ before constructing a Delaunay triangulation ensures that, on average, the amount of variation of the retrieved quantity in vertical and horizontal directions is similar. This, in turn, allows us to make use of the aforementioned benefits of Delaunay partitioning.

In our implementation, we retrieve several quantities on the same grid, and L_h and L_v may differ for each of them. The cost function of equation (2.20) is evaluated separately for each quantity, so regularisation can still be calculated correctly as long as spatial structures of every quantity are adequately sampled by the grid. In practice, this means that as long as the ratio L_h/L_v is of the same order of magnitude for all quantities, they can all be retrieved on one grid. Fortunately this is usually the case (see Chapter 3). For test retrievals in this work $L_h/L_v = 200$ for trace gas concentrations and $L_h/L_v = 67$ for temperature, therefore we set $\eta = 100$. Retrieval results do not indicate systematic oversampling or undersampling in either horizontal or vertical directions. The retrieval is not sensitive to a change in η, as long as it is not a change by more than an order of magnitude .

In order to keep the computational costs low, we use a simple linear interpolation scheme: in each Delaunay cell we express an atmospheric quantity f at any point $\boldsymbol{x}$ as

$$f(\boldsymbol{r}) = f(\boldsymbol{r_0}) + \boldsymbol{k} \cdot (\boldsymbol{r} - \boldsymbol{r_0}), \quad \boldsymbol{k} = \text{const.} \tag{2.24}$$

If $\boldsymbol{r}_i$, $0 \leq i \leq 4$ are the four vertices of the Delaunay cell, the constant gradient $\boldsymbol{k}$ can obtained

from a system of three linear equations

$$f(\boldsymbol{r}_i) = f(\boldsymbol{r_0}) + \boldsymbol{k} \cdot (\boldsymbol{r}_i - \boldsymbol{r}_0), \quad 1 \leq i \leq 3 \tag{2.25}$$

Based on elementary properties of systems of linear equations, there will be a unique solution $\boldsymbol{k}$, if and only if the vectors $\boldsymbol{r}_i - \boldsymbol{r}_0$, $i \leq i \leq 3$ are linearly independent. If they are not independent, they necessarily lie all in one plane. However, the definition of Delaunay grid ensures that they are not even close to being in one plane, as that would result in a tetrahedron with a very large circumscribed sphere. Hence the solution $\boldsymbol{k}$ always exists, is unique, and can be found numerically without running into troublesome near-degenerate cases. Also, to investigate the behaviour of this interpolation scheme on the cell boundary, let us restrict the equation system (2.25) to one face of the tetrahedron, e.g. the triangle with vertices $\boldsymbol{r}_0$, $\boldsymbol{r}_1$, $\boldsymbol{r}_2$. Then (2.25) becomes a system of two equations ($1 \leq i \leq 2$) with the 2-D vector $\boldsymbol{k}$ as the unknown. We can then prove, same as in the 3-D case, that it always has a unique solution. By uniqueness, the interpolation on the face of tetrahedron must then give the same result as the 3-D interpolations inside the tetrahedrons on either side of the face $\boldsymbol{r}_0$, $\boldsymbol{r}_1$, $\boldsymbol{r}_2$. This proves that this interpolation is also continuous at cell boundaries, a highly desired property for any interpolation. We will also see that it is consistent with our volume integration scheme of choice described in section 2.3.3. Implementation is simple and fast, as any point inside a given Delaunay cell can be interpolated with data about that cell only. The gradient ∇f of the atmospheric quantity, is, however, generally discontinuous at cell boundaries making the interpolation unsuitable for direct use in spatial derivative evaluation. We cannot, however, ensure continuity of ∇f at the cell boundary without making the interpolation dependent on data from nearby cells, which would greatly increase the computational cost.

2.3.2 Derivatives

In order to evaluate the cost function based on 3-D exponential covariance (2.20), we need to estimate $\nabla\phi$ and $\Delta\phi$ at every grid point (as before, $\phi = f - f_{\text{apr}}$ is the departure of atmospheric quantity f from the a priori). This section describes the algorithm we use to

achieve that on irregular Delaunay grids.

We begin by establishing some requirements that our derivative-estimation algorithm will have to meet. Firstly, recall that our inverse model assembles the precision matrix $\mathbf{S}_a^{-1}$ so that $(\boldsymbol{y}-\boldsymbol{y}_{\mathrm{apr}})^T \mathbf{S}_a^{-1} (\boldsymbol{y}-\boldsymbol{y}_{\mathrm{apr}})$ would be a numerical representation of (2.20) (or, more generally, (2.17)). Let us write $\mathbf{S}_a^{-1} = \mathbf{A}+\mathbf{B}$, where $\mathbf{A}$ is a diagonal matrix representing the first integral of (2.20) (or first term of (2.17)), and $\mathbf{B}$ represents the remaining terms. If $\mathbf{B}$ were an exact representation, it would be positive definite by construction, but this may not hold with $\nabla\phi$ and $\Delta\phi$ obtained numerically for a finite grid. If indeed an atmospheric state vector $\boldsymbol{q}$ exists so that $\boldsymbol{q}^T\mathbf{B}\boldsymbol{q}=0$, then for every atmospheric state $\boldsymbol{y}$

$$\begin{aligned}(\boldsymbol{y}\pm\boldsymbol{q}-\boldsymbol{y}_{\mathrm{apr}})^T \mathbf{B} (\boldsymbol{y}\pm\boldsymbol{q}-\boldsymbol{y}_{\mathrm{apr}}) = \\ (\boldsymbol{y}-\boldsymbol{y}_{\mathrm{apr}})^T \mathbf{B} (\boldsymbol{y}-\boldsymbol{y}_{\mathrm{apr}}) \pm 2 (\boldsymbol{y}-\boldsymbol{y}_{\mathrm{apr}})^T \mathbf{B}\boldsymbol{q},\end{aligned} \tag{2.26}$$

hence one of the states $\boldsymbol{y}\pm\boldsymbol{q}$ would be favoured (have a smaller cost function) over $\boldsymbol{y}$ by the inverse modelling algorithm. Therefore, a scaled version of $\boldsymbol{q}$ would appear on any retrieval as noise. This particular type of noise would only be suppressed by the cost function term from $(\boldsymbol{y}-\boldsymbol{y}_{\mathrm{apr}})^T \mathbf{A} (\boldsymbol{y}-\boldsymbol{y}_{\mathrm{apr}})$. This guarantees only that $\boldsymbol{y}$ is not very far from a priori, but does nothing to ensure that it is even continuous. This often results in retrievals where noise expresses itself as unphysical periodic structures and is unacceptable.

We deal with this problem by explicitly ensuring that $\mathbf{B}$ is positive definite. Consider the estimation of derivatives at a single grid point $\boldsymbol{a}\in\mathbb{R}^3$. $\nabla\phi(\boldsymbol{a})$, and $\Delta\phi(\boldsymbol{a})$ are numerically estimated from the values of ϕ in some (say m) grid points near $\boldsymbol{a}$. We can write this as a map

$$\begin{aligned}&D_{\boldsymbol{a}}(\phi):\mathbb{R}^m\to\mathbb{R}^6\\ &\qquad\{\phi(\boldsymbol{r}_i)-\phi(\boldsymbol{a}) : 1\le i\le m\}\mapsto\\ &\qquad\left\{\frac{\partial\phi}{\partial x},\frac{\partial\phi}{\partial y},\frac{\partial\phi}{\partial z},\frac{\partial^2\phi}{\partial x^2},\frac{\partial^2\phi}{\partial y^2},\frac{\partial^2\phi}{\partial z^2}\right\}.\end{aligned} \tag{2.27}$$

Now $\boldsymbol{q}^T\mathbf{B}\boldsymbol{q}=0$, $\boldsymbol{q}\neq\mathbf{0}$ implies that at every grid point $\boldsymbol{a}\in\mathbb{R}^3$ we have $\nabla\phi(\boldsymbol{a})=0$, $\Delta\phi(\boldsymbol{a})=0$ for the $\phi(\boldsymbol{a})$ corresponding to state $\boldsymbol{q}$. Hence such $\boldsymbol{q}$ will not exist, if we require

that $D_{\boldsymbol{a}}$ have trivial null space for all grid points $\boldsymbol{a}$ (i.e. $D_a(\phi) = \{0, \ldots, 0\}$ only if $\phi(\boldsymbol{x}_i) = \phi(\boldsymbol{a})$, $1 \leq i \leq m$). The converse is not always true, so the trivial null space requirement is a stronger condition than absolutely necessary. It is, however, advantageous because it restricts the derivative-estimation algorithm at each grid point independently and hence can be implemented without computationally expensive operations on $\mathbf{S}_a^{-1}$ as a whole.

Since (2.27) will be used directly to construct $\mathbf{S}_a^{-1}$, which does not depend on atmospheric state $\boldsymbol{y}$ and hence on $\phi(\boldsymbol{a})$, $D_{\boldsymbol{a}}$ must be a linear map, so null space is a vector space of dimension $\max\{0, m-6\}$, hence we need $m \leq 6$. We also want to avoid the derivative estimation to be underdetermined ($m \geq 6$), so we choose $m = 6$, i.e. we aim to construct a linear map (2.27) that estimates derivatives at grid point $\boldsymbol{a}$ using atmospheric quantity values at 6 points around $\boldsymbol{a}$. This prevents us from using interpolation for derivative calculations, since each interpolated value depends on atmospheric quantity values at multiple (in our case 4) grid points and consequently, even if the same grid point is reused for several interpolated values, the total number of grid points employed exceeds 6 in any interpolation-based scheme we could come up with.

A solution satisfying the above criterion and able to deal with grid points with neighbours at irregular positions is based on polynomial fitting. For 6 grid points around a grid point $\boldsymbol{a} = (x_a, y_a, z_a)$ denoted as $\boldsymbol{r}_i = (x_a + x_i, x_a + y_i, x_a + z_i)$, $1 \leq i \leq 6$ we write

$$\begin{aligned} \phi(\boldsymbol{r}_i) - \phi(\boldsymbol{a}) &= \phi_x x_i + \phi_y y_i + \phi_z z_i \\ &+ \frac{\phi_{xx}}{2} x_i^2 + \frac{\phi_{yy}}{2} y_i^2 + \frac{\phi_{zz}}{2} z_i^2, \quad 1 \leq i \leq 6. \end{aligned} \tag{2.28}$$

We solve this as a linear system for the unknowns ϕ_x, ϕ_y, ϕ_z, ϕ_{xx}, ϕ_{yy}, ϕ_{zz}, which can then be directly identified with the derivatives we seek. Note that, as we required, the system can be solved by inverting a 6-by-6 matrix that only depends on $\boldsymbol{r}_i$ and not $\phi(\boldsymbol{r}_i)$, so we can use this method to precompute a matrix that would act on the atmospheric state vector to return the value of the volume integral over the derivative (2.20).

The only remaining issue is selecting a suitable set of grid points $\boldsymbol{r}_i$ so that the resulting matrix that needs to be inverted would not be singular or have a very high condition number. We found that this is much easier to achieve by imposing simple geometric criteria for point

selection rather than algebraic conditions.

Let $\boldsymbol{a}$ be a point on Delaunay grid. The main idea of the algorithm we propose is to pick, for each spatial dimension d, a pair of points r_1, r_2 suitable for estimating the derivative in that direction. Points of such a pair should be sufficiently separated in d direction (i.e. projections of the vectors $\boldsymbol{r}_i - \boldsymbol{a}$ to d direction sufficiently different), be on the opposite sides of $\boldsymbol{a}$ and be reasonably close to $\boldsymbol{a}$. We obtain the required 6 points by choosing one pair of points for each of the three dimensions. This can be implemented as follows.

Let $\boldsymbol{a} = (x_a, y_a, z_a)$, and let us write the coordinates of other points on this grid as $\boldsymbol{r}_i = (x_a + x_i, y_a + y_i, z_a + z_i)$ with $r_i = \|\boldsymbol{r}_i - \boldsymbol{a}\|$. Let $0 < \beta < 1$ and $\gamma > 1$ be constants, suitable numeric values will be discussed further on. Then:

1. For each Delaunay grid neighbour $\boldsymbol{r}_i$ of $\boldsymbol{a}$, compute $\alpha_{ix} = x_i/r_i$, $\alpha_{iy} = y_i/r_i$, $\alpha_{iz} = z_i/r_i$.

2. If i, j such that $|\alpha_{ix}| > \beta$, $|\alpha_{jx}| > \beta$, $\alpha_{ix}\alpha_{jx} < 0$ exist, then pick $\boldsymbol{x}_i$, $\boldsymbol{x}_j$ for derivative calculation. Else if k, l such that $|\alpha_{kx}| > |\alpha_{lx}| > \beta$, $\alpha_{kx}/\alpha_{lx} > \gamma$ exist, then pick $\boldsymbol{x}_l$, $\boldsymbol{x}_k$ for derivative calculation.

3. Repeat step 2 for y and z dimensions. Each point can be only picked for one of the dimensions.

4. If neither condition of step 2 is satisfied for at least 1 dimension, repeat steps 1-3 with not only direct Delaunay grid neighbours of $\boldsymbol{a}$, but also second neighbours (i.e. neighbours of neighbours). If this fails as well, do not calculate derivatives at the point $\boldsymbol{a}$ and simply assume them to be zero.

We found that the polynomial interpolation method is robust and a rather low value of $\beta = 0.3$ was sufficient to produce suitable sets of neighbouring points (i.e. almost all 6-by-6 matrices resulting from such choice of points can be reliably inverted for polynomial fitting). In practice this means that the algorithm can find a suitable pair of points for dimension d unless all the Delaunay neighbours of the point $\boldsymbol{a}$ are located very close to the other two axes with respect to the point $\boldsymbol{a}$.

2.3.3 Volume integration

Computing (2.20) requires a way to estimate volume integrals on Delaunay grid, which is described here.

Let a Delaunay cell have vertices $\boldsymbol{r}_i$ and face areas S_i for $0 \leq i \leq 3$, and volume V. Then integrating an atmospheric quantity f as interpolated in (2.24) over V we get

$$\int_V f(\boldsymbol{r})\,\mathrm{d}V = \frac{V}{4}\sum_{i=0}^{3} f(\boldsymbol{r}_i)\,. \tag{2.29}$$

One can prove this by writing (2.24) with $\boldsymbol{r}_i$, $0 \leq i \leq 3$ instead of $\boldsymbol{r}_0$ and adding up the resulting four equations to obtain

$$f(\boldsymbol{r}) = \frac{1}{4}\sum_{i=0}^{3} f(\boldsymbol{r}_i) + \boldsymbol{k}\cdot\left(\boldsymbol{r} - \frac{1}{4}\sum_{i=0}^{3}\boldsymbol{r}_i\right). \tag{2.30}$$

Now choose Cartesian coordinates $(x',\, y',\, z')$, where $\boldsymbol{r_0} = (H,\, 0,\, 0)$ and $\boldsymbol{r}_i$, $1 \leq i \leq 3$ lie in the plane $x' = 0$ and consider the x' component of the integral $\boldsymbol{I} = \int_V \left(\boldsymbol{r} - 1/4\sum_{i=0}^{3}\boldsymbol{r}_i\right)\mathrm{d}V$

$$\begin{aligned} I_{x'} = \int_V \left(x' - \frac{H}{4}\right)\mathrm{d}V &= \int_0^H x' S_0 \left(\frac{H-x'}{H}\right)^2 \mathrm{d}x' \\ &- \frac{HV}{4} = \frac{H^2 S_0}{12} - \frac{HV}{4} = 0. \end{aligned} \tag{2.31}$$

As we can choose such coordinates for any vertex instead of $\boldsymbol{r}_0$, the integral $\boldsymbol{I}$ has zero component in three linearly independent directions, so $\boldsymbol{I} = 0$. Then integrating (2.30) over V yields (2.29) and completes the proof.

We can now see that (2.29) gives an exact value to the volume integral of f provided that f behaves exactly as prescribed by our interpolation scheme. Since the interpolation is linear we may expect the values of volume integrals to be correct to the first order in cell dimensions. Since, generally, all data fed into the inverse modelling problem is interpolated beforehand, there is little reason to expect that a more elaborate and accurate volume integration scheme would improve the accuracy of retrievals on its own. A computationally more costly method based on Voronoi cells (Voronoi, 1908; Aurenhammer et al., 2013) was also implemented, but

did not produce meaningfully different results.

2.4 Diagnostics

Estimating the accuracy of remote sensing data products generated by means of inverse modelling is, in general, rather difficult due to the indirect manner in which they are obtained from the actual measurements. Many established techniques for calculating diagnostics are prohibitively numerically expensive in the case of large 3-D retrievals. In this section we discuss two methods of obtaining diagnostics for 3-D problems and the relevant mathematical algorithms for applying these methods to large problems.

So far we have made few assumptions about the behaviour of the forward model $\boldsymbol{F}$ and, as far as inverse modelling is concerned, treated it as a black box. The only property we really need for the inverse modelling methods described in this thesis to work is that $\boldsymbol{F}(\boldsymbol{x})$ is continuous with respect to $\boldsymbol{x}$. The radiative transfer models used for limb sounding in practise are indeed rather complex, and it is difficult to identify further useful mathematical properties of their results. In particular, radiative transfer is typically highly non-linear. On the other hand, once the solution is found, one can investigate the behaviour of $\boldsymbol{F}$ in a small neighborhood of the solution by assuming that the forward model responds linearly to small perturbations in its input. The following methods make use of that fact in two different ways.

2.4.1 Linear diagnostics

If the forward model $\boldsymbol{F}$ is assumed to be locally linear, we can employ many results from the linear inverse modelling theory. In particular, Rodgers (2000) proves that the retrieved atmospheric state $\boldsymbol{x}$ can be written in terms of the (unknown) true state $\boldsymbol{x}_t$ and the measurement error $\boldsymbol{\epsilon}$ as

$$\boldsymbol{x} = \mathbf{A}\boldsymbol{x}_\mathrm{t} + (\mathbf{I} - \mathbf{A})\,\boldsymbol{x}_\mathrm{a} + \mathbf{G}\boldsymbol{\epsilon}, \tag{2.32}$$

where

$$\begin{aligned} \mathbf{G} &= \mathbf{M}^{-1}\,(\mathrm{D}\mathbf{F}(\boldsymbol{x}))^T\,\mathbf{S}_\epsilon^{-1} \qquad \mathbf{A} = \mathbf{G}\,\mathrm{D}\mathbf{F}(\boldsymbol{x}) \\ \mathbf{M} &= \mathbf{S}_\mathrm{a}^{-1} + [\mathrm{D}\mathbf{F}(\boldsymbol{x})]^T\,\mathbf{S}_\epsilon^{-1}\,\mathrm{D}\mathbf{F}(\boldsymbol{x}). \end{aligned} \tag{2.33}$$

Notation here follows (2.7), $\mathrm{D}\mathbf{F}(\boldsymbol{x})$ denotes the Jacobian matrix of $\boldsymbol{F}$, which is considered constant in this linearised theory. The *averaging kernel* $\mathbf{A}$ describes the retrievals response to the signal. In the case of an ideal measurement one would have $\mathbf{A} = \mathbf{I}$, and in reality $\mathbb{A}$ represents a set of peaked distributions, reflecting the finite resolution and possible cross-talk in the measurements. The so-called *gain matrix* $\mathbf{G}$ describes the response of the retrieval to the measured signal. Its significance can be seen more clearly if one substitutes the expression of $\mathbf{A}$ from (2.33) to (2.32)

$$\boldsymbol{x} - \boldsymbol{x}_{\mathrm{apr}} = \mathbf{G}\left(\mathrm{D}\mathbf{F}(\boldsymbol{x})\left(\boldsymbol{x}_{\mathrm{t}} - \boldsymbol{x}_{\mathrm{apr}}\right) + \boldsymbol{\epsilon}\right). \tag{2.34}$$

$\mathbf{G}$ is then the complete characterisation of the (linearised) retrievals response to both actual signal and noise and would typically be sufficient to characterise the measurement accuracy (evaluate errors due to different sources, resolution, etc.), if only it can be evaluated explicitly. The computational cost of inverting $\mathbf{M}$ is at the very best $O(N^{2.8})$ (Skiena, 1998) for a retrieval with N grid points, a worse scaling than the whole retrieval and completely unfeasible for large problems with $10^5 - 10^6$ points. Note, however, that i'th element of $\boldsymbol{x}$ only depends on i'th line of the matrix $\mathbf{G}$ (see (2.34), so one can use Krylov subspace methods (e.g. conjugate gradients) to solve $\mathbf{M}\boldsymbol{r}_i = \boldsymbol{e}_i$ for the i'th row $\boldsymbol{r}_i^T$ of the inverse matrix $\mathbf{M}^{-1}$. The i'th row $\boldsymbol{g}_i$ of $\mathbf{G}$ can then be obtained as $\boldsymbol{r}_i^T \left(\mathrm{D}\mathbf{F}(\boldsymbol{x})\right)^T \mathbf{S}_\epsilon^{-1}$. This operation, just as the numerical implementation of the retrieval itself, can be realised by matrix-vector and vector-vector multiplication only. Furthermore, all the matrices involved in the definition of $\mathbf{G}$ are sparse in our retrieval implementation. The calculation of diagnostic parameters for a single grid point (the $\boldsymbol{x}$ component x_i), or a few of them, is hence feasible with this method. Once $\boldsymbol{g}_i$ is calculated, one can, for example, obtain the variance of the retrieved value of x_i due to instrument error by computing $\boldsymbol{g}_i^T \mathbf{S}_\epsilon \boldsymbol{g}_i$. An example of such calculations for a test case is given in Chapter 3.

2.4.2 Monte Carlo diagnostics for 3-D retrievals

Suppose we made a total error $\hat{\boldsymbol{\epsilon}}$ in a particular estimate of $\boldsymbol{F}(\boldsymbol{x}) - \boldsymbol{y}$. It could have been due to instrument noise or the fact that our imprecise knowledge of atmospheric quantities (retrieved or unretrieved) has an effect on the (other) retrieved quantities. Using the linear theory in the neighbourhood of the original inverse problem solution $\boldsymbol{x}$, the new solution due to the error $\hat{\boldsymbol{\epsilon}}$ can be derived from (2.34)

$$\hat{\boldsymbol{x}} = \boldsymbol{x}_{\mathrm{apr}} + \mathbf{G}\hat{\boldsymbol{\epsilon}} = \boldsymbol{x}_{\mathrm{apr}} + \mathbf{M}^{-1} \left(\mathrm{D}\mathbf{F}(\boldsymbol{x})\right)^T \mathbf{S}_\epsilon^{-1} \hat{\boldsymbol{\epsilon}} \tag{2.35}$$

Since $\mathbf{M}$ is sparse, $\hat{\boldsymbol{x}}$ can be cheaply computed by solving the linear equation system

$$\mathbf{M} \left(\hat{\boldsymbol{x}} - \boldsymbol{x}_{\mathrm{apr}}\right) = \left(\mathrm{D}\mathbf{F}(\boldsymbol{x})\right)^T \mathbf{S}_\epsilon^{-1} \tag{2.36}$$

The main idea of the widely applied Monte Carlo technique is that the correct variance for $\hat{\boldsymbol{x}}$ can be obtained from a relatively small set of different $\hat{\boldsymbol{x}}$, provided that the corresponding $\hat{\boldsymbol{\epsilon}}$ are statistically representative of the actual (normal) error distribution. Ungermann (2013) used this technique for a 2-D retrieval and achieved good agreement with a deterministic computation with just 32 samples of $\hat{\boldsymbol{\epsilon}}$. The main advantage of this method is the possibility to obtain error estimates for all grid points at a reasonable computational cost, as opposed to just a few points (at a computational cost of similar order to Monte Carlo) as in the methods from the last section.

In the statistical model of our retrieval, instrument noise values are normally distributed with covariance $\mathbf{S}_\epsilon$ and contribute to $\hat{\boldsymbol{\epsilon}}$ directly, while the atmospheric parameters collectively have normal distribution $\mathbf{S}_\mathrm{a}$, and their perturbation $\hat{\boldsymbol{q}}$ contributes to $\hat{\boldsymbol{\epsilon}}$ with $\mathrm{D}\mathbf{F}(\boldsymbol{x}))\hat{\boldsymbol{q}}$. In the case of GLORIA retrievals, $\mathbf{S}_\epsilon$ is diagonal, so random samples of simulated instrument noise are just vectors of independent samples of 1D normal distribution. $\mathbf{S}_\mathrm{a}$ has a more complicated structure forcing us to adopt the more general solution, commonly used with the Monte Carlo technique. One generates a vector $\boldsymbol{p}$ of independent standard normal random variables and finds a square matrix $\tilde{\mathbf{L}}$ such that $\tilde{\mathbf{L}}\tilde{\mathbf{L}}^T = \mathbf{S}_\mathrm{a}$. Then one can set $\hat{\boldsymbol{q}} = \tilde{\mathbf{L}}\boldsymbol{p}$, and indeed

$\langle \hat{\boldsymbol{q}}\hat{\boldsymbol{q}}^T \rangle = \langle \tilde{\mathbf{L}}\boldsymbol{p}\boldsymbol{p}^T\tilde{\mathbf{L}}^T \rangle = \tilde{\mathbf{L}}\langle \boldsymbol{p}\boldsymbol{p}^T \rangle \tilde{\mathbf{L}}^T = \mathbf{S}_\mathrm{a}$, i.e. the vector $\hat{\boldsymbol{q}}$ has the required covariance (the angle brackets in the expression above denote the expected value).

A widely used technique for obtaining the matrix $\mathbf{L}$ is the Cholesky decomposition (Golub, 1996). Given the covariance matrix $\mathbf{S}_\mathrm{a} = \{s_{ij}\}$ it explicitly provides a lower triangular matrix root $\tilde{\mathbf{L}} = \{l_{ij}\}$ satisfying $\tilde{\mathbf{L}}\tilde{\mathbf{L}}^T = \mathbf{S}_\mathrm{a}$ as shown in (2.37).

$$l_{ij} = \begin{cases} \sqrt{s_{ij} - \sum_{k=1}^{i-1} l_{ik}^2}, & i = j \\ l_{jj}^{-1}\left(s_{ij} - \sum_{k=1}^{j-1} l_{ik}l_{jk}\right), & i > j \\ 0, & i < j. \end{cases} \tag{2.37}$$

In practice we do not usually assemble the covariance matrix $\mathbf{S}_\mathrm{a}$, but rather its inverse: the precision matrix $\mathbf{S}_\mathrm{a}^{-1}$, because the latter is sparse. This is not an issue, since $\mathbf{S}_\mathrm{a}^{-1}$ is then also symmetric positive definite, so one can compute its root $\mathbf{L}$ such that $\mathbf{L}\mathbf{L}^T = \mathbf{S}_\mathrm{a}^{-1}$ in the same way as above, and then obtain $\hat{\boldsymbol{q}}$ from the linear system $\mathbf{S}_\mathrm{a}^{-1}\hat{\boldsymbol{q}} = \mathbf{L}\boldsymbol{p}$. We will refer to the components of precision matrix by $\mathbf{S}_\mathrm{a}^{-1} = \{a_{ij}\}$. Ungermann (2013) successfully used this technique for 1-D retrievals. We will now demonstrate why this is inherently problematic for higher dimensions and introduce a different method suitable for 3-D.

Cholesky decomposition does not preserve the sparse structure of $\mathbf{S}_\mathrm{a}^{-1}$, i.e. the $\mathbf{L}$ obtained in this way will typically have many more non-zero entries than $\mathbf{S}_\mathrm{a}^{-1}$. It follows from (2.37), however, that if $\mathbf{S}_\mathrm{a}^{-1}$ has lower half-bandwidth $w = \min\{k \geq 0 : i - j > k \Rightarrow a_{ij} = 0\}$, then so has $\mathbf{L}$. In practice, this means that if $\mathbf{S}_\mathrm{a}^{-1}$ is a sparse $N \times N$ matrix with half-bandwidth $w \ll N$, $\mathbf{L}$ will have approximately $N(w+1)$ non zero entries. Cholesky decomposition is hence well suited for computing diagnostics of 1-D retrievals: assuming that the value of the retrieved atmospheric parameter at one point only directly correlates with its w nearest neighbouring points in each direction, one gets a precision matrix with half-bandwidth w and can compute $\mathbf{L}$ cheaply with $O(Nw^2)$ operations.

The situation is very different in the higher dimensions. We will use some results of graph theory to show that Cholesky decomposition is not practical in those cases. The n-dimensional lattice graph P_k^n consists of an n-dimensional rectangular grid of size k in each direction,

with edge between any two grid neighbours. Let us label the vertices of P_k^n with integers: $P_k^n = \{v_i : 1 \leq i \leq k^n\}$, and let q be the maximum difference of indexes of neighbouring vertices ($q = \max\{\|i-j\| : v_i, v_j \text{neighbours}\}$). Then the *bandwidth* $\varphi(P_k^n)$ of P_k^n is defined as the minimum possible value of q among all possible ways to label the vertices. Now say we have some physical quantity defined on each vertex of this grid. Then any reasonable precision matrix $\mathbf{S}_\mathrm{a}^{-1}$ for this grid would at least give non-zero correlations between grid neighbours, i.e. $\left(\mathbf{S}_\mathrm{a}^{-1}\right)_{ij} \neq 0$ if v_i and v_j are neighbours. Then, by comparing the definitions of $\varphi(P_k^n)$ and lower-half bandwidth w of the precision matrix from the last paragraph, one can see that $2w+1 \geq \varphi(P_k^n)$. FitzGerald (1974) showed that $\varphi\left(P_k^2\right) = k$ and $\varphi\left(P_k^3\right) = \lfloor 3k^2/4 + k/2 \rfloor$. Therefore, the narrowest possible half-bandwidths of $\mathbf{S}_\mathrm{a}^{-1}$ are $w = O(k)$ in 2-D and $w = O\left(k^2\right)$ in 3D. It follows that if the grid contains a total of N points, the computational cost of Cholesky decomposition would be $O(N^2)$ in 2D and $O\left(N^{7/3}\right)$ in 3D, which is unsatisfactory for large retrievals.

For these higher dimensions, we need to use sparse matrix iterative techniques to reduce computational cost and memory storage requirements, such as Krylov subspace methods. In general, it is rather difficult to find a simple iteration scheme that would compute a square root of a matrix and converge reasonably fast. Here we will follow an algorithm proposed by Allen et al. (2000). Consider a system of linear ordinary differential equations (ODEs) with initial condition

$$\begin{cases} \mathrm{d}\boldsymbol{v}/\mathrm{d}t = -\frac{1}{2}\left(\mathbf{S}_\mathrm{a}^{-1}t - (1-t)\,I\right)^{-1}\left(\mathbf{I} - \mathbf{S}_\mathrm{a}^{-1}\right)\boldsymbol{v}(t) \\ \boldsymbol{v}(0) = \boldsymbol{u}, \end{cases} \tag{2.38}$$

where $\boldsymbol{v}(t)$ is a column vector of size N, $\mathbf{I}$ is the identity matrix and $\mathbf{S}_\mathrm{a}^{-1}$ is a $N \times N$ symmetric positive definite matrix, prescaled so that $\|\mathbf{S}_\mathrm{a}^{-1}\|_\infty < 1$ (i. e. $\mathbf{S}_\mathrm{a}^{-1} - \mathbf{I}$ is non-singular). $\left(\mathbf{S}_\mathrm{a}^{-1} - \mathbf{I}\right)$ and $\left(\mathbf{S}_\mathrm{a}^{-1}t + (1-t)\mathbf{I}\right)^{-1}$ commute for $0 \leq t \leq 1$, which makes it easy to verify that

$$\boldsymbol{v}(t) = \left(\mathbf{S}_\mathrm{a}^{-1}t - (1-t)\,\mathbf{I}\right)^{1/2}\boldsymbol{u} \tag{2.39}$$

is the solution of (2.38). Hence we can obtain $\boldsymbol{v}(1) = \mathbf{S}_\mathrm{a}^{-1/2}\boldsymbol{u}$ by solving (2.38) numerically,

and then solve the linear system $\mathbf{S}_\mathrm{a}^{-1}\hat{\boldsymbol{q}} = \boldsymbol{v}\,(1)$ for the vector $\hat{\boldsymbol{q}}$, so that $\hat{\boldsymbol{q}} = \mathbf{S}_\mathrm{a}\mathbf{S}_\mathrm{a}^{-1/2}\boldsymbol{u}$. The matrix $\mathbf{S}_\mathrm{a}^{-1/2}$ above is symmetric by construction (sum of products of symmetric matrices), hence

$$\langle \hat{\boldsymbol{q}}\hat{\boldsymbol{q}}^T \rangle = \mathbf{S}_\mathrm{a}\mathbf{S}_\mathrm{a}^{-1/2}\langle \boldsymbol{u}\boldsymbol{u}^T \rangle \mathbf{S}_\mathrm{a}^{-1/2}\mathbf{S}_\mathrm{a} = \mathbf{S}_\mathrm{a}, \tag{2.40}$$

i.e. $\hat{\boldsymbol{q}}$ is indeed the vector required for Monte Carlo simulations. Note also that one does not need to explicitly calculate matrix inverses while solving the ODE, since

$$\left(\mathbf{S}_\mathrm{a}^{-1}t - (1-t)\,\mathbf{I}\right)\frac{\mathrm{d}\boldsymbol{v}}{\mathrm{d}t} = -\frac{1}{2}\left(\mathbf{I} - \mathbf{S}_\mathrm{a}^{-1}\right)\boldsymbol{v}\,(t) \tag{2.41}$$

is a linear system that can be solved for $\mathrm{d}\boldsymbol{v}/\mathrm{d}t$.

We chose a classical approach – a Runge-Kutta method, to solve the linear ODE system numerically. Using constant step size proved to be inefficient, so adaptive step size control was introduced (in particular, a fifth order Runge-Kutta-Fehlberg method by Fehlberg (1985)). Conjugate gradients method (Saad, 2003) was employed for all the linear equation systems involved. If we make the same assumption about the structure of the inverse of the correlation matrix as before, i.e. that atmospheric quantities are only correlated between nearest grid neighbours, the said matrix will have a constant number of non-zero entries in each row for any amount of rows (grid points) N. More explicitly, under this assumption the covariance matrix for 1-D retrieval would be tridiagonal, and for a 3-D retrieval on a regular rectangular grid it would contain 6 non-zero entries in each row. Therefore, each iteration of the conjugate gradients algorithm will cost $O\,(N)$ operations. It is difficult, in general, to estimate the dependence of required number of iterations on N, but in our case large matrices seem to converge similarly to smaller ones and the whole computational cost of generating random vectors remains close to $O(N)$, which is a huge improvement over the Cholesky decomposition. The algorithm does not, though, explicitly yield the root of the covariance matrix and only gives one random vector per run. Hence, unlike the Cholesky decomposition, it must be executed again for each new random vector required, so it is only feasible if the number of random vectors required is a lot smaller than N. Fortunately, this is very much the case in practice, since the number of random vectors required is typically only of the order of 100 or

less (Ungermann, 2013).

Although this root-finding algorithm does not provide a way to directly multiply the matrix root with itself, there is an inexpensive way to verify that the matrix root was computed correctly. Let $\mathbf{S}$ be a $n \times n$ symmetric positive definite matrix, let $\boldsymbol{e}_i$ be the i'th unit vector ($1 \leq i \leq n$), and compute $\boldsymbol{v}_i = \mathbf{S}^{1/2}\boldsymbol{e}_i$ using our algorithm. Then for any i, j we have $\boldsymbol{v}_i^T\boldsymbol{v}_j = \boldsymbol{e}_i^T \left(\mathbf{S}^{1/2}\right)^T \mathbf{S}^{1/2}\boldsymbol{e}_i = \boldsymbol{e}_i^T\mathbf{S}\boldsymbol{e}_i = \mathbf{S}_{ij}$, an element of $\mathbf{S}$. Hence the quality of the matrix root can be evaluated by comparing $\boldsymbol{v}_i^T\boldsymbol{v}_j$ with $\mathbf{S}_{ij}$. The error tolerances of conjugate gradients and Runge-Kutta were adjusted so that these values would differ by at most 10^{-4} when factoring a matrix prescaled so that the largest eigenvalue is approximately 0.95.

Chapter summary

This chapter introduced the newly developed regularisation scheme for 3-D tomography based on physical parameters and second-order spatial derivatives, as well as all the mathematical tools required to perform a retrieval, with the new regularisation, on irregular grids. Despite the added conceptual complexity of the newly developed methods compared to previously existing alternatives, there are new opportunities for improved efficiency and overall reduction of computational costs. It is now possible to obtain diagnostic information for all grid points of a 3-D retrieval thanks to the Monte Carlo error estimation method newly adopted for 3D problems. Refer to the next chapter for the tests and performance evaluation for the new methods.

Chapter 3

3-D tomography with GLORIA: method evaluation

In the previous chapter, a new regularisation scheme (Section 2.2), methods for use of irregular grids (Section 2.3), and an efficient diagnostics computation scheme for those grids (Section 2.4.2) were developed. In this chapter, these new methods are validated for use for GLORIA limb imager retrievals and their performance compared to more established techniques, both in terms of retrieval quality and computational cost, by performing 3-D tomography with simulated measurements. The last section of the chapter presents two small-scale tests for evaluating regularisation and irregular grid methods on their own, without doing a full test retrieval as in previous sections.

3.1 The GLORIA instrument

The Gimballed Limb Observer for Radiance Imaging of the Atmosphere (GLORIA) is an airborne IR limb imager. It is a Michelson interferometer and acquires spectra in the 770 to 1400cm^{-1} range (Riese et al., 2014; Friedl-Vallon et al., 2014). The spectral resolution depends on the configured measurement mode. The best possible spectral sampling of 0.0625 cm^{-1} is achieved in the so called *chemistry mode* used for retrieving a large number of trace species. One full interferogram is recorded in about 13 s in this mode. In *dynamics mode*, spectral

sampling is reduced to 0.2 cm^{-1}, but the faster acquisition rate of ≈5 s per interferogram allows for instrument panning, i.e., the observation direction with respect to aircraft heading alternates between 11 values in between 49° and 129°. 3-D tomography images are acquired in this mode. Instrument panning capability is also useful for 1-D retrievals, since the observation angle can be chosen so that the direction of highest horizontal sampling is aligned with the orientation of the most interesting structures in the atmosphere. An even faster version of dynamics mode mode with 0.625 cm^{-1} spectral resolution and more panning angle steps has been used in the past.

The detector of the spectrometer is a 2-D array with 256 × 256 physical pixels. The optics is designed to image the inner 128x128 pixels to a 4° × 4° field of view in both vertical and horizontal directions. The signals from the physical pixels are further co-added to improve signal-to-noise ratio. The vertical field of view allows to capture the full observable altitude range in one image without the need to scan vertically. The highest altitude at which atmospheric parameters can be retrieved is typically around the flight altitude, and the lowest altitude is typically 6 km in cloud-free conditions (atmosphere becomes optically thick and unsuitable for limb observation in GLORIAs spectral range at lower altitudes mostly due to the water vapour continuum). If optically thick clouds are present, the retrieval is limited to altitudes above the cloud tops.

All the measurement data used in this thesis was acquired while GLORIA was flying aboard the German HALO research aircraft operated by DLR (Deutsches Zentrum für Luft- und Raumfahrt, eng. German Aerospace Center). The test case with synthetic measurements in Section 3.2.1 also uses the flight path of an actual HALO flight. HALO is a modified Gulfstream G550 business jet, with certified ceiling of 15.5 km, maximum cruise speed of 940 km/h and range exceeding 10 000 km (DLR, 2020). In practice, the maximum altitude can only be achieved in the end of the flight, while initially HALO typically climbs to only about 12.5 km due to the weight of the fuel on board. The typical cruise speed during research flights is about 850 km/h.

Best horizontal resolution in tomographic retrievals of down to 20 km is achieved when the aircraft is flying around the observed air mass in a close-to-circular flight pattern while panning

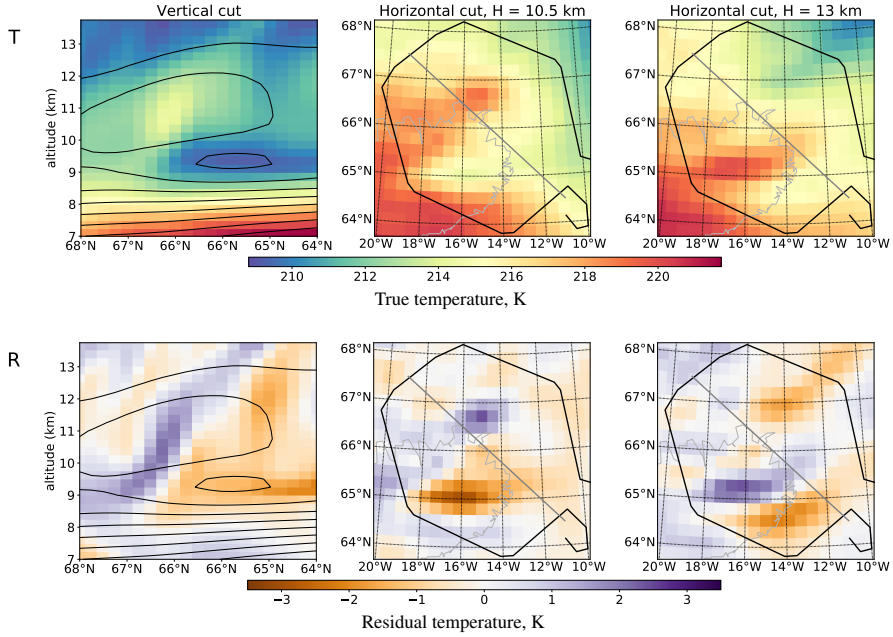

Figure 3.1: The first row (T) shows the ECMWF temperature data used to generate the synthetic measurements (true temperature). Second row (R) shows the temperature residual: the difference between the true temperature and the smoothed temperature field used as an a priori. In the first column, black lines represent contours of a priori temperature value. In columns 2 and 3: black line – flight path, grey line – position of cut shown in the first column, thin grey line – topography (Icelandic coastline visible).

the instrument (dynamics mode). Due to practical flight planning and aircraft navigation considerations, the actual tomography-optimised flight paths are typically hexagonal and around 400 km in diameter (Ungermann et al., 2010b; Krisch et al., 2017).

Both 1-D and 3-D retrievals are performed by means of inverse modelling, using the Jülich Rapid Spectral Simulation Code Version 2 (JURASSIC2). The radiative transfer model (Hoffmann et al., 2008) (employed as the forward model) uses the emissivity growth approximation method (Weinreb and Neuendorffer, 1973; Gordley and Russell, 1981) and the Curtis-Godson approximation (Curtis, 1952; Godson, 1953). The implementation of inverse modelling scheme described in Chapter 2 was also incorporated into JURASSIC2.

3.2 Simulated retrieval set-up

3.2.1 Test data

A hexagonal flight pattern intended for tomography was realised on 25 of January 2016, as part of flight 10 of the POLSTRACC measurement campaign. The flight path of the HALO research aircraft contained a regular hexagon with diameter (distance between the opposite vertices) of around 500 km over Iceland, which allowed for a high spatial resolution retrieval in the central part of this hexagon (Figure 3.1). The flight altitude throughout the hexagonal flight segment remained close to 14 km. For detailed information about this flight refer to Krisch et al. (2017).

The test case used in this chapter is based on the actual aircraft path, measurement locations, spectral lines used for retrieval and meteorological situation during this flight. Synthetic measurement data was used instead of real GLORIA observations: the forward model of JURASSIC2 was employed to simulate the observed radiances in the atmospheric state given by the ECWMF temperature and WACCM model data for trace gases. Simulated instrument noise was subsequently added to these radiances. This set-up allows us to use model data as a reference (the "true" atmospheric state) for evaluation of retrieval quality. The same set of simulated measurements was used for all test retrievals described in this chapter. These measurements were obtained by running the forward model on a very dense grid (about twice as dense in each dimension as those of the densest test retrievals). This was done to ensure that the discretisation errors in the simulated measurements would be minimal and would not favour any retrieval (as it could happen, if they were generated on the same grid). An evaluation of forward model errors on different grids is presented in Section 3.4.2.

The retrieval derives temperature and volume mixing ratios of O_3, HNO_3, CCl_4, and $ClONO_2$. Temperature and CCl_4 volume mixing ratio (VMR) are derived in the altitude range from 3 km to 20 km; O_3, HNO_3, $ClONO_2$ are retrieved from 3 km to 64 km. The latter three trace gases have larger volume mixing ratios above flight level and hence significant contributions to measured radiances from these high altitudes. Interpolated WACCM data was used as a priori for all trace gases. A priori data for temperature was obtained by applying

polynomial smoothing to ECMWF data. The retrieval is hence not supplied with the full temperature structure that was used to simulate the measurement. Therefore, the agreement between the retrieval result and the "true" atmospheric state, upon which the simulated measurements are based, cannot be achieved by overly restricting the solution to the a priori by regularisation.

3.2.2 Correlation length estimation

Table 3.1: Retrieval parameters

Entity	α_0	α_h	σ
Temperature	10^{-3}	10^{-1}	0.645 K
O_3	10^{-5}	10^{-3}	70.7 ppbv
HNO_3	10^{-5}	10^{-3}	902 pptv
CCl_4	10^{-5}	10^{-3}	2.13 pptv
$ClONO_2$	10^{-5}	10^{-3}	76.7 pptv

Regularisation weights α_0, α_h, (as in (2.8)) are used for retrieval A, the standard deviation σ (see (2.22)) used for retrievals B-D

The standard deviation σ and correlation lengths L_h and L_v in equation (2.20) can be obtained from statistical analysis of in situ measurement or model data. Rigorous derivation of these parameters for each retrieved trace gas and temperature would require detailed analysis of in situ measurement databases and is, therefore, out of scope of this study. However, the following rough approximation proved sufficient to improve upon retrieval results compared to the old regularisation scheme.

3-D tomographic retrievals are most useful for those trace gases that have high vertical gradients and complex spatial structure. The spatial correlation lengths of VMRs of such gases are mostly generated by stirring, mixing and other dynamical processes and are therefore similar. Furthermore, Haynes and Anglade (1997) and Charney (1971) estimated the

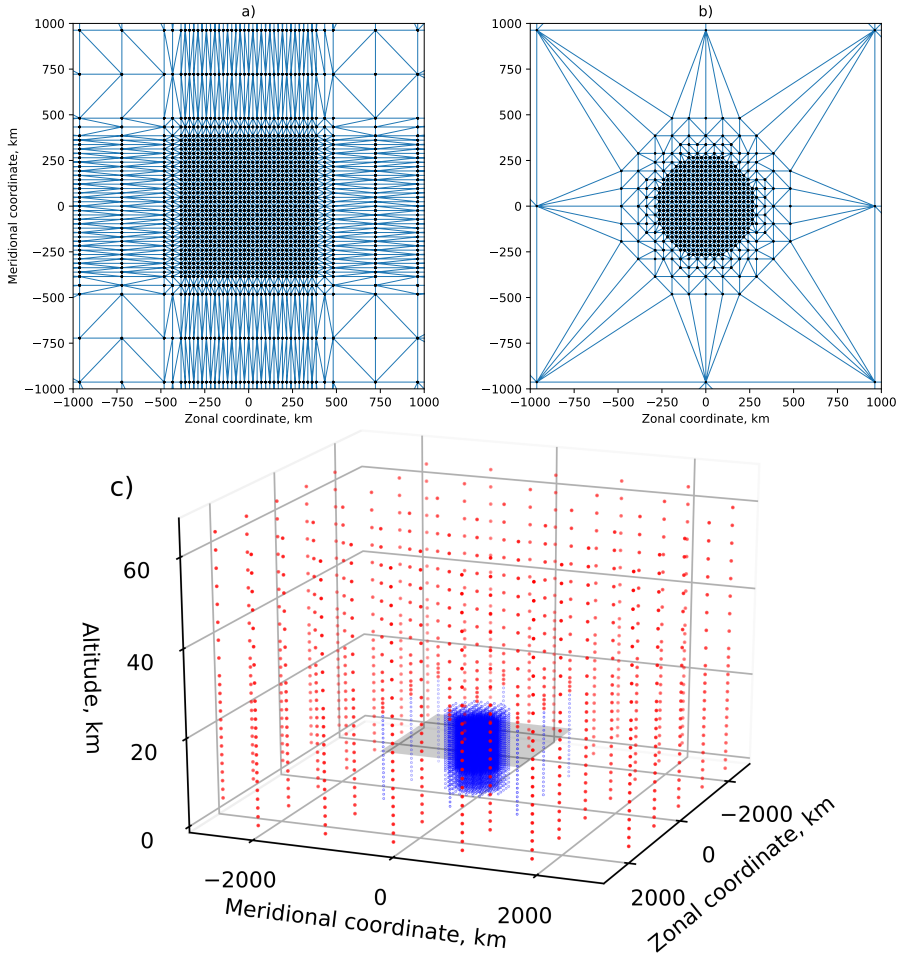

Figure 3.2: Panels (a) and (b): horizontal cuts of retrieval grids. Dots show grid points, blue lines indicate Delaunay cell boundaries. (a) shows the full initial grid for retrievals A, B, C (all horizontal layers of this grid are identical), (b) shows the thinned out grid for retrieval D (cut at 11 km). Panel (c): grid for retrieval D. Radial distance is defined as distance to the vertical line at the centre of the hexagonal flight path (66°N, 15°W). Points within the inner core (1000 km × 1000 km × 20 km) are shown in blue, other points – in red, shaded rectangle shows the position of horizontal cut in panel (b).

dynamically governed aspect ratio to be $\alpha \approx 200 - 250$ in lower stratosphere, and we expect less than that in the upper troposphere. Hence we will assume $L_h/L_v = 200$ for all trace

gases.

An analysis of spatial variability of some airborne in situ measurements was performed by Sparling et al. (2006). For ozone concentration $\chi(s, z)$, where s is the horizontal location and z is the altitude, they define fractional difference parameters

$$\Delta_{r,h} = \frac{2\,|\chi(s+r, z+h) - \chi(s, z)|}{[\chi(s+r, z+h) + \chi(s, z)]}, \tag{3.1}$$

$$\Delta_r = \lim_{h \to 0} \Delta_{r,h} \tag{3.2}$$

and provide the dependence of the standard deviation $\sigma(\Delta_r)$ on the horizontal separation r. If the typical spatial variation in ozone VMR is significantly smaller than the mean ozone VMR $\langle\chi\rangle$, one can approximate

$$\Delta_r \approx \frac{|\chi(s+r) - \chi(s)|}{\langle\chi\rangle}. \tag{3.3}$$

Then, using the covariance relation (2.15) and various properties of the normal distribution, we get

$$\sigma^2(\Delta_r) = 2\left(\frac{\sigma}{\langle\chi\rangle}\right)^2 \left(1 - \frac{2}{\pi}\right)\left(1 - \exp\left(-\frac{r}{L_h}\right)\right). \tag{3.4}$$

By comparing this to experimental results of Sparling et al. (2006), we estimate $L_h = 200\,\text{km}$. Using the aspect ratio argument above, we also set $L_v = 1\,\text{km}$.

The spatial structure of retrieved temperature differs from that of the trace gases. It is determined not only by mixing and stirring, but also radiative processes and dynamical processes such as gravity waves. Radiative transfer tends to erase some of the fine vertical structure determined by isentropic transport, hence one should use a greater vertical correlation length than in the case of trace gases. Gravity waves have a variety of length scales, but due to the finite resolution and integrating properties of the instrument not all of them can be retrieved. Following the gravity wave observational filter study for the GLORIA instrument in Krisch et al. (2017) we can estimate lowest observable horizontal wavelengths of gravity waves to be $\lambda_h \sim 200\,\text{km}$ and lowest vertical wavelength $\lambda_v \sim 3\,\text{km}$. λ_h coincides with the dynamically determined correlation length $L_h = 200\,\text{km}$, so this value should be appropriate

for temperature as well. The λ_v limit is not only determined by instrument resolution, but is also related the fundamental properties of gravity waves. Preusse et al. (2008) gives the following expression for the gravity wave saturation amplitude

$$\hat{T}_{\max} = \frac{\lambda_v \bar{T} N^2}{2\pi g}, \tag{3.5}$$

where $\bar{T}$ is the mean temperature and N is the Brunt–Väisälä frequency. In typical lower stratosphere conditions and $\lambda_v = 3\,\mathrm{km}$ the equation (3.5) gives $\hat{T}_{\max} \approx 4\mathrm{K}$. Since gravity waves are usually not saturated and considering typical measurement error (see 3.3.3), waves of significantly shorter wavelengths would probably not be observed. We hence set $L_v = 3\,\mathrm{km}$. Time series of measurements at a fixed point in the atmosphere are then used to approximate the standard deviations σ for all retrieved quantities (Table 3.1). Our choice of σ value for temperature, in particular, may seem rather low. This is related to the choice of a priori: smoothed ECMWF data was used instead of climatological values that would have been more typical in this case. Such an a priori can be expected to match the large scale structures of real temperature more closely, thus reducing the forward model errors in poorly resolved areas and improving the results. It is particularly useful for resolving fine structures, such as gravity waves, which were the main scientific interest of the measurement flight (Krisch et al., 2017) used as a basis for test retrievals. A likely closer match between a priori and retrieval thus requires a lower σ value, that, in this set-up, represents expected strength of gravity wave disturbances, rather than full thermal variability of the atmospheric region in question.

3.3 Results

3.3.1 Test retrievals

The test data described in the previous section was processed with several different regularisation set-ups and retrieval grids. Here we present the results for four different runs.

Firstly, as a reference, the latest version of JURRASIC2 without the implementations

Table 3.2: Grid densities in different regions for retrieval D (in kilometres)

Radius	< 300	300-400	400-550	550-1500	> 1500
Altitude	Horizontal grid separation				
1-5	100	100	100	1000	1000
5-12.5	25	50	100	1000	1000
12.5-14.5	25	25	100	1000	1000
14.5-17	25	50	100	1000	1000
17-20	100	100	100	1000	1000
20-64	500	500	500	1000	1000
Altitude	Vertical grid separation				
1-5	1	1	1	1	2
5-12.5	0.125	0.25	1	1	2
12.5-14.5	0.125	0.125	1	1	2
14.5-18	0.125	0.25	1	1	2
18-24	2	2	2	2	2
24-64	4	4	4	4	4

Table 3.3: Grid point altitudes for retrieval A (in kilometres)

Altitude range	Vertical grid separation
1 – 5	1
5 – 20	0.25
20 – 25	1
28 – 64	4

of any new algorithms described in this thesis was used (retrieval A). It uses a rectangular grid. Vertical spacing for this grid is given in Table 3.3. As required for the rectilinear grid, the number and distribution of points is the same in each altitude (Figure 3.2a). For this reference run, a first order regularisation (2.7) with trilinear interpolation (Bai and Wang, 2010) was used. The regularisation weights, as defined in (2.8), are given in Table 3.1. These are typically tuned ad-hoc, i.e., adjusted by trial-and-error until optimal retrieval results can be achieved, starting from the default values obtained using the L-Curve method (Hansen and O'Leary, 1993). While tuning, retrieval results are compared against the atmospheric state used to generate the synthetic measurements. When using real observations, results are validated against in situ measurements and model data.

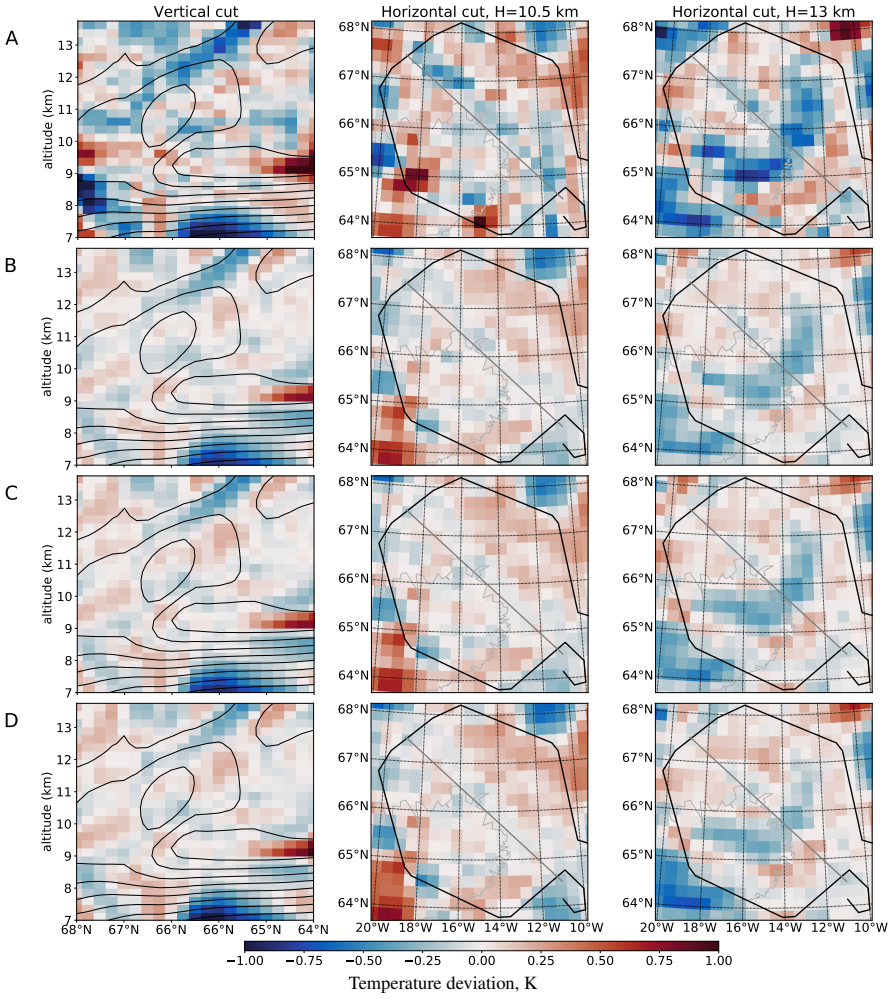

Figure 3.3: Panels show difference between retrieved temperature and true temperature of the simulated atmosphere. Rows A-D show results of respective retrievals. In the first column, black lines represent contours of a priori temperature value. In columns 2 and 3: black line – flight path, grey line – position of cut shown in the first column, thin grey line – topography (Icelandic coastline visible).

In order to evaluate the performance of second order regularisation, retrieval B was performed. The grid and interpolation methods were identical to retrieval A, but the regularisation was replaced with the second order scheme from equations (2.20), (2.22) and correlation

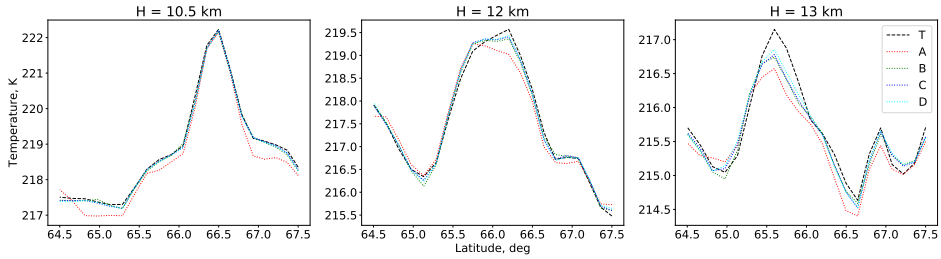

Figure 3.4: Retrieved temperature at different altitudes in the vertical cut shown in Figures 3.1 and 3.3. Line T represents the true temperature of the simulated atmosphere, A-D: respective retrievals.

lengths derived in section 3.2.2 from in situ observations. These parameters were not tuned subsequently.

We compare the quality of different retrievals by inspecting the differences between the retrieved temperature and temperature used to generate the synthetic measurements ("true" temperature). These differences are shown on horizontal and vertical slices of the observed atmospheric volume in Figure 3.3. Figure 3.4 shows the variation of the retrieved and true temperatures on horizontal lines in order to visualise the response of retrievals to different spatial structures in true temperature.

Comparison of Figure 3.3 rows A and B shows the effect of the new regularisation (2.20). The new algorithm (retrieval B) demonstrates better agreement with the true temperature. It shows markedly less retrieval noise in the central area, as well as better results (less effect of a priori) just outside it, at the edges of the vertical cut shown in Figure 3.3. Considering also that, unlike A, the regularisation strength of B was not manually tuned for this test case in particular, we can conclude that the new regularisation performed better in this test case.

The third retrieval (C) was performed on the same set of grid points as B and with the same input parameters, but the grid was treated as irregular, i.e., a Delaunay triangulation was found, the algorithms described in section 2.2 were used for regularisation. A horizontal cut of the Delaunay triangulation for this grid is shown in Figure 3.2a. By comparing B and C one can evaluate the agreement between the old interpolation, derivative calculation and volume integration techniques for rectilinear grids and their newly developed irregular-

grid-capable alternatives. The temperature fields from retrievals B and C are very similar (Figure 3.3), which confirms that the new Delaunay triangulation based code gives consistent results when run on traditional rectilinear grids.

Finally, retrieval D was performed with the same input parameters and methods as C, but using only the subset (22 %) of the original grid points to reduce computational cost. These points were chosen so that grid density would be highest in the volumes best resolved by GLORIA and sparser where little or no measurement data is available. In particular, a set of axially symmetric regions around the centre of original retrieval (i.e., symmetric w.r.t. vertical axis at 66°N, 15°W) was defined as shown in Table 3.2. Points were removed from the original grid to achieve the specified vertical and horizontal resolutions for each region, resulting in the grid shown in Figure 3.2. Results changed little compared to retrieval C. Most of the minor differences between C and D occur near the edges of the hexagonal flight path (Figure 3.3). Even though the grid spacing for retrieval D is still the same as C in some these areas, larger grid cells nearby have some effect on their neighbours. Note also that C and D retrievals tend to differ most in the areas where the agreement between each of them and the true temperature is relatively poor and diagnostics predict lower accuracy (Figure 3.5), so D can be considered to be as good as C in well-resolved areas. Unphysical temperature structures far outside the measured area like the one partially seen at 64°N, 20°W are not unique to this retrieval, they just occur a little closer to the flight path in this case due to the coarser grid outside the hexagon.

3.3.2 Computational costs

JURASSIC2 finds an atmospheric state minimising (2.7) iteratively. In each iteration it first computes a Jacobian matrix of the forward model, hence obtains a Jacobian of the cost function (2.7) and then minimises the cost function using the Levenberg-Marquardt (Marquardt, 1963) algorithm and employing conjugate gradients (CG; Saad, 2003, Hanke, 1995) to solve the linear equation systems involved. The forward model is then run to simulate the measurements for the new iteration of atmospheric state.

All calculations were performed on the Jülich Research on Exascale Cluster Architectures

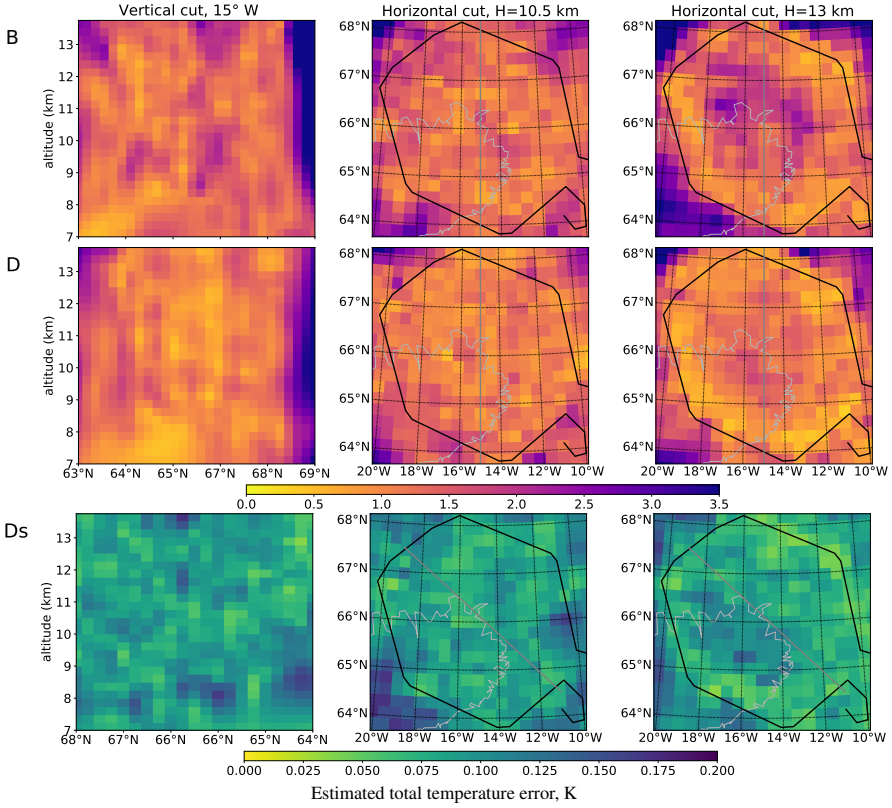

Figure 3.5: Panels B and D show the Monte Carlo estimate of the total temperature error the retrievals B and D would have, if the measurements were real. Panel Ds shows an error estimate for the synthetic retrieval D (this assumes that unretrieved quantities, e.g. pressure, are known exactly). In columns 2 and 3: black line – flight path, thick grey line – position of cut shown in the first column, thin grey line – topography.

(JURECA) supercomputer operated by the Jülich Supercomputing Centre (Jülich Supercomputing Centre, 2016). Each retrieval was executed in parallel on 4 computation nodes, each with 24 CPU cores (twin Intel Xeon E5-2680 v3 CPU's) and 128 GB of system main memory.

Table 3.4 shows the time required for different parts of calculation averaged over 3 identical runs (although $< 1\%$ variation was observed). The "Other calculations" field mostly includes time required by input and output, but also preparatory steps, such as Delaunay triangulation in the case of retrievals C and D.

The results in Table 3.4 reveal the impact of the new methods on computation times. The new, more complex regularisation results in slower convergence in the conjugate gradient calculation, making retrieval B about 6% more expensive than A. The Delaunay triangulation, however, decreases Jacobian calculation costs by roughly 25%, even the one used on the same grid as the old approach. This has to do with the fact that interpolation based on Delaunay triangulation only requires 4 values of the interpolated quantity at neighbouring points, and linear interpolation in three directions requires 8, thus resulting in more non-zero terms in the Jacobian. The time required for initialisation of the Delaunay interpolation and derivatives, including construction of the matrix $\mathbf{S}_a^{-1}$, increases rather fast with grid size with current implementation, contributing to "other calculations" of retrieval C. Further optimisation of this step is possible and will be implemented in the future. In total, the new retrieval (C) is 9% faster then the old approach (A) while using the same grid.

Table 3.4: Computational cost of retrievals (calculation times given in minutes)

Retrieval	A	B	C	D
Number of grid points	302526	302526	302526	54580
Jacobian calculation	134.4	133.2	101.2	61.3
Minimisation (CG)	4.2	14.9	12.8	6.0
Forward model	2.5	2.5	2.6	2.6
Other calculations	5.6	4.4	17	3.0
Total elapsed time	146.7	155.0	133.6	72.9

Retrieval D gives a further 45% reduction of computation time by removing 82% of points in the grid. A speedup of such order was expected. Only a minority of grid points contribute to a forward model (and hence Jacobian) calculations, and JURASSIC2 code is heavily optimised for sparse matrix operations. Most of the grid points contributing to the forward model are in the areas well resolved by the instrument and thus cannot be removed from the grid without compromising the final data products. Therefore, the actual savings in computation time mostly come from removing points above flight level and choosing a more appropriate non-rectangular shape for the densest part of the grid when measurement geometry requires that. Some of the points above flight path must be included since infrared radiation from there is measured by the instrument, but very little information about atmosphere far above flight

level can be retrieved, so very low grid densities are sufficient (Table 3.2).

3.3.3 Diagnostics

We follow use the Monte Carlo method described in Section 2.4.2 as the main technique for error estimation. Results for retrievals B and D are presented in Figure 3.5 B, D. They show the total error estimate for temperature based on the sensitivity of temperature value to (simulated) instrument noise and all other retrieved atmospheric quantities as well as expected error of non-retrieved quantities (e.g. pressure). These results tell us what temperature errors we could expect if the retrievals in question were performed with real data. The panel Ds shows an error estimate based on (simulated) instrument noise and uncertainties of retrieved parameters only. In the case of a synthetic retrieval, unretrieved parameters such as background gases or instrument uncertainties, that immediately influence the simulated measurements, are known exactly. Therefore, panel Ds is a Monte Carlo evaluation of the error expected for our test retrieval with simulated measurements (Figure 3.3D), and the magnitude of this deviation is indeed similar.

These results confirm that temperature can only be retrieved with high accuracy within the flight hexagon or very close to the actual path. Also, the error estimates are higher in the central area of hexagon close to flight altitude, in agreement with test results (compare column 3 of Figures 3.3 and 3.5).

Recall the regularisation method from Section 2.4.1, which is only suitable for computing error estimates for a small number of grid points. We applied this deterministic method to one point in the centre of the hexagon (66° N, 15° W, 11.75 km altitude) for retrieval B. The total temperature error was found to be 1.27 K and agrees with Monte Carlo result (1.25 K) at this point within 2%, which is an excellent accuracy for an error estimate.

3.4 Stand-alone tests for retrieval methods

Additional testing was carried out to directly evaluate the performance of particular newly developed algorithms separately from the full retrieval. Two of the more important ones are

presented here.

3.4.1 Validating the numerical implementation of regularisation

The equation (2.22) was used to construct precision matrices $\mathbf{S}_\mathrm{a}^{-1}$ directly, since constructing a covariance matrix $\mathbf{S}_\mathrm{a}$ explicitly and inverting it would be prohibitively computationally expensive. While the equation (2.20) was derived analytically, its discrete implementation cannot be exact, which raises the question whether our precision matrices still have required properties, namely, whether they are still inverses of $\mathbf{S}_\mathrm{a}$ that obeys equation (2.15). Clearly, this can only be verified directly for a small test case, where covariance matrices are small enough to be inverted. Also, employing matrix norms to compare matrices is not very useful in this case, as the directly computed $\mathbf{S}_\mathrm{a}^{-1}$ is based on finite difference derivative estimates which do not work very well at grid boundaries. This is not a problem for the retrieval, which, by design, approaches a priori near grid boundaries, but it has strong effects on matrix norms. Instead, we compared the covariance matrices by using them to compute the norms of several test vectors, that represent typical structures expected for that covariance.

Precision matrix $\mathbf{S}_\mathrm{a}^{-1}$ was constructed for one entity on a regular $20 \times 20 \times 20$ grid (grid constant 1 in each direction) using the same techniques as for retrieval B ($\sigma = 1$ and $L_v = L_h = L = 2$). Then a covariance matrix was explicitly constructed for the same grid using equation (2.15) and inverted to obtain the precision matrix $\hat{\mathbf{S}}_\mathrm{a}^{-1}$. A set of vectors $\boldsymbol{x}_\phi$ – discrete representations of a "Gaussian wave packet" disturbance

$$\phi\left(\boldsymbol{r}\right) = \exp\left(-\frac{\|r\|^2}{d^2}\right)\cos\left(\boldsymbol{k}\cdot\boldsymbol{r}\right) \tag{3.6}$$

was computed. The parameter d was chosen so that the amplitude of the wave would decay to at most 0.01 at the grid boundary, thus suppressing edge effects. Two different wavelengths, namely $\lambda = 15$, 20, in grid units, and were chosen and 50 $\boldsymbol{k}$ values pointing at every possible direction were generated for each wavelength (i.e. $\|\boldsymbol{k}\| = 2\pi/\lambda$). Then, for each of the resulting 100 disturbances the norms $\|\boldsymbol{x}_\phi\|_p$ and $\|\boldsymbol{x}_\phi\|_t$, where $\|\boldsymbol{x}_\phi\|_\mathrm{p}^2 = \boldsymbol{x}_\phi^T\mathbf{S}_\mathrm{a}^{-1}\boldsymbol{x}_\phi$ and

$\|\boldsymbol{x}_\phi\|_\mathrm{t}^2 = \boldsymbol{x}_\phi^T \hat{\mathbf{S}}_\mathrm{a}^{-1} \boldsymbol{x}_\phi$, were calculated, as well as their relative difference

$$\delta = 2\frac{|\|\boldsymbol{x}_\phi\|_\mathrm{p} - \|\boldsymbol{x}_\phi\|_\mathrm{t}|}{\|\boldsymbol{x}_\phi\|_\mathrm{p} + \|\boldsymbol{x}_\phi\|_\mathrm{t}}. \tag{3.7}$$

For the case $\lambda = 15$ we found that the mean δ value was 0.050, with standard deviation 0.0042, and for the case $\lambda = 20$ mean was 0.036, with standard deviation 0.0007. We believe that precision of this order is sufficient for regularisation purposes.

3.4.2 Forward model tests

Table 3.5: Forward model tests

Measurements	original + noise	A	C	D
$\Delta(\boldsymbol{y}, \boldsymbol{y}_\mathrm{orig})$	0.0193	0.0035	0.0036	0.0047

Difference in forward model results, compared to original synthetic measurement set without noise. A-D refer to forward model results of respective retrievals.

As pointed out in Section 3.2.1, the same measurement set, synthetically generated on dense grid, was used for retrievals A-D. This provides an easy way to verify if the forward model is performing consistently on different grids: run it on each grid, based on the "true" atmospheric state and compare the results with the synthetic measurements from the dense grid. In our test case, the radiances are calculated for $n = 31$ spectral windows. If vector $\boldsymbol{y}$ represents a set of radiances, and $\boldsymbol{y}_i$ represents the radiances at i-th spectral window, we evaluate the difference between those vectors with the parameter

$$\Delta(\boldsymbol{y}, \boldsymbol{y'}) = \frac{2}{n}\sum_i^n \frac{\|\boldsymbol{y}_i - \boldsymbol{y}'_i\|_2}{\|\boldsymbol{y}_i\|_2 + \|\boldsymbol{y}'_i\|_2}, \tag{3.8}$$

where $\|\cdot\|_2$ is the Euclidean norm. The results of this comparison are presented in Table 3.5. Forward model for retrievals A and C used the same grid, but A used trilinear interpolation, and C used Delaunay interpolation. We can see that the change in interpolation does not

introduce significant errors (compared to those introduced by the grid change). Thinned out grid and Delaunay interpolation was used for grid D. Note that the simulated measurements that were actually used also have simulated instrument noise added to them. The results clearly show that the effects of different discretisation are well below instrument noise level. Also, the error is lower than our generally assumed forward model error of 1-3% (Hoffmann, 2006).

Chapter summary

As shown by a case study with synthetic data, the newly developed regularisation scheme, combined with irregular grid retrieval methods employing Delaunay triangulation, improves both upon the quality and the computational cost of 3-D tomography. It also eliminates grid dependence and the need to tune parameters for each use case. The few remaining physical parameters required can be derived from in situ measurements and model data. Tests show that an 82% reduction in the number of grid points and a 50% reduction in total computation time, compared to previous methods, can be achieved without compromising results. The computationally efficient Monte Carlo technique newly adopted for the accuracy estimation of 3-D retrievals was also validated.

Chapter 4

Rossby wave breaking during WISE campaign

This chapter introduces GLORIA measurements from two research flights of the HALO research aircraft, their analysis and scientific evaluation. During these flights, GLORIA observed different stages of the same Rossby wave (RW) breaking event over the North Atlantic. The flight plan was aimed to study the structure and dynamics of the breaking wave as well as mixing and air mass transport between stratosphere and troposphere. Both 1-D retrieval and 3-D tomography results are introduced and discussed in detail.

The WISE measurement campaign

The Wave Drive Isentropic Exchange (WISE) measurement campaign was carried out August to October 2017 from Shannon Airport in Ireland. A total of sixteen research flights of the German HALO research aircraft were performed, mostly over the North Atlantic, Scandinavia and western Europe. One of the major science themes was horizontal transport from tropical troposphere into the extra-tropical lower stratosphere above the extra-tropical tropopause layer. This is the most important pathway for water vapour, among other tracers, during summer and autumn months (Ploeger et al., 2013) and is strongly influenced by RW breaking (McIntyre and Palmer, 1983). Seasonal variability of such transport and Rossby wave activity are related (Postel and Hitchman, 1999), and deep intrusions of low latitude air into high

latitudes associated with RW breaking are reflected in the observed ozone and water vapour concentration day-to-day variability (Vogel et al., 2016). The HALO aircraft was equipped with multiple in situ instruments: their combined measurements allowed to deduce age-of-air spectra providing insights into transport pathways and time scales. On the other hand, the high vertical resolution of GLORIA and 3-D tomography capability was very well suited for investigating stirring, mixing and filamentation processes.

4.1 Measurement flights

4.1.1 Synoptic situation

On 7 October 2017 an onset of a Rossby wave breaking event was predicted over the western part of North Atlantic. A research flight was planned to probe the UTLS above the polar jet (Figure 4.1a). The HALO aircraft took off from Shannon, Ireland, at at around 12:30 UTC and landed just after 20:00 UTC. The GLORIA instrument performed well and measured for the whole duration of the flight. These measurements were used for 1-D retrievals, and the resulting profiles were combined into a 2-D data product (curtain) along the flight path.

A hexagonal flight pattern in the Rossby wave breaking region itself was flown between 16:00 UTC and 17:45 UTC, allowing for a 3-D tomographic analysis of the volume. Due to the limited aircraft range, flying a full hexagon this far from the operating base was not possible, hence only 5 sides were executed. Also, after flying 2 of the 5 sides, HALO climbed from the altitude of 13.4 km to around 13.9 km. For best results and easier processing, one would wish to avoid climbing in the middle of the tomographic data acquisition. In this case, however, flying at the higher altitude was not possible earlier due to the weight of the remaining fuel. Also the benefits of flying the last 3 hexagon sides higher and hence observing a wider altitude range were deemed more important. This choice was further motivated by the presence of optically thick clouds at low altitudes. In parts of the hexagon, cloud tops reached to almost 10.5 km altitude, thereby restricting the altitude range available for retrieval. Another complication for producing 3-D data was the high wind speeds of the polar jet, reaching more than 40 m/s, resulting in significant advection of air masses during the measurement acquisi-

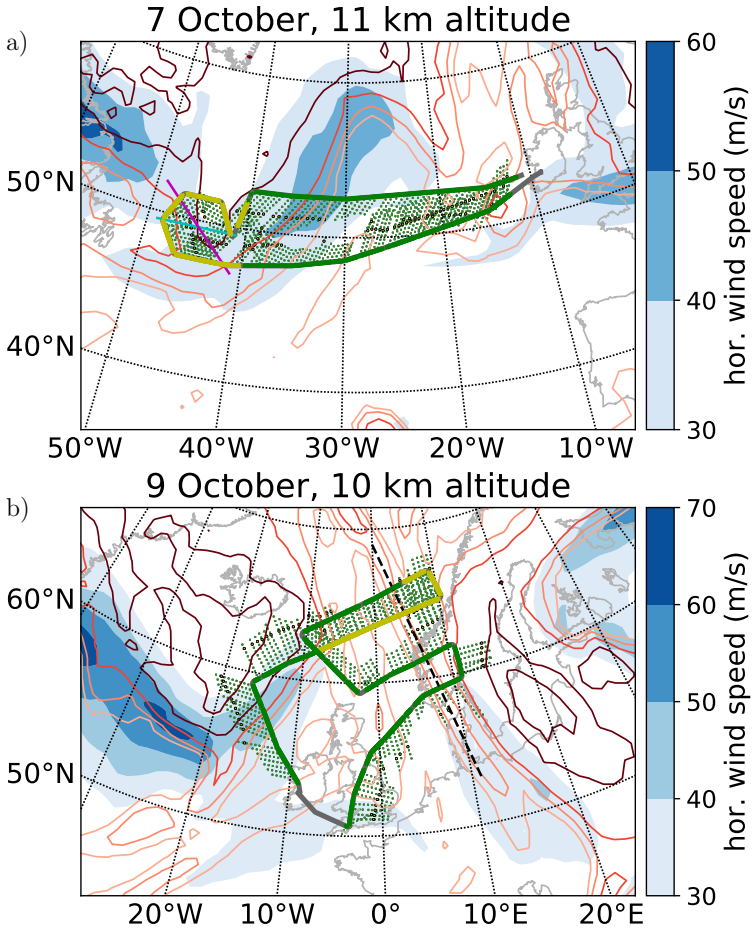

Figure 4.1: Synoptic situation during measurement flights. Flight track shown in green for chemistry mode, yellow for dynamics mode measurements. Tangent points are depicted as green dots. Potential vorticity contours for 2, 4, 6, and 8 PVU, respectively, are shown in increasingly darker reddish colours. Magenta and cyan lines in panel a) mark the position of cuts shown in Figure 4.6, dashed black line in panel b) marks an old air filament (see main text for discussion)

tion time (see Section 4.4 for solution to this particular problem). The measured air masses could be successfully reconstructed in 3-D despite of these challenges (see Section 4.1.2). The tomographic retrieval is complemented by 2-D data (curtains of profiles obtained from 1D retrievals) of the region immediately east of the hexagon, which also proved to be of interest.

By 9 October 2017, the wave breaking event was at its final stage and most of the air masses that were present in the hexagon flown two days before were stretched into a thin filament extending from 70°N, 0°E to 51°N, 12°E. This filament can be seen as an elongated 2 PVU contour in Figure 4.1b and is highlighted by a dashed magenta line. A research flight was flown to investigate the late stage of this RW breaking by measuring this filament.The aircraft crossed the filament a total of four times during this flight, as seen in Figure 4.1b. The flight lasted from 08:30 UTC till 17:00 UTC. In this work, we present only 2-D data products from this flight.

4.1.2 Retrievals

Table 4.1: Spectral windows for 3-D retrieval

#	Spectral range, cm^{-1}	#	Spectral range, cm^{-1}
1	791.0 - 793.0	6	980.0 - 984.2
2	863.0 - 866.0	7	992.6 - 997.4
3	892.6 - 896.2	8	1000.6 - 10006.2
4	900.0 - 903.0	9	1010.0 - 1014.2
5	956.8 - 962.4		

Table 4.2: Regularisation parameters for 3-D retrieval

Parameter	Value, ppbv	Parameter	Value, km
σ_{O_3}	50	ρ_h	250
σ_{HNO_3}	0.12	ρ_v	1

The 3-D retrieval of ozone and nitric acid (HNO_3) was performed using radiances from the spectral windows given in Table 4.1. The a priori data for air temperature and pressure was taken from the European Centre for Medium-Range Weather Forecasts (ECMWF; Dee et al., 2011) operational analyses. Whole Atmosphere Community Climate Model (WACCM; e.g. Garcia et al., 2007) data was chosen as a priori for ozone and HNO_3. The spectral windows used for the 3-D retrieval are presented in Table 4.1, the regularisation parameters used are shown in Table 4.2. Refer to Section 2.2.1 for detailed explanations of their purpose and effect. For this retrieval, the standard deviations σ_{O_3} and σ_{HNO_3} were obtained by computing the

standard deviation of in situ data for each tracer (shown in Section 4.2.2 for result validation). In this late stage of a Rossby wave breaking event the structures are particularly stretched and a higher ratio of horizontal and vertical correlation lengths $\eta = \rho_h/\rho_v$ of 250 was used. This higher ratio is consistent with values for the lowermost stratosphere (Haynes and Anglade, 1997) and also seems to match the aspect ratios of structures that form in CLaMS backward trajectory runs (Section 4.2.2). The final values of ρ_h and ρ_v were then selected to optimise the resolution of the retrieval.

4.1.3 Backward trajectories

Backward trajectory calculations from the chemical Lagrangian model of the Stratosphere (CLaMS; McKenna et al. 2002) were used for measurement data analysis. The model was driven by winds obtained from ECMWF data. An air parcel was placed at each grid point of the GLORIA data product, and the trajectories of these parcels were traced back for up to 1 month. Mixing and chemical processes, which are normally included in the CLaMS model, are not used for backward trajectory runs. One of the main uses of backward trajectories was to determine the "age-of-air", i.e. time that an air parcel in question spent in stratosphere. The maximum potential vorticity gradient tropopause (Kunz et al., 2011) was used to define stratosphere and troposphere for the backward trajectories.

4.2 Results and analysis

4.2.1 7 October flight: 2-D data

In this section, we present the GLORIA 2-D data products. They were generated along most of the flight path (Figure 4.1a). The measured volume mixing ratios of ozone, water vapour and nitric acid are presented in Figure 4.2. The retrieved values are shown as functions of time and altitude, but it is important to remember that the GLORIA 2-D curtains do not represent a vertical cut through the atmosphere along the flight path but a slant curtain (see Figure 1.2). At flight altitude, the data shown is valid ∼10 km to the right of the aircraft, while at lowest altitude this distance increases to up to 250 km. The locations of the tangent

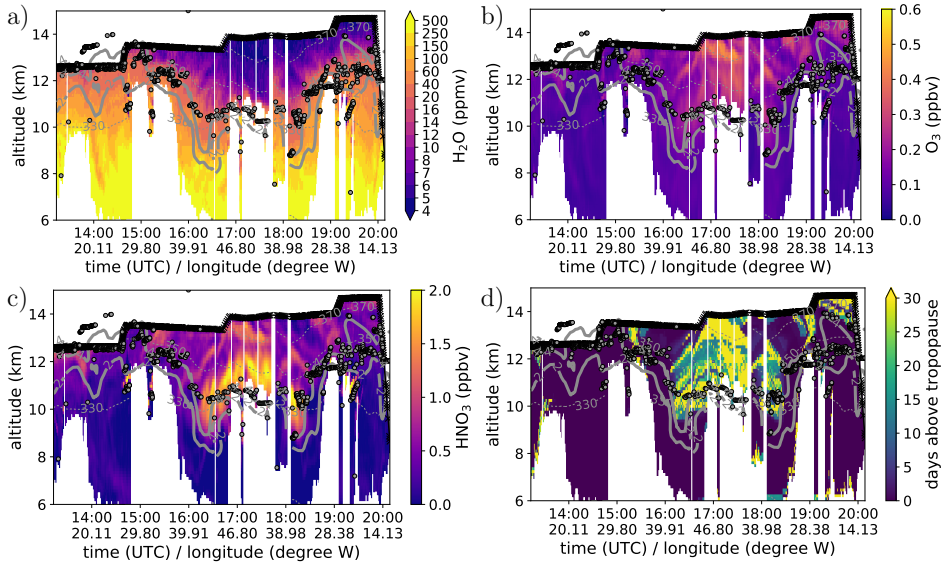

Figure 4.2: Water vapour, ozone and nitric acid 2-D retrieval data. Isentropes are shown as thin dashed lines, 2 and 4 PVU contours – thick solid lines, thermal tropopause – dots.

points of the observations are shown in Figure 4.1a. The missing data in Figure 4.2 is due to aircraft manoeuvres and optically thick clouds. In the case of cloud presence, only the data above cloud top is available. The retrieval of 2-D data was also performed for the hexagonal part of the flight path (from 16:15 to 17:42 UTC) for consistency, even though the 3-D data is available for that part of the flight. 2-D data products are formed by combining a series of profiles from 1-D retrievals. Each 1-D retrieval is valid at the time of measurement, hence 2-D data product does not have a single valid time, the data js valid at the measurement acquisition time.

Generally, water vapour has high volume mixing ratios in the troposphere and is much less abundant in the stratosphere due to freezeout in particular around the tropical tropopause. O_3 and HNO_3 are more abundant in stratosphere, where they are generated by photolysis, and less abundant in the troposphere. Generally these two gases have a compact positive correlation in the deep stratosphere. The correlation is attributed mostly to source and sink regions being similar for the two gases, and not a result of chemical interactions between them

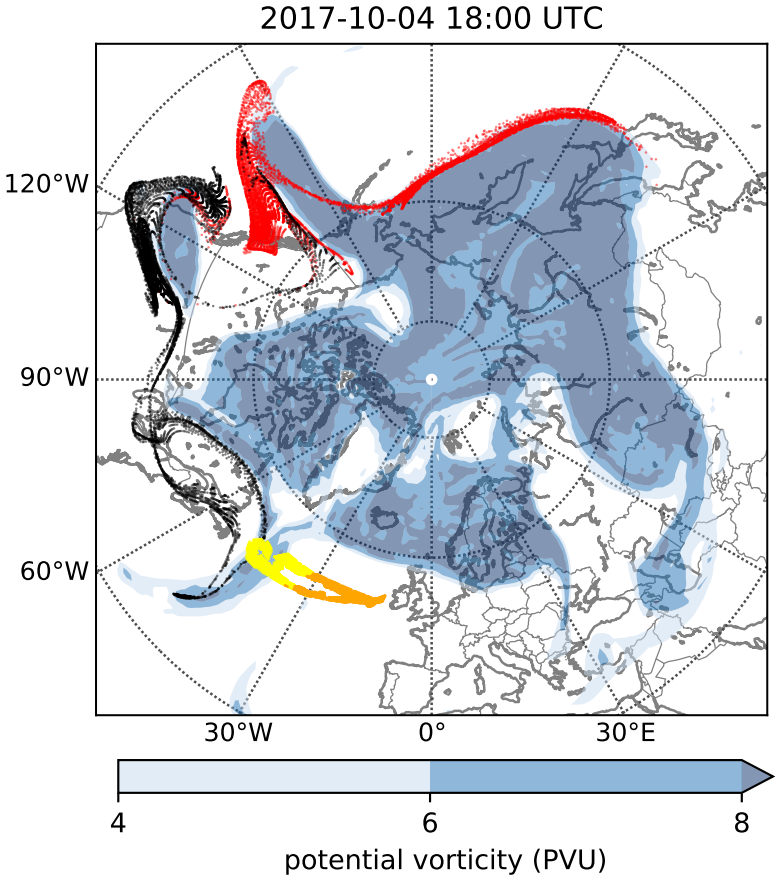

Figure 4.3: Air mass origin plot for the retrieved 2-D data. Horizontal cut at 11 km altitude 3 days before measurement flight is shown. Locations of GLORIA observations on 7 October: yellow - near polar jet (west from 30° W, PV > 1 PVU), orange – away from jet (all the rest). The positions of "yellow" air parcels 3 days before measurement are shown in red, of "orange" air parcels – in black.

(Section 4.2.3; Popp et al. 2009). Retrievals generally confirm the aforementioned trends, but also show heavily filamented structures in all the tracers presented here. There is a clear positive correlation between ozone and nitric acid: ozone-rich air masses tend to have high nitric acid concentrations and vice versa. One can also see negative correlation between water vapour and ozone (or, alternatively, between water vapour and nitric acid), especially around

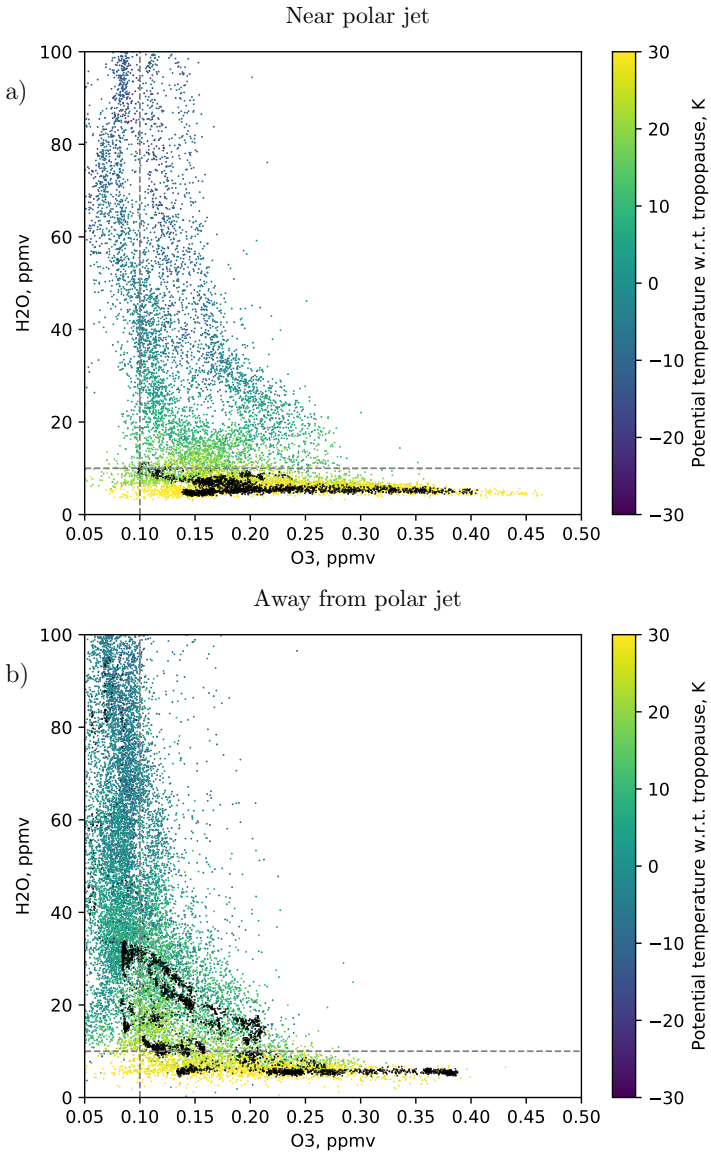

Figure 4.4: Ozone – water vapour tracer-tracer plots from 7 October flight. Black dots represent *in situ* measurement data at flight altitude. O_3 was measured by FAIRO (Zahn et al., 2012), H_2O – by FISH (Zöger et al., 1999). Dots of the shown colour scale – GLORIA data.

16:15 and 18:30 UTC, where the H_2O structure shows more filamentation. This suggests that the whole structure was formed by STE: air parcels rich in ozone and nitric acid (old air) come from higher up in the stratosphere, while wet air masses have relatively recently resided in the troposphere (young air).

The origins of the filaments were investigated with the help of CLaMS backward trajectories. The typical mixdown time scale for lower stratosphere in the Rossby wave surf zone is of the order of one month (Juckes and McIntyre, 1987). Hence, in this region, one may expect small scale ozone-poor structures to be a consequence of transport across the dynamical tropopause within the last month. Based on this reasoning, we plotted the "age" (i.e., time spent above the maximum potential vorticity gradient tropopause[1]) of each stratospheric air parcel observed by GLORIA (Figure 4.2d). There is good agreement between young air masses in this plot and ozone-poor and HNO_3-poor air in GLORIA retrieval. Almost all ozone rich (>0.25 ppmv) air masses, including thin filaments, have stayed in stratosphere for more than one month. Younger air, conversely, is almost always ozone poor. Also, wet air filaments correspond to young air masses, that can be seen best around 16:15, 17:50 and 18:40 UTC. Unfortunately, the air mass within the hexagonal flight pattern (16:15 to 17:42 UTC) was very dry, significant water vapour structures could only be found around the very edges of the hexagon and were advected outwards while this pattern was flown. The 3-D tomographic water vapour retrieval was therefore not performed.

HALO took off from Ireland, which was, at the time of the flight (7 October), south of polar jet and therefore not directly effected by air masses of the polar UTLS, the polar jet and Rossby waves that shape it. One can clearly see the jet (in wind speed) and Rossby waves (in PV) in Figure 4.1a. Conversely, the western part of the flight, including the hexagonal flight pattern, is directly on top of the polar jet and therefore heavily influenced by it and the RW surf zone. To illustrate this difference, we divided the observed air masses into those "near polar jet" (we defined these as air masses observed at locations west of 30°W and with PV > 1 PVU at 11 km altitude), and "away from the jet" (all the rest). The locations of

[1]Note that this definition of age is different from the classical one, which is the elapsed time since an air parcel enetered the stratosphere in the region of tropical tropopause in particular. Air masses that have just crossed the extratropical tropopause are considered young with our definition here.

observation for these air masses are shown in yellow and orange, respectively, in Figure 4.3. The PV at 11 km is plotted there as well and shows Rossby waves. The polar jet is located on the edges of the high-PV area (see Figure 4.1). The backward trajectory calculations show the position of the observed air parcels three days before observation. We see that the air masses "away from the jet" (black) came from lower latitudes and did not travel as far around the pole. The air found near the jet (red) has stayed near the jet for the last 3 days at least. The air parcels measured on 7 October as a rather compact group were stretched through a long portion of polar jet on the other side of the pole just 3 days ago. These air masses were brought together by strong wind shear and transported far away by the strong westerlies of the jet. Note as well that the original positions of "near jet" air look especially dispersed around a breaking Rossby wave at 140° W. Such a sparse group of air parcels could only be brought into a compact group by strong wind shear and stirring in the breaking RW. This difference in air mass origin explains, why most of the filamentation in trace gas structure can be seen between 15:10 and 19:10 UTC ("near jet" air). The origins of air inside the hexagonal flight pattern will be studied in more detail in Section 4.2.2.

To highlight the effect of RW breaking, we provide separate O_3 – H_2O tracer-tracer plots for "near jet" air masses (Figure 4.4a) and the rest (Figure 4.4b). We designate air parcels as stratospheric, if they contain less than 10 ppm water vapour, and tropospheric, if they have less than 0.1 ppm ozone. In this context, such air parcels are often refereed to as stratospheric and tropospheric *end members*. Air parcels that fall into neither of these two categories are typically products of mixing (Proffitt et al., 1990; Hoor et al., 2002; Pan et al., 2004). In the eastern part of the flight there is evidence of some mixing, but only between end members with relatively low values of both ozone and water vapour. This indicates that stratospheric air masses do not penetrate far into the troposphere and vice versa. Since in situ observations represent a more spatially limited data set (black dots), two separate mixing lines can be discerned there. The "western" part of the flight, close to the polar jet, shows evidence of more vigorous mixing. In particular, there is a distinct branch of wet ($>$ 50 ppmv water) air with potential temperatures consistent with the upper troposphere in this region and enhanced ozone (around 0.15 ppmv). This suggests an influx of stratospheric air into the

upper troposphere. Also, the air mass with around 0.2 ppmv O_3 and 30 ppmv H_2O could only have originated from a substantially deeper tropospheric intrusion into the stratosphere (or vice versa) than that needed to explain the ozone-water vapour structure of the eastern part of the flight.

4.2.2 Tomography results and analysis

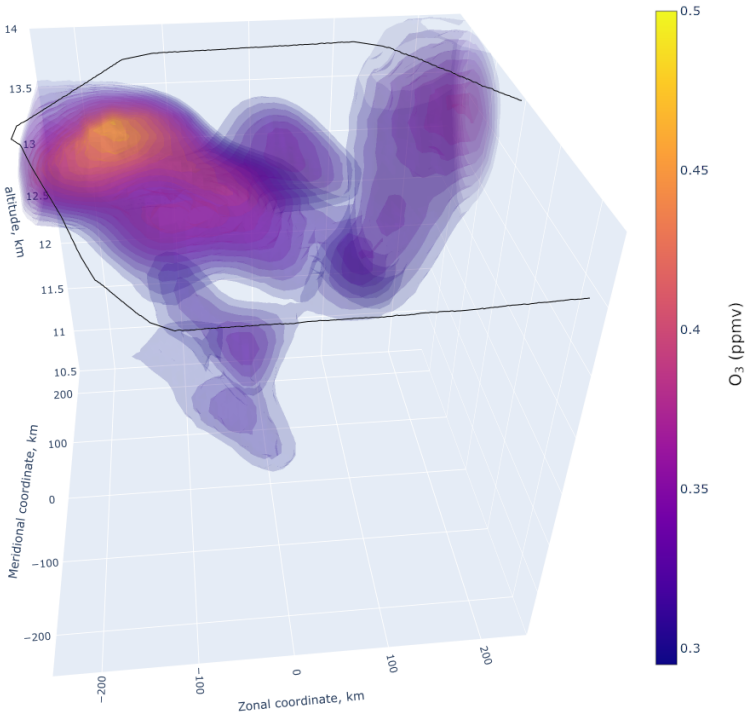

Figure 4.5: 3-D plot of tomographic retrieval of ozone VMR. Flight track represented by a thin black line.

In this section we study the origin of the air inside the hexagonal tomographic flight pattern on 7 October (see Figure 4.1a). The results of the tomographic retrieval for ozone and nitric acid (HNO_3) are presented as vertical 2-D cuts through the measured volume in Figure 4.6. There is, as before, a clear positive correlation between the two trace gases. A more detailed look into the correlation of the two gases is presented in Section 4.2.3.

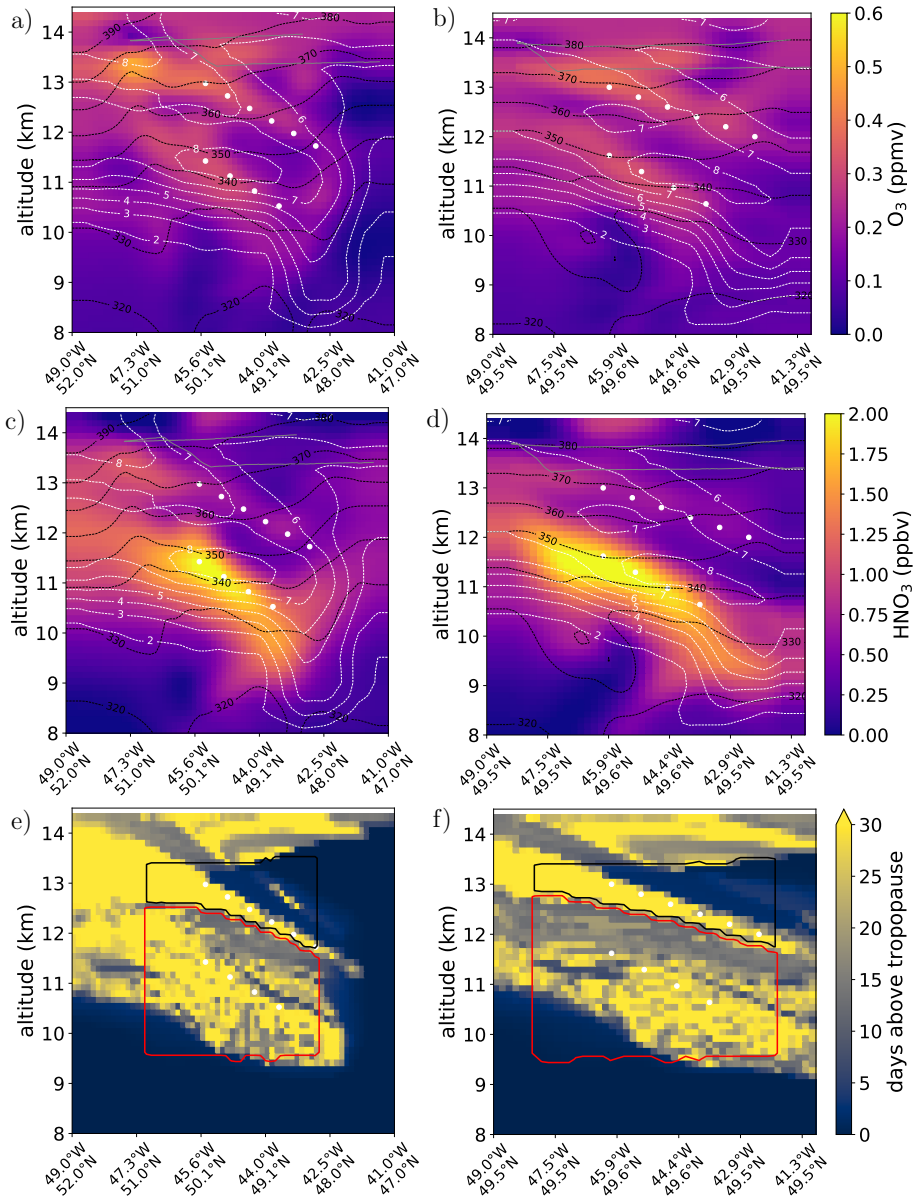

Figure 4.6: Vertical cuts through 3-D tomographic retrieval and corresponding air mass origin plots. Solid grey line – projection of flight path onto the displayed cut, black dashed lines – isentropes, labelled in K, white dashed lines – PV isosurfaces, labelled in PVU. Black and red lines in the bottom panels show the position of air parcels for which backward trajectories were calculated. Their previous positions shown, with those same colours, in Figure 4.8. Positions of vertical cuts are shown in Figure 4.1a: left panels - magenta, right panels - cyan. White dots mark filaments (see main text).

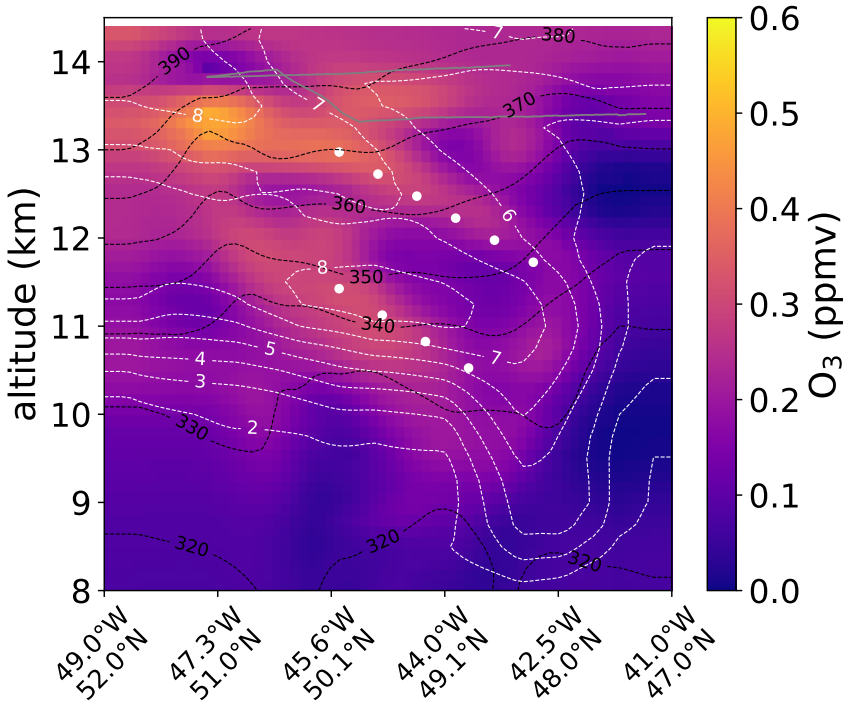

Figure 4.7: A vertical cut through 3-D tomographic retrieval (Figure 4.6 a enlarged). Solid grey line – projection of flight path onto the displayed cut, black dashed lines – isentropes, labelled in K, white dashed lines – PV isosurfaces, labelled in PVU. The position of the cut is shown as a solid magenta line in Figure 4.1a

Figure 4.6 also shows a complex structure of thin filaments (layers) of younger and older air in the lower stratosphere (LS). As in the previous section, we use backward trajectories to determine the "age" (time spent above dynamical tropopause) of each stratospheric air parcel observed by GLORIA (Figure 4.6e, f). The two older air filaments (marked with white dots) that are the main features of both ozone and nitric acid retrievals can be identified with the two filaments of air that has stayed in the stratosphere for more than 30 days. Younger air masses can be seen in between the two filaments as well as above them. The boundary between older stratospheric air and the troposphere at 10-11 km altitudes is also reflected in the retrieval. For ozone, in particular, values higher than approximately 0.25 ppbv within the hexagonal flight pattern are mostly measured for air parcels that stayed in the stratosphere

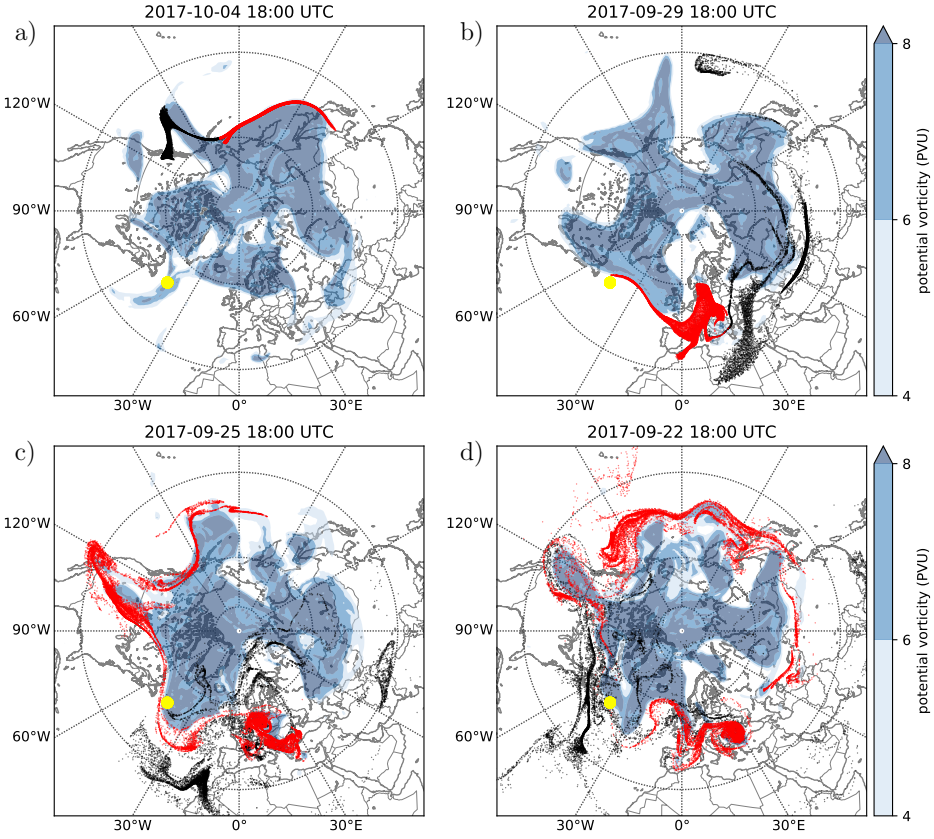

Figure 4.8: Origins of observed air parcels. Panels show horizontal cuts at 11 km altitude. Potential vorticity is shown in shades of blue. The location where air parcels were observed by means of GLORIA 3-D tomography on 7 October is shown in yellow (they form a small disc). The parcel locations at the dates indicated for each panel are shown in black and red. We further distinguish those into: red - those that were east of 165°W on 4 October 18:00 UTC, black – the remaining ones.

for more than 30 days. The accuracy and resolution of the retrieval decreases away from the centre of the hexagonal flight pattern, which is the likely reason for the "smearing out" of the filaments at around 48°N, 42.5°W.

The panels of Figure 4.6 with GLORIA data also show potential temperature isolines, derived from GLORIA temperature retrieval and ECMWF pressure data. The major filaments

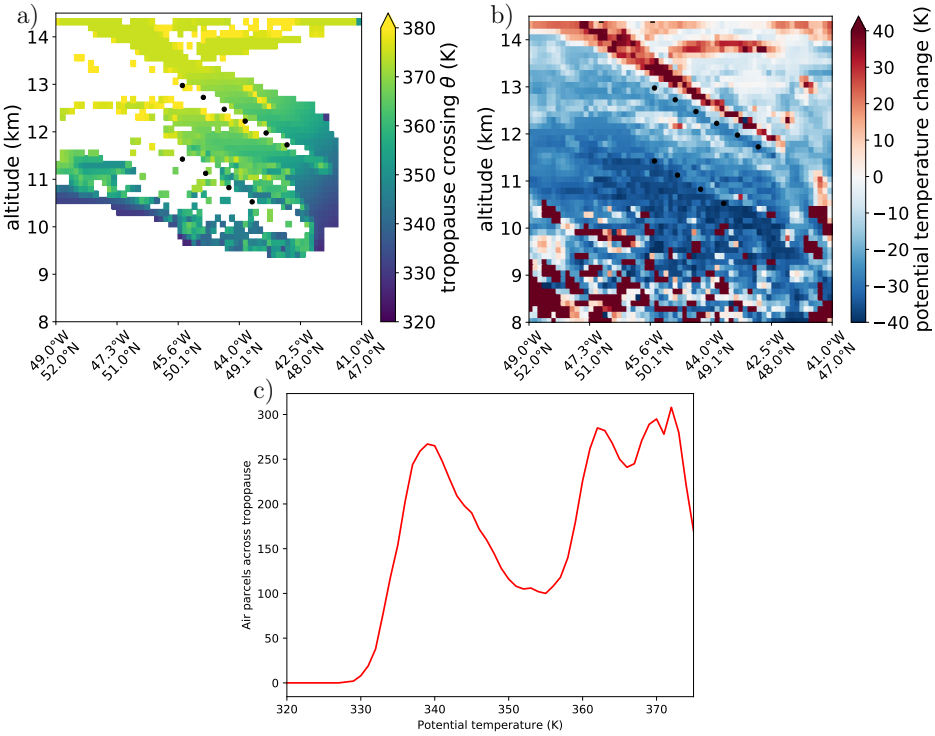

Figure 4.9: Panel a) shows the potential temperature of tropopause crossing for the parcels that crossed tropopause within the last month. Panel b) shows the change in potential temperature of observed air parcels within the last month. Black circles in panels a) and b) mark retrieved old air filaments, they are at the same positions as the white circles in Figure 4.6. Panel c) shows the distribution of potential temperature of tropopause crossing for the observed air parcels (5 K running mean).

are almost uniform in nitric acid and especially ozone structure, despite the fact that they are not isentropic. The arrangement of tracer filaments and potential vorticity with respect to potential temperature surfaces shows that scale breakdown has occurred: although the filaments remain quasi-horizontal, they can subsequently be erased by mixing along isentropes, making the effective horizontal length scales shorter.

A more detailed look into the backward trajectories allows us to trace the origin of each major filament and explain most of the observed ozone structure in terms of planetary wave activity. Figure 4.8a shows that air masses sampled by the 3-D retrieval on 7 October (location

highlighted in yellow) come from an elongated region along the polar jet (edge of high PV region). This is because the retrieval sampled air masses right on top of the jet at different altitudes. Air parcels in the jet tend to stay confined to it, but are subject to extreme vertical wind shear: in the observed altitude range the wind speed of the jet decreases rapidly with altitude, thus air masses from low altitudes have travelled a longer distance around the pole. This can be confirmed in Figure 4.6e-f: the "red" air parcels of Figure 4.8, where observed below the "black" ones. A breaking Rossby wave can be seen around 140°W on 4 October. The "black" group of air parcels were brought together by this breaking event: one can already see them as a relatively compact group on 4 October, but the panel from 29 September shows that they in fact come from very different locations west of the breaking wave. The old and young air structures seen in the "black" areas in Figure 4.6e-f are hence a consequence of this event: the young air masses (they are roughly 3 days old, as the event happened 3 days ago) entered the stratosphere because of the event, and older air masses were completely reshaped. In a similar fashion, another Rossby wave breaking event around 8 days prior to measurement (29 September) created the other prominent young air filament (seen at the top of the region marked by red contours in Figure 4.6)e-f, with most of the air entering from the troposphere over western Europe. Most of the remaining air masses observed by GLORIA below 12 km can be traced back to a third wave breaking event on 25 September (Figure 4.8c). One can then see that the RW breaking is the dominant process for tracer structure genesis in this region, with most of the old versus young air structure formed by it.

Figure 4.9 gives some insight into the vertical transport of observed air parcels. Panel c) shows the distribution of the observed air parcels according to the potential temperature at which they entered stratosphere (maximum potential vorticity gradient tropopause was used to determine the entry point). It shows the two distinct pathways of air into stratosphere around the polar jet: from low potential temperature levels (∼340 K or less) upwards across the tropopause, or isentropically from lower latitudes at high potential temperature (horizontal transport). The latter pathway plays a major role, as expected for this region (Holton et al., 1995; Pan et al., 2009). Figure 4.9b shows the origin of air parcels in the vertical direction. We can distinguish between the two old air filaments that have descended from the stratosphere

(black circles) that match the retrieved old air structures, the air in between and to the south east of the filaments, that has been isentropically transported into the stratosphere and has less stratospheric tracers, and the turbulent troposphere below ∼9.5km with low ozone and nitric acid values. The young air filament just above the upper filament marked in circles has been strongly displaced upwards during a Rossby wave breaking event. Its signature can be seen in Figure 4.6a between the upper old air filament marked with white circles and a small old air blob at 43.5°W at around 13km altitude.

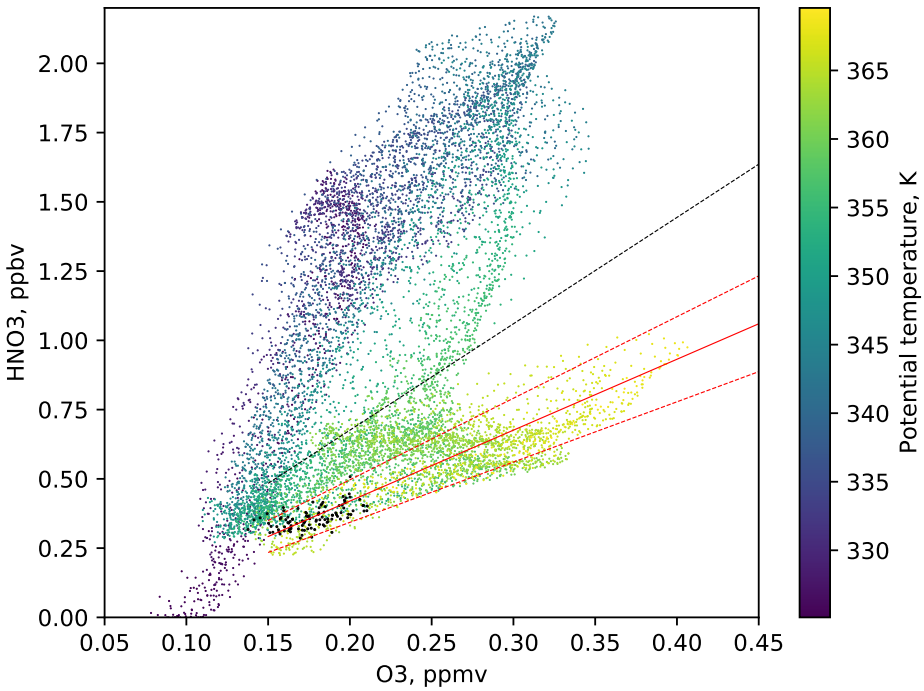

Figure 4.10: Ozone - nitric acid tracer-tracer plot. Solid red line represents linear relationship of ozone and nitric acid typical for the stratosphere. Dashed red lines indicate the ±15% HNO_3 compared to that relationship, black dashed line indicates +50% HNO_3. Black dots represent in situ measurement data, dots of the shown colour scale – GLORIA data. Maximum potential vorticity gradient tropopause was used here.

4.2.3 Ozone and nitric acid concentration comparison

Nitric acid (HNO_3) is produced in the stratosphere (mainly from NO_x) and destroyed in the troposphere by washout. Hence tropospheric HNO_3 mixing ratios can be as low as 0.1 ppbv or less. Due to similar source and sink regions, HNO_3 typically displays very compact relationship with ozone in the stratosphere. Popp et al. (2009) gives a simple linear relation between the two gases, which typically holds within 15% in the stratosphere for ozone concentrations higher that 150 ppbv

$$HNO_3 = (0.00256 \pm 0.000154)O_3 - (0.0922 \pm 0.0886)\text{ppbv} \tag{4.1}$$

The tracer-tracer correlation of ozone and nitric acid for the 3-D tomographic retrieval is shown in Figure 4.10. We can distinguish between several types of air masses in this tracer-tracer space. There is a HNO_3 poor tropospheric branch ($HNO_3 < 0.2$ ppbv), which consists solely of air parcels located below the dynamical tropopause (around 330 K here). A "deep stratospheric" branch conforms to the relationship of (4.1) within the prescribed $\pm 15\%$ tolerance and consists mainly of air parcels above 360 K potential temperature. Air along the flight path falls into this category based on both GLORIA and *in situ* measurement data. Most of observed stratospheric air parcels have slightly enhanced HNO_3 values (between +15% and +50% HNO_3 compared to (4.1)). Finally, there is the air mass with strongly enhanced HNO_3 values around the tropopause, clearly seen in Figure 4.6. It has > 1.25 ppbv HNO_3 and potential temperature of 330-350 K. Evidence of mixing between this air mass and its surroundings can be seen as linear structures in Figure 4.10.

It is clear from the argument above that the strong HNO_3 enhancement seen in Figure 4.6b-c at the altitude of around 11.5 km could not be a consequence of STE alone. The most important tropospheric source of HNO_3 is conversion from NO_x, which, in turn, is produced mostly by fossil fuel burning (24 TgN/yr), biomass burning (8 TgN/yr), soil emissions (12 TgN/yr) and lightning ((9 TgN/yr)) (Price et al., 1997; Nesbitt et al., 2000). All of these sources, except for lightning, release NO_x into the boundary layer, where its lifetime often below 1 day (Tie et al., 2001) and any HNO_3 produced is subject to washout. Therefore,

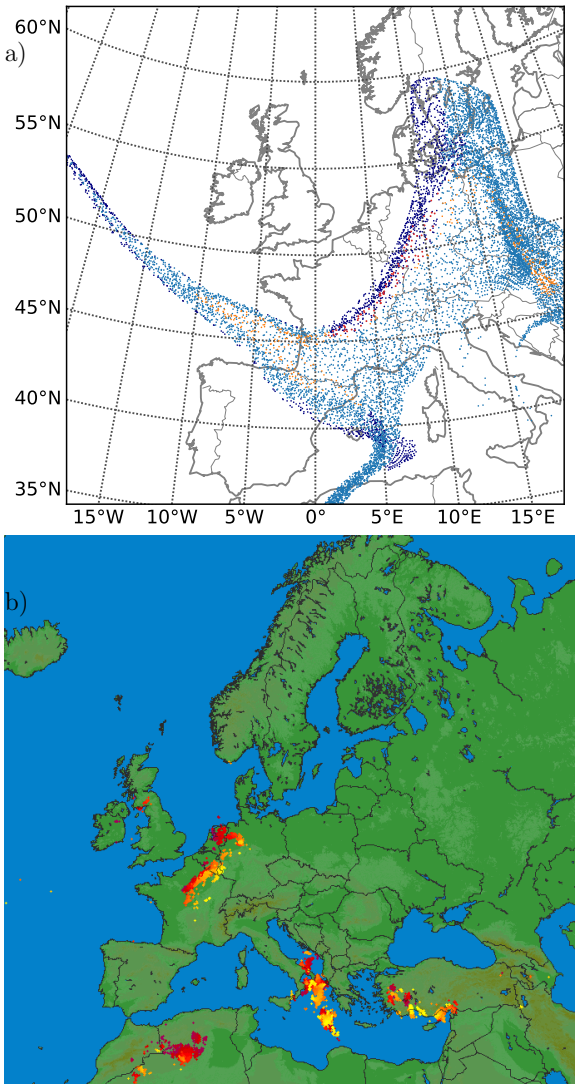

Figure 4.11: Panel a) shows the positions of air parcels observed as part of the 7 October 3-D retrieval on 29 September 18:00 UTC (8 days before measurement). Air parcel colouring: dark blue – less than 2 ppbv HNO_3, less than 5 PVU; light blue – less than 2 ppbv HNO_3, more than 5 PVU; red – more than 2 ppbv HNO_3, less than 5 PVU; orange – more than 2 ppbv HNO_3, more than 5 PVU. HNO_3 VMRs considered are from the 7 October 3-D retrieval. Panel b) shows lightning strikes between 29 September 18:00 UTC and 30 September 00:00 UTC in the area, based on VLF network data. Lightning strikes are indicated by purple-to-yellow colour scale, depending on their time of occurrence within the given period.

despite lower total emissions, lightning is the most important source of NO_x in the upper troposphere (Zhang et al., 2000, 2003).

Backward trajectories were used to investigate whether the air masses with enhanced HNO_3 values could have been influenced by lightning. The air parcels observed on 7 October only came into proximity of significant lightning activity around 8 days before the measurement. That was also the time when the structures around the enhanced HNO_3 air masses there formed, i.e., it is the earliest time when the measured air parcels formed a relatively compact group (Figure 4.8). Figure 4.11 shows the positions of the air parcels with more than 2 ppbv HNO_3 and other air parcels observed by GLORIA on 29 October and the map of lightning activity that day. We see that the air mass in close proximity to the lightning strikes (both close by horizontally and located below 5 PVU) has a large proportion of HNO_3 rich air parcels, and, conversely, that significant proportion of HNO_3 rich air is located close to the lightning activity. Also, the time of 8 days between NO_x emission and HNO_3 measurement would have been sufficient for NO_x to HNO_3 conversion based on, e.g., Jaeglé et al. (1998). It is therefore possible, that the highest HNO_3 values observed on 7 October were due to lightning. The lightning positions were obtained from very low frequency (VLF) radio observations (lightningmaps.org, Narita et al. (2018)).

4.2.4 October 9 measurements: late stage of RW breaking

The breaking Rossby wave event seen on 7 October was observed again during a flight on 9 October. No measurements suitable for tomography were taken during this flight and the 2-D data for O_3, HNO_3 and H_2O are shown in Figure 4.12. ECMWF forecasts before the flight led us to expect that the breaking wave would be squeezed into a thin filament, shown as 2 PVU contour in Figure 4.1b extending from 70°N, 0°E to 51°N, 12°E (dashed magenta line). The filament was crossed twice in both directions and can indeed be seen as ozone and nitric acid rich structures around 11:00 and 14:00 UTC. Using backward trajectories the air parcels that were measured both as part of the tomographic 3-D retrieval on 7 October and 2-D retrieval on 9 October were identified. They are highlighted by horizontal green hatches in Figure 4.12.

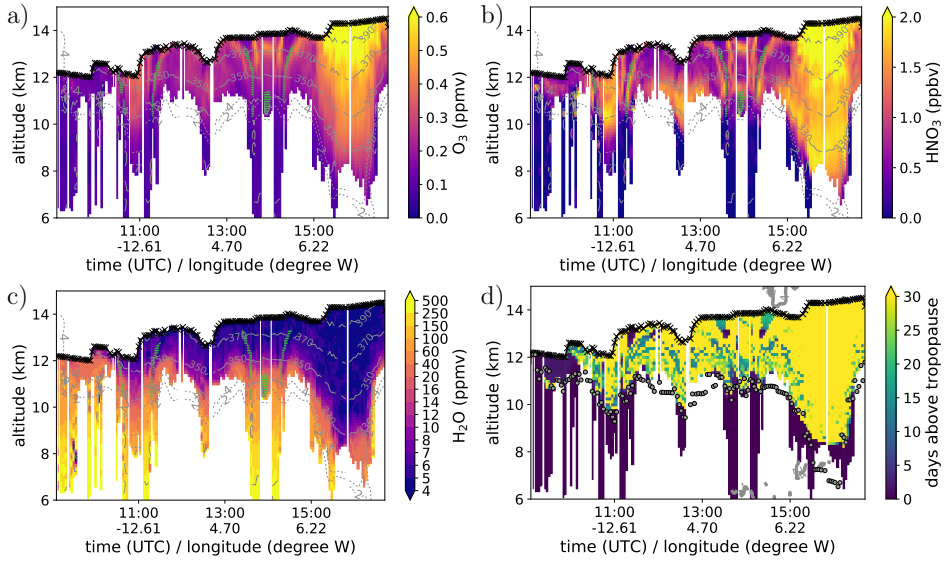

Figure 4.12: 2-D data from 9 October flight. Ozone (top left), nitric acid (top right), water vapour (bottom left) retrievals with age of air plot (bottom right) for the same air parcels. Isentropes are shown as thin solid lines, 2 and 4 PVU contours – thick dashed lines. Green hatches represent air parcels observed by GLORIA on 7 October.

The old air (ozone and nitric acid rich) parts of the filament are very thin (some only around 35 km thick). The air mass that filled the hexagon (400 km in diameter) on 7 October was also stretched into a filament of 30 km thickness in its narrowest parts.

As before, a plot showing the age of air in the stratosphere is provided in Figure 4.12d. Note the qualitatively different nature of younger air structures compared to previous plots of this sort and lack of filamentation in this region, which is generally less affected by planetary waves. The only sizeable young air parcels are found around the breaking Rossby wave. A O_3 - HNO_3 tracer - tracer plot for the air parcels observed in both flights is shown in Figure 4.14. The general positive correlation between O_3 and HNO_3 and the enhanced HNO_3 values remain in the retrieval of 9 October, but the maximum concentrations of both tracers are slightly lower. There are more air samples of middling tracer values (e.g., around 0.17 ppmv of ozone and 0.65 ppbv of nitric acid), while the distinct outlying branches, such as the purely stratospheric branch (around solid red line) and the highest HNO_3 enhancement, are noticeably subdued.

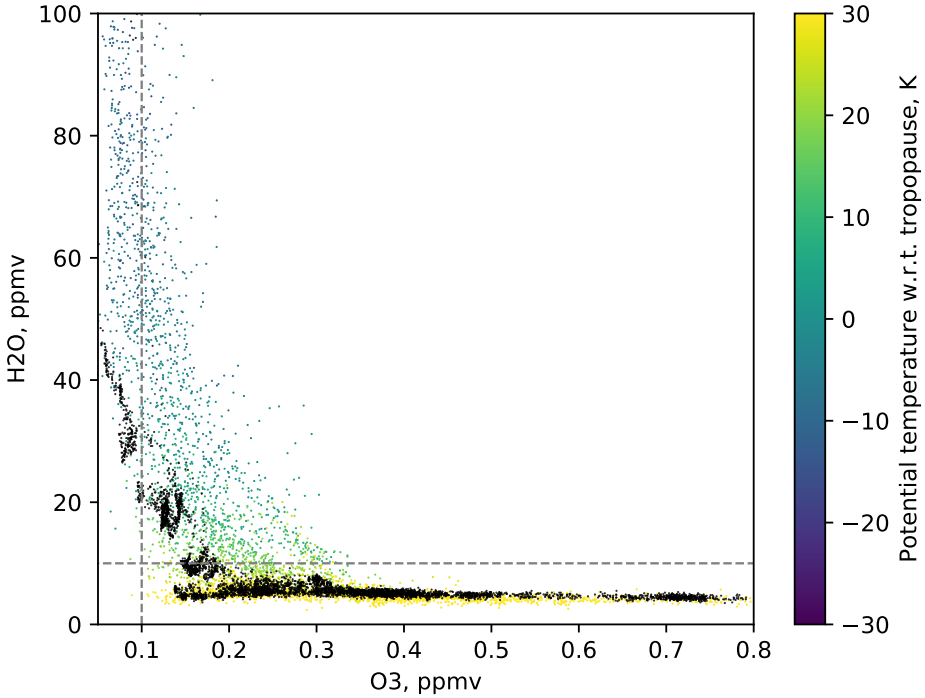

Figure 4.13: Ozone - water vapour tracer-tracer plot from October 9 flight. Black dots represent in situ measurement data (O_3 – FAIRO, H_2O – FISH), dots of the shown colour scale – GLORIA data. Maximum potential vorticity gradient tropopause was used here.

This is evidence of mixing, as tracer concentrations in all samples approach their average values.

The O_3 – H_2O correlation (Figure 4.13) has a similar dual mixing line structure as the corresponding correlation for "near jet" air parcels of the 7 October flight (Figure 4.4a). This is not surprising, since many of the air masses observed during the 9 October flight come from the area observed on 7 October. The later flight, however, encountered some very ozone-rich (∼0.8 ppmv) air masses around flight level, and generally slightly enhanced ozone values in the troposphere. The latter fact might be a consequence of further advanced mixing around the tropopause.

To further investigate the evolution of the air parcels observed in both flights, we determined the HNO_3 values in the hexagon based on the 9 October retrieval performed 2 days

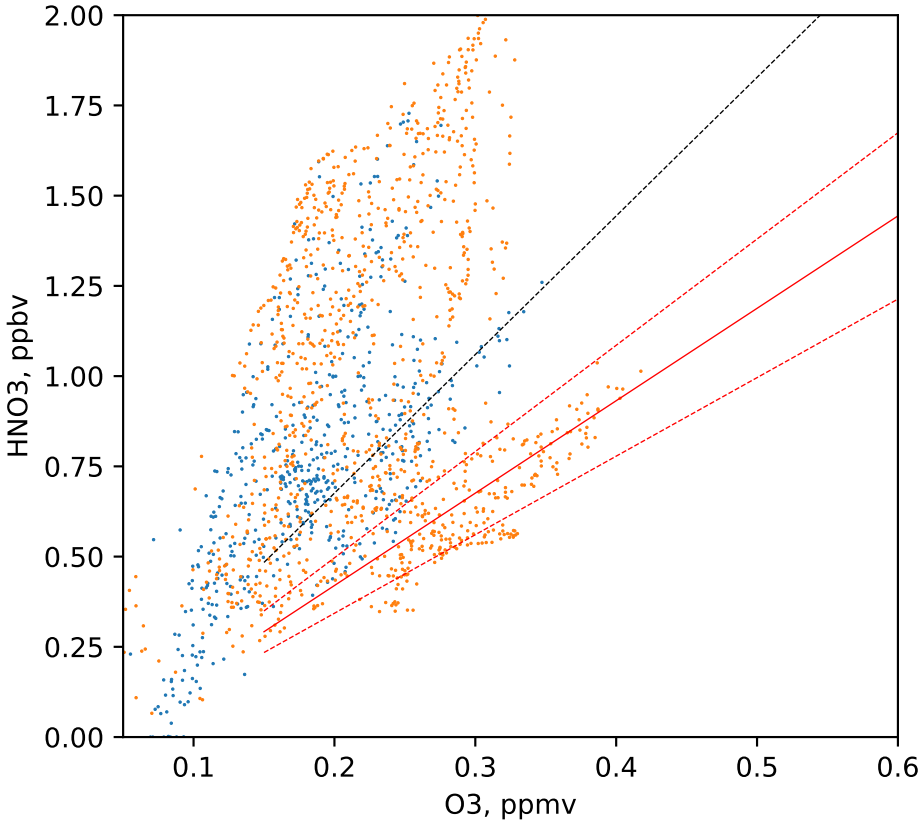

Figure 4.14: Ozone – nitric acid tracer-tracer plot for air parcels observed in both flights. Tracer concentrations measured on 7 October (3-D tomographic retrieval) shown in orange, those measured on 9 October – in blue. Solid red line represents linear relationship of ozone and nitric acid typical for the stratosphere. Dashed red lines indicate the ±15% HNO_3 compared to that relationship, black dashed line indicates +50% HNO_3.

later. Air parcels from the 9 October 2-D data product were traced back to the hexagon. Each grid point inside the hexagon was assigned the HNO_3 volume mixing ratio of the closest back traced parcel. If no parcel was traced back to a particular point within 100 km horizontally or 0.4 km vertically, the HNO_3 volume mixing ratio was deemed undetermined. One vertical cut through the HNO_3 "retrieval" obtained in this manner is shown in Figure 4.15, with a cut through the actual 3-D retrieval from 7 October shown for comparison. We can see that the tracer structure obtained by back tracing reflects many of the features in the tomographic

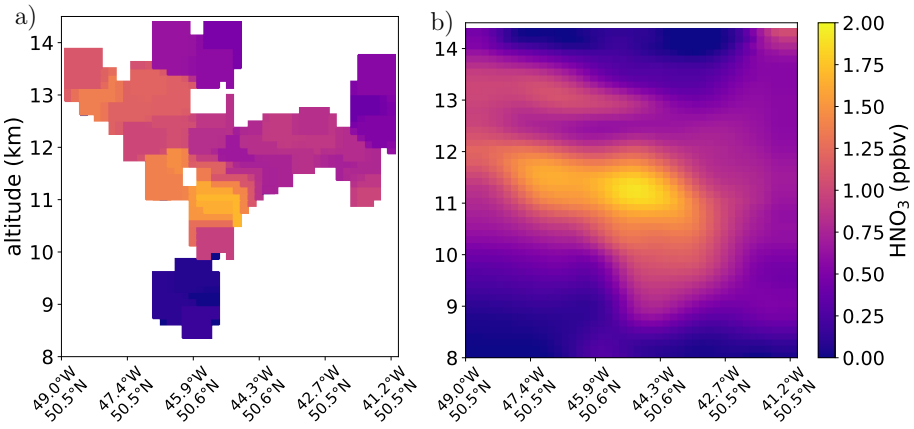

Figure 4.15: Left panel - HNO_3 volume mixing ratios on a vertical cut inside the hexagonal flight pattern based on back traced 9 October measurements, right panel – HNO_3 volume mixing ratios from the 7 October tomographic 3-D retrieval on the same vertical cut for comparison.

retrieval, although they are less intense and resolution, obviously, is a lot lower. This comparison demonstrates, however, that the thin filament, although clearly irreversibly separated from air masses around polar jet, is still not mixed and "remembers" its past.

4.3 Accuracy and validation

4.3.1 Tomographic retrieval error estimation

The data quality and expected errors of tomographic retrieval differ depending on the position of the point where these errors are calculated with respect to the flight path (hexagonal part of pattern). The relative errors for HNO_3 and O_3 were estimated for each point on the retrieval grid using a Monte Carlo based technique (Section 2.4.2). The particular error estimate calculated here includes measurement error and errors due to inaccuracies of the retrieval method, but does not include errors due to imprecise knowledge of atmospheric parameters (e.g. pressure, CO_2 volume mixing ratios, etc.), that are required for retrieval and taken from external sources, mostly models.

Results of the calculation are presented as a vertical cut through the retrieved 3-D volume

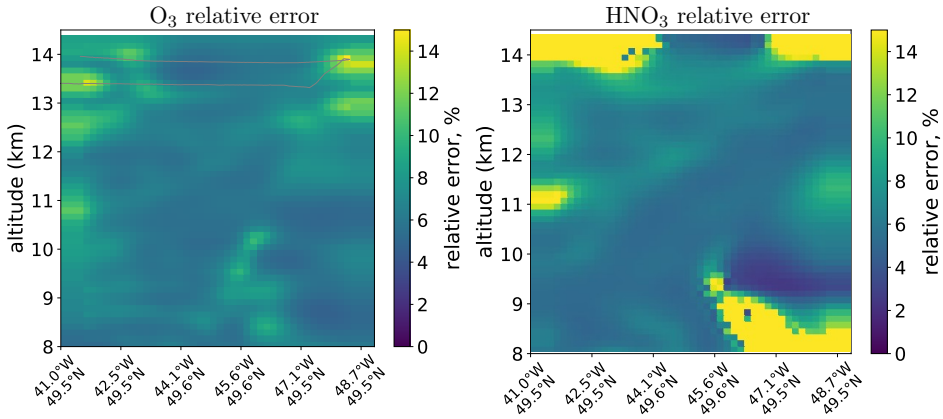

Figure 4.16: 3-D tomography relative error, Monte Carlo estimate

Table 4.3: Average measurement error for 11 to 12 km altitude

Retrieval	O_3 ppmv	HNO_3 ppbv
7 October, 3-D	0.014	0.06
7 October, 2-D	0.006	0.03
9 October, 2-D	0.008	0.04

(Figure 4.16). The same cut as in Figure 4.6, left, was used. One can confirm that, as expected, the data quality is best under the centre of the hexagonal flight pattern and quickly gets worse just outside the hexagon. Ozone retrieval around the flight path itself also seems problematic and should be interpreted with care. The average error values for measurements at 11 to 12 km altitude with horizontal distance of up to 200 km from the centre of the hexagonal flight pattern are given in Table 4.3. The table also contains estimates for linear retrievals at the same altitude range, using the methodology of Section 2.4.1.

4.3.2 3-D retrieval validation using in situ instrument data

In order to validate the 3-D data products, we have performed a comparison with *in situ* measurements. During WISE ozone volume mixing ratios were measured by the Fast Airborne Ozone instrument (FAIRO) (Zahn et al., 2012). The Atmospheric Nitrogen Oxides Measuring System (AENEAS) was also on board and provided NO_y and NO data products. In UTLS one can generally calculate the total reactive nitrogen as the sum of volume mixing ratios of

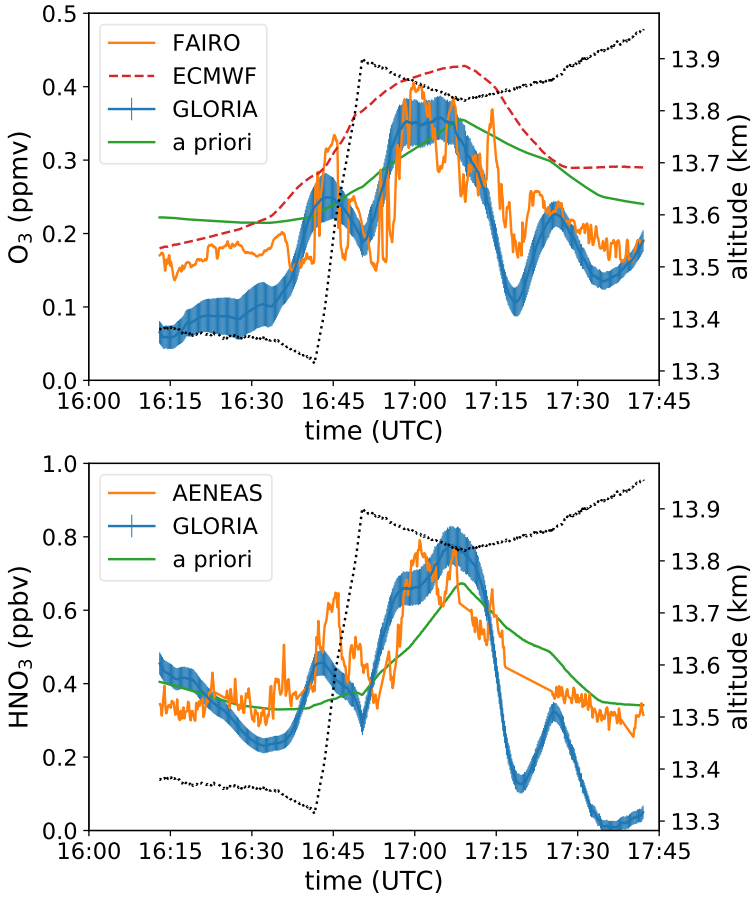

Figure 4.17: Comparison to in situ instrument data along the flight path. *A priori* data is from the WACCM model. Refer to main text regarding details on *in situ* instruments and there data products.

the following gases

$$NO_y \approx NO + NO_2 + HNO_3 + PAN + ClONO_2 \tag{4.2}$$

The volume mixing rations of NO_2, PAN and $ClONO_2$ are all typically at least one order of magnitude lower than that of HNO_3 considering the latitude and season of observation. PAN, and $ClONO_2$ can be obtained be GLORIA data, and NO_2 is a relatively well mixed

tracer which we estimated based on WACCM model data. HNO_3 can hence be derived from AENEAS data for GLORIA validation purposes.

The comparison of GLORIA data and the *in situ* instruments is presented in Figure 4.17. There are two important considerations that have a significant effect on how good of a match to *in situ* can be expected. Firstly, GLORIA measures trace gas volume mixing ratios along its line of sight, with a vertical resolution of about 200 m, and horizontal resolution of 20 km. Since the whole line of sight (for usable measurements) is actually below the flight altitude, the highest altitude data available cannot be regarded as measured from the aircraft location, but rather $\sim$ 100 m below it and $\sim$ 10 km to the side of it. The result is imperfect spatial coincidence between GLORIA and *in situ*, which can introduce biases into the comparison in the areas of high tracer gradients. Secondly, the GLORIA data product is valid for 16:50 UTC, while the *in situ* data is valid for the measurement time (see advection compensation description in Section 4.1.2). The data in Figure 4.17 is corrected for this discrepancy in the sense that GLORIA data is provided for the actual air masses that the aircraft was flying through and not for the locations with respect to ground that were sampled. By 16:50 UTC, however, many of these air masses, especially the ones from the beginning of the flight, were advected outside of the best resolved area of the hexagonal flight path (i.e. there were few overlapping measurements of these air parcels). This has a negative effect on data quality there. The errors for air further below flight altitude and closer to the centre of the hexagon should therefore be more accurate.

4.4 The effect of advection compensation

The 3-D tomographic retrieval was performed in the vicinity of the polar jet: the winds in parts of the observed volume exceed 40 m/s. HALO aircraft took around 1 h 45 min to complete the hexagonal flight pattern and some locations in the atmosphere were observed from one direction in the beginning of this period, and then again from another angle near the end of it. Due to the high winds, such a pair of measurements did actually look at different air masses and could significantly disagree. This problem is solved by introducing advection

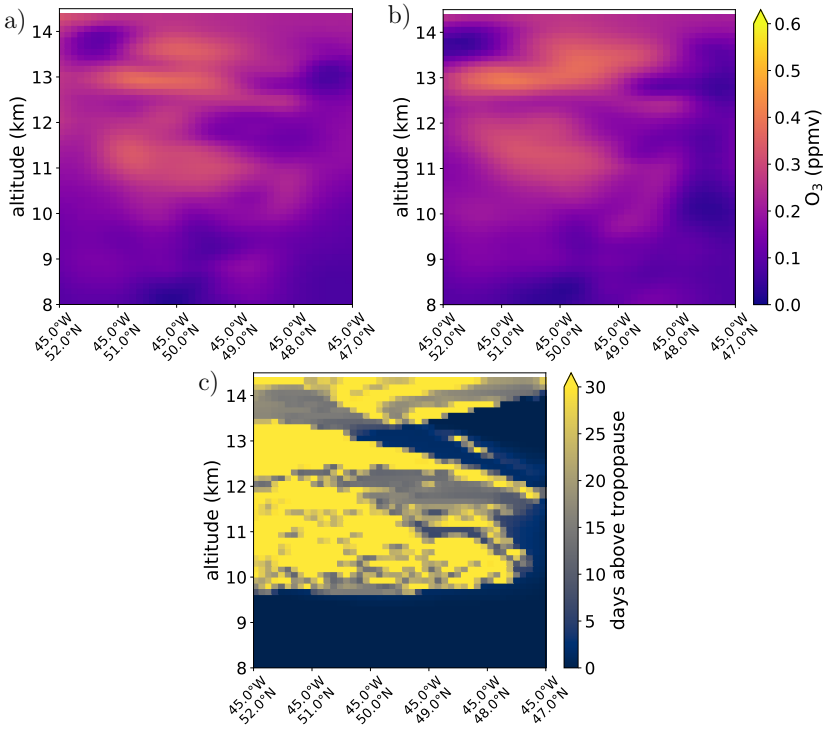

Figure 4.18: The effect of advection compensation. All three panels show the same cut through retrieved volume: a) with advection compensation, b) without. Panel c) shows age of air, defined as before.

compensation (Ungermann et al., 2011). The main idea of the technique is described below.

We choose a time t_v for which the retrieval will be valid (16:50 UTC in this case, approximately the middle of the measurement time window). As it is the case with most instruments, GLORIA retrieval data is provided on a discrete grid. If a measurement was taken at a time t_m, one can relate all required atmospheric parameters at each grid point at time t_m to the actual retrieved quantities (atmospheric parameters at time t_v) by advecting grid points at time t_m to time t_v. In practice, this advection is not performed for every t_m, but only to a number of preset values and then temporal interpolation is used. In this work CLaMS backward trajectories, driven by ECMWF winds, were used for advection. The positions of advected grid points were recorded with 10 min intervals. The additional computational costs

due to advection compensation amount to less that 10% of the total computational cost of the 3-D retrieval.

The success of this approach depends on the key assumption that the mixing and chemical state of an air parcel remain constant within the time of tomography acquisition. This is true to high accuracy for the VMRs of most trace gases, since most processes of atmospheric chemistry are too slow to meaningfully change air composition within the time period of less than 2 h: trace gasses are simply advected by winds. Temperature retrievals are rather more complicated in this regard: temperature might change due to adiabatic expansion or contraction as the air parcel moves, it can have significant small scale disturbances due to internal gravity waves. For the work described in this chapter, advection compensation was used for trace gases, but no compensation at all was applied for temperature. This still delivered good results, since the temperature distribution in our particular case lacked small scale structure, diminishing the acquisition time problems for temperature. Also, we were mostly interested in retrieving trace gases, temperature data product, by itself, is of lesser scientific interest and is only required to be able to retrieve trace gases properly. Small inaccuracies in temperature are therefore less of the problem. The effect of temperature error on trace gas products is included into the error estimates (Section 4.3.1). One cannot, however, do the same for temperature-focussed retrievals (e.g. internal gravity wave observations). A simplified physical model of gravity waves that could be incorporated into the inverse modelling scheme and account for temperature evolution is subject to further work.

Although the advection compensation was proposed by Ungermann et al. (2011), it was not applied for production retrievals till now, mostly due to the lack of research flights in windy conditions with specialised patterns for tomography and a focus on trace gas retrievals. It is therefore interesting to confirm that advection compensation does lead to improved results. Figure 4.18 shows a different cut through the 3-D volume than presented before, and showcases the differences between retrieval with advection compensation and one without. One can see that without advection compensation a prominent filament near the flight level becomes disconnected, among other differences. The retrieval with advection enabled is a better match to the age of air structure.

Chapter summary

A Rossby wave breaking event was observed with the GLORIA instrument during two research flights two days apart. Both, standard 1-D retrievals and 3-D tomographic retrieval of trace gas volume mixing ratios were performed. The latter was particularly challenging due to incomplete hexagonal flight pattern with a climb during its execution and high winds. Nevertheless, good data was obtained. Tomographic retrieval showed complex vertical structure in stratospheric tracers (ozone and nitric acid) with heavy filamentation, related to several previous Rossby wave breaking events. Many of those features cannot otherwise be observed in such detail. With the help of backward trajectory calculations, much the observed tracer structure can be understood as stirring and mixing of air masses of tropospheric and stratospheric origins (age-of-air concept), but there are still unexpected aspects to this structure, such as the non-isentropic nature of the filaments. Also, a strong nitric acid enhancement was observed just above the tropopause. It was demonstrated that lightning activity is a possible cause for this nitric acid enhancement. The backward trajectory analysis helped to identify air masses that entered stratosphere isentropically from lower latitudes and those uplifted upwards across tropopause, both types were identified with observed air with tropospheric signatures. The 2-D data showed signatures of enhanced mixing between stratospheric and tropospheric air parcels near the polar jet with some transport of water vapour into the stratosphere. In the late stage of the RW breaking event, a very thin filament (horizontal thickness was down to 30 km at some altitudes) containing air masses rich in stratospheric tracers was formed and advected away from the polar jet. The air masses of the filament showed signatures of mixing, but the tracer structure in the air volume observed two days earlier as part of the tomographic retrieval could still be traced back from the filament.

Chapter 5

Summary and outlook

In this thesis, novel methods for limb sounder 3-D tomographic retrievals were developed. They include a new regularisation scheme based on first order spatial derivatives and Laplacian and parametrised by physical parameters that can be obtained from in situ measurements or model data. The methods required to perform tomography on an irregular grid were developed as well, allowing for a reduction of total amount of points in the retrieval grid and saving computational costs. Finally, a Monte Carlo based method for computing retrieval diagnostics was adopted for the 3-D retrieval for the first time.

These methods were then applied to retrieving trace gas volume mixing ratios from two research flights of the GLORIA limb imager in order to study Rossby wave breaking. The resulting dataset is a unique combination of spatial coverage and resolution, and provides a unique glimpse on fine-scale vertical structures appearing as a result of stirring and filamentation.

The main questions to be tackled in this thesis were posed in the introduction and can now be answered:

- **What effect does the regularisation have on retrieval results? How can one ensure that this effect comes from physically meaningful assumptions, rather than ad-hoc mathematical manipulations?**

  A new regularisation scheme was introduced in this thesis. It is based on a simple covariance relation for the atmosphere (2.15) and physical parameters: the standard

deviation of the atmospheric quantity and its correlation lengths. They can be determined from model data and/or in situ measurements and theoretical considerations. The regularisation term (Section 2.2) corresponding to this covariance relation can be analytically expressed as volume integral involving gradients and the Laplacian of the atmospheric quantity. The volume integral can then be discretised for practical implementation. Tests with synthetic data showed that a 3-D tomographic retrieval with this new regularisation with parameters obtained from in situ measurements and general properties of the atmosphere (Section 3.2.2) was more accurate than the same retrieval with the more established Tikhonov regularisation parametrised by (unphysical) parameters hand-tuned specifically for the test case. This gives reason to believe that better data products could be produced with the new technique without many trial-and-error runs to determine the correct set of regularisation parameters. It is also noteworthy that good test results were achieved with constant regularisation parameters across the retrieval volume. The general framework developed here allows for spatial variability of those parameters for greater flexibility. This might be relevant for limb sounding from higher altitudes for which the range of retrieval altitudes is also high and properties of the atmosphere often vary.

- **Can the computational cost of tomographic retrieval be reduced by using irregular grids?**

  The retrieval implementation on an irregular grid was challenging. A conceptually rather complex algorithm to compute spatial derivatives on irregular grids (section 2.3.2) was required to prevent the appearance of additional retrieval noise, The final implementation produced virtually identical results to the previously used simpler rectilinear grid approach, but most grid points in poorly-resolved areas could be removed leading to a 82% reduction in grid size and a 50% reduction in overall computational cost. This was achieved on a relatively simple regular grid with axially symmetric density. Further reductions might be possible by aligning grid points closer with tangent point densities.

  The Monte Carlo technique for computing diagnostics previously could not be used for

3-D retrievals, as the 3-D covariance matrices, even if they are sparse, have too complex structure in general for the most commonly used root finding algorithms to work. These algorithms produce non-sparse roots and become numerically unstable in the process. A much more efficient matrix root finding algorithm was adopted (Section 2.4.2) and it is now possible to calculate diagnostics for all grid points with computational cost comparable to that of retrieval.

- **What is the 3-D distribution of air masses of stratospheric and tropospheric origin around the polar jet? How is it effected by Rossby wave breaking? Can this distribution be understood from the perspective of stratosphere-troposphere exchange (STE) and known dynamical processes?**

  The 3-D tomographic retrieval based on the data from the flight on 7 October 2017 revealed complex 3-D structure of air masses of the breaking wave. Two thin anisotropic filaments of old (rich in ozone and nitric acid) air were found stacked on top of each other with air of various ages around them (Section 4.2.2). CLaMS backward trajectory calculations showed that the two major filaments and air masses in between were indeed closely related to three previous Rossby wave breaking events. Age of air calculation based on the aforementioned backward trajectories and maximum potential vorticity gradient tropopause was used to demonstrate that much of the observed tracer structure could be understood as stirring and mixing of stratospheric and tropospheric air masses. There are, however, some unexpected aspects in the tracer structure, e.g. the non-isentropic nature of the observed filaments. Furthermore, a strong nitric acid enhancement just above the tropopause was observed. The ozone and nitric acid VMRs of this air mass could not be explained simply by descent from higher levels in the stratosphere. It was shown, however, that this enhancement had come into close proximity with thunderstorms and it was hence possible that it resulted from NO_x production by lightning (Zhang et al., 2000). The 3-D retrieval contained large amounts of air with history indicative of horizontal transport from lower latitude stratosphere and matching tracer signatures. Air masses from extratropical troposphere were found mostly at the

lowest altitudes of the observed part of the stratosphere, but strongly uplifted filaments were also present and their histories were consistent with the measured tracer content.

- **How strong are the mixing processes in the UTLS around polar jet? How are they influenced by Rossby wave breaking?**

  The atmospheric region near the jet stream showed heavy filamentation, vigorous mixing (diagnosed by means of ozone-water vapour tracer-tracer analysis) and some transport of water vapour into the stratosphere. Areas further away from wave surf showed pronouncedly weaker mixing signatures and much simpler structure of the lower stratosphere. During the late stage of the RW breaking event, an old air mass, some of which was observed as part of the discussed 3-D tomographic retrieval, was stretched into an very thin filament (down to 30 km horizontal width) and advected away from the jet. The air in the filament showed some signs of mixing with its immediate surroundings but still retained some of the structures of the previously observed air mass. The statistically meaningful match between the two retrievals was only possible due to the 3-D nature of the tomographic data product. The attempts to do the same with in situ instrumentation were not successful.

Outlook

At the time of writing, the novel 3-D tomography methods were already being applied for 3-D internal gravity wave retrievals of the recent SOUTHTRAC measurement campaign carried out in September-November 2019 in Argentina and Chile. Gravity waves manifest themselves as very complex (both in the vertical and horizontal directions) temperature structures, especially, if multiple wave packets are present at the observed location. The new regularisation is proving useful for capturing the fine detail of the waves. The savings in computational costs described in this thesis allow to perform these retrievals on a very fine grid with existing computer infrastructure, thus ensuring that no resolution is lost because of gridding. Unlike trace gas VMRs, temperature is not simply advected in the atmosphere. As a result, advection compensation discussed in this thesis cannot be directly applied to gravity wave retrievals.

An implementation of basic gravity wave physics directly into the inverse modelling scheme of GLORIA tomographic retrievals is planned in order to solve the finite acquisition time problem for gravity wave 3-D data.

More generally, the methods developed in this work can prove useful for any kind of remote sensing application that aims to deliver a 3-D data product. For example, observation geometries of many limb sounding satellites result in lines of sight that only intersect in the orbital plane (or parallel planes close to it), making it possible to perform tomography in two dimensions. If, however, the resulting data set is three-dimensional, it is inevitably correlated in all three dimensions and exploiting this fact with the help of a 3-D regularisation may significantly improve data quality.

The GLORIA data from the WISE campaign presents a unique combination of resolution and spatial coverage and could be very useful for model validation. So far, the data was analysed from the purely dynamical perspective using air parcel trajectory calculations. Comparing it with model runs including mixing and atmospheric chemistry implementations could answer many questions about model performance that are otherwise very hard to tackle.

Appendices

A.1 List of mathematical notation

General notation:

italic, e.g. F	Scalar variable (real number) or real-valued function.
bold italic, e.g. $\boldsymbol{a}$	Vector or vector-valued function.
bold roman, e.g. $\mathbf{G}$	Matrix.
$\{\mathbf{A}\}_{ij}$	Element of the matrix $\mathbf{A}$, i-th row, j-th column.
D$\boldsymbol{V}$	Jacobian of $\boldsymbol{V}$.
$\langle a \rangle$	Expected value of a.
$\langle \boldsymbol{a}, \boldsymbol{b} \rangle$	Inner product of $\boldsymbol{a}$ and $\boldsymbol{b}$.
$\|\boldsymbol{a}\|$	Norm of $\boldsymbol{a}$.
$\|\boldsymbol{a}\|_2$	Euclidean norm of a.
$\|\mathbf{A}\|_\infty$	The infinity norm (highest eigenvalue) of matrix $\mathbf{A}$.
$\sim$	Proportional to (when used in equations).

Particular notation:

$\boldsymbol{\epsilon}$	Vector of measurement error.
$\mathbf{I}$	Identity matrix.
$\boldsymbol{F}(\boldsymbol{x})$	The forward model (a mapping from atmospheric state space to measurements space).
$J(\boldsymbol{x})$	The cost function (sometimes called misfit), defined in equation (2.7).
$\mathbf{S}_{\text{apr}}$	Covariance matrix of of the atmospheric state.
$\mathbf{S}_{\text{apr}}^{-1}$	Precision matrix of of the atmospheric state.
$\mathbf{S}_{\epsilon}$	Covariance matrix of of the measurement error $\boldsymbol{\epsilon}$.
$\mathbf{S}_{\epsilon}^{-1}$	Precision matrix of of the measurement error $\boldsymbol{\epsilon}$.
$\boldsymbol{x}$	Atmospheric state vector.
$\boldsymbol{x}_{\text{apr}}$	A priori atmospheric state vector.
$\boldsymbol{y}$	Measurement vector.

A.2 List of abbreviations

CLAES	Cryogenic Limb Array Etalon Spectrometer
CRISTA	Cryogenic Infrared Spectrometers and Telescopes for the Atmosphere
CRISTA - NF	Cryogenic Infrared Spectrometers and Telescopes for the Atmosphere - New Frontiers
DLR	Deutches Zentrum für Luft und Raumfart, engl. German Aerospace Center
ECMWF	European Centre for Medium-Range Weather Forecast
GLORIA	Gimballed Limb Observer for Radiance Imaging of the Atmosphere
GW	Gravity wave
HALO	High Altitude and Long Range research aircraft
HIRLDS	High Resolution Dynamics Limb Sounder
IRLS	Infrared Limb Sounder
JURASSIC2	Juelich Rapid Spectral Simulation Code, version 2
LIMS	Limb Infrared Monitor of the Stratosphere
LOS	Line-of-sight
MIPAS	Michelson Interferometer for Passive Atmospheric Sounding
MIPAS - STR	Michelson Interferometer for Passive Atmospheric Sounding on Stratospheric Aircraft
MLS	Microwave Limb Sounder
NASA	National Aeronautics and Space Administration
POLSTRACC	Polar Stratosphere in Changing Climate measurement campaign
PVU	Potential vorticity unit, 1 PVU = 10^{-6} K $\cdot$ m^2 $\cdot$ kg^{-1} $\cdot$ s^{-1}
RW	Rossby wave

SAMS	Stratospheric and Mesospheric Sounder
UTC	Universal Time, Coordinated
UTLS	Upper Troposphere and Lower Stratosphere
VMR	Volume mixing ratio
WACCM	Whole Atmosphere Community Climate Model
WISE	Wave Driven Isentropic Exchange measurement campaign

A.3 Applicability of the new regularisation scheme for 1-D and 2-D retrievals

The exponential covariance relation, given in equation (2.15), can be trivially extended to any dimension. It is used as a statistical model to many processes. The norm associated with this exponential covariance, given in equation (2.16), is, however, a 3-D-specific result. Known 2D equivalents involve fractional powers of derivatives and therefore are not as easy to implement numerically. A norm associated with 1-D exponential covariance can be shown (Tarantola, 2013) to have the simple form

$$\|\phi\|^2 = \frac{1}{2\sigma^2 L}\left(\int_{x_1}^{x_2} \phi^2 \mathrm{d}x + L^2 \int_{x_1}^{x_2} \left(\frac{\partial \phi}{\partial x}\right)^2 \mathrm{d}x\right) \tag{A.3.1}$$

neglecting some boundary terms. Here the scalar field $\phi(x)$ represents the difference between the quantity to be retrieved and an a priori, and L is the correlation length. All the main theoretical results and numerical methods of this paper can therefore be reproduced for 1-D inverse modelling problems. The usefulness of our methods for practical 1-D applications ultimately depends on the size of the problem in question. 1-D limb sounding retrievals, for example, are usually too small for the methods developed here to be useful. It would typically be possible, and indeed simpler, to explicitly construct and invert the covariance matrix of a 1-D problem, rather than discretise the associated norm (A.3.1). In the case of a very large 1D problem with strong covariance, however, one may find the methods presented in this work more attractive.

Acknowledgements

I would like to address my first thanks to Prof. Dr. Martin Riese for giving me an opportunity to work at IEK-7 on this interesting research project and for entrusting me with the valuable experimental data used of this work. His comments on my results and publications were extremely helpful.

In particular, I would like to thank Dr. Jörn Ungermann for his patience in answering all my questions and providing a wider scientific context to many of the problems I faced. Countless discussions with him on almost every topic discussed in this thesis have greatly expanded my understanding both of remote sensing and atmospheric science. My work on tomographic retrievals is in many ways a continuation of the earlier work he did on this topic, and the measurement data presented in this thesis benefited greatly from his relentless efforts of improving GLORIA level 1 data processing and 1-D retrievals.

I am grateful to Dr. Peter Preusse for his continued support and ideas that helped me to improve my results and papers to be published.

I would also like to express my gratitude to the members of the GLORIA team for their impressive work on the instrument that made this research possible and for the friendly atmosphere that ensured the measurement campaigns were a truly unforgettable experience. I am also grateful to all the colleagues at IEK-7 for the very pleasant and stimulating working environment at the institute.

I would like to acknowledge HITEC (Helmholtz Interdisciplinary Doctoral Training in Energy and Climate Research) graduate school for providing funding for this PhD project.

Bibliography

E. Allen, J. Baglama, and S. Boyd. Numerical approximation of the product of the square root of a matrix with a vector. *Linear Algebra and its Applications*, 310(1-3):167–181, 2000. doi: 10.1016/s0024-3795(00)00068-9.

F. Aurenhammer, R. Klein, and D.-T. Lee. *Voronoi Diagrams and Delaunay Triangulations*. WORLD SCIENTIFIC, 2013. doi: 10.1142/8685.

J. T. Bacmeister, V. Küll, D. Offermann, M. Riese, and J. W. Elkins. Intercomparison of satellite and aircraft observations of ozone, CFC-11, and NO_y using trajectory mapping. *J. Geophys. Res.*, 104:16379–16390, 1999. doi: 10.1029/1999JD900173.

Y. Bai and D. Wang. On the comparison om trilinear, cubic spline, and fuzzy interpolation methods in the high-accuracy measurements. *IEEE Transactions on Fuzzy Systems*, 18(5): 1016–1022, Oct 2010. ISSN 1063-6706. doi: 10.1109/TFUZZ.2010.2064170.

J.-D. Boissonnat and M. Yvinec. *Algorithmic Geometry*. Cambridge University Press, New York, NY, USA, 1998. ISBN 0-521-56529-4.

M. Carlotti, B. M. Dinelli, P. Raspollini, and M. Ridolfi. Geo-fit approach to the analysis of limb-scanning satellite measurements. *Appl. Optics*, 40:1872–1885, 2001. doi: 10.1364/AO.40.001872.

J. G. Charney. Geostrophic turbulence. *J. Atmos. Sci.*, 28(6):1087–1095, 1971. doi: 10.1175/1520-0469(1971)028⟨1087:GT⟩2.0.CO;2.

A. R. Curtis. Discussion of 'A statistical model for water vapour absorption' by R. M. Goody. *Quart. J. Roy. Meteorol. Soc.*, 78:638–640, 1952.

D. P. Dee, S. M. Uppala, A. J. Simmons, P. Berrisford, P. Poli, S. Kobayashi, U. Andrae, M. A. Balmaseda, G. Balsamo, P. Bauer, P. Bechtold, A. C. M. Beljaars, L. van de Berg, J. Bidlot, N. Bormann, C. Delsol, R. Dragani, M. Fuentes, A. J. Geer, L. Haimberger, S. B. Healy, H. Hersbach, E. V. Hòlm, L. Isaksen, P. Kållberg, M. Köhler, M. Matricardi, A. P. McNally, B. M. Monge-Sanz, J.-J. Morcrette, B.-K. Park, C. Peubey, P. de Rosnay, C. Tavolato, J.-N. Thépaut, and F. Vitart. The ERA-interim reanalysis: configuration and performance of the data assimilation system. *Quart. J. Roy. Meteorol. Soc.*, 137(656): 553–597, 2011. ISSN 1477-870X. doi: 10.1002/qj.828.

B. Delaunay. Sur la sphere vide. *Bull. Acad. Sci. USSR: Class. Sci. Math.*, 7:793–800, 1934.

DLR. Halo website, 2020. URL `http://www.halo.dlr.de/aircraft/specifications.html`. Retrieved on 2020-06-20.

J. R. Drummond, J. T. Houghton, G. D. Peskett, C. D. Rodgers, M. J. Wale, J. Whitney, and E. J. Williamson. The stratospheric and mesospheric sounder on Nimbus 7. *Philos. T. Roy. Soc. A*, 296:219–241, 1980. doi: 10.1098/rsta.1980.0166.

E. Fehlberg. Some old and new runge-kutta formulas with stepsize control and their error coefficients. *Computing*, 34(3):265–270, 1985. ISSN 1436-5057. doi: 10.1007/BF02253322.

C. FitzGerald. Optimal indexing of the vertices of graphs. *Mathematics of Computation*, 28 (127):825–831, 1974. doi: 10.2307/2005704.

P. M. d. F. Forster and K. P. Shine. Radiative forcing and temperature trends from stratospheric ozone changes. *J. Geophys. Res.*, 102:10841–10855, 1997. doi: 10.1029/96JD03510.

F. Friedl-Vallon, T. Gulde, F. Hase, A. Kleinert, T. Kulessa, G. Maucher, T. Neubert, F. Olschewski, C. Piesch, P. Preusse, H. Rongen, C. Sartorius, H. Schneider, A. Schönfeld, V. Tan, N. Bayer, J. Blank, R. Dapp, A. Ebersoldt, H. Fischer, F. Graf, T. Guggenmoser, M. Höpfner, M. Kaufmann, E. Kretschmer, T. Latzko, H. Nordmeyer, H. Oelhaf, J. Orphal,

M. Riese, G. Schardt, J. Schillings, M. K. Sha, O. Suminska-Ebersoldt, and J. Ungermann. Instrument concept of the imaging Fourier transform spectrometer GLORIA. *Atmos. Meas. Tech.*, 7(10):3565–3577, 2014. doi: 10.5194/amt-7-3565-2014.

R. R. Garcia, D. Marsh, D. E. Kinnison, B. Boville, and F. Sassi. Simulations of secular trends in the middle atmosphere 1950-2003. *J. Geophys. Res.*, 112:D09301, 2007. doi: 10.1029/2006JD007485.

A. Gettelman, P. Hoor, L. L. Pan, W. J. Randel, M. I. Hegglin, and T. Birner. The extra tropical upper troposphere and lower stratosphere. *Rev. Geophys.*, 49:RG3003, 2011. doi: 10.1029/2011RG000355.

J. C. Gille and J. M. Russel III. The limb infrared monitor of the stratosphere: Experiment description, performance, and results. *J. Geophys. Res.*, 89:5125–5140, 1984. doi: 10.1029/JD089iD04p05125.

J. C. Gille, J. J. Barnett, J. G. Whitney, M. A. Dials, D. Woodard, W. P. Rudolf, A. Lambert, and W. Mankin. The High-Resolution Dynamics Limb Sounder (HIRDLS) experiment on AURA. *Proc. SPIE*, 5152:161–171, 2003. doi: 10.1117/12.507657.

W. L. Godson. The evaluation of infra-red radiative fluxes due to atmospheric water vapour. *Quart. J. Roy. Meteorol. Soc.*, 79:367–379, 1953.

G. Golub. *Matrix computations.* Johns Hopkins University Press, Baltimore, 1996. ISBN 9780801854149.

L. L. Gordley and J. M. Russell. Rapid inversion of limb radiance data using an emissivity growth approximation. *Appl. Optics*, 20:807–813, 1981. doi: 10.1364/AO.20.000807.

G. Günther, R. Müller, M. von Hobe, F. Stroh, P. Konopka, and C. M. Volk. Quantification of transport across the boundary of the lower stratospheric vortex during arctic winter 2002/2003. *Atmos. Chem. Phys.*, 8(13):3655–3670, 2008. doi: 10.5194/acp-8-3655-2008.

M. Hanke. *Conjugate gradient type methods for ill-posed problems.* John Wiley & Sons, 1995.

P. C. Hansen and D. P. O'Leary. The use of the L-curve in the regularization of discrete ill-posed problems. *SIAM J. Sci. Comput.*, 14(6):1487–1503, 1993. doi: 10.1137/0914086.

P. Haynes and J. Anglade. The vertical scale cascade in atmospheric tracers due to large-scale differential advection. *J. Atmos. Sci.*, 54:1121–1136, 1997.

M. R. Hestenes and E. Stiefel. Methods of conjugate gradients for solving linear systems. *J Res NIST*, 49(6):409–436, 1952. doi: 10.6028/jres.049.044.

L. Hoffmann. Schnelle Spurengasretrieval für das Satellitenexperiment Envisat MIPAS. Technical Report JUEL-4207, Forschungszentrum Jülich, Jülich, Germany, 2006. ISSN 0944-2952.

L. Hoffmann, M. Kaufmann, R. Spang, R. Müller, J. J. Remedios, D. P. Moore, C. M. Volk, T. von Clarmann, and M. Riese. Envisat MIPAS measurements of CFC-11: retrieval, validation, and climatology. *Atmos. Chem. Phys.*, 8:3671–3688, 2008. doi: 10.1016/j.asr.2005.03.112.

J. R. Holton, P. H. Haynes, M. E. McIntyre, A. R. Douglass, R. B. Rood, and L. Pfister. Stratosphere-troposphere exchange. *Rev. Geophys.*, 33:403–439, 1995.

P. Hoor, H. Fischer, L. Lange, J. Lelieveld, and D. Brunner. Seasonal variations of a mixing layer in the lowermost stratosphere as identified by the co-o_3 correlation from in situ measurements. *J. Geophys. Res.*, 107(D5):4004, 2002. doi: 10.1029/2000JD000289.

L. Jaeglé, D. J. Jacob, Y. Wang, A. J. Weinheimer, B. A. Ridley, T. L. Campos, G. W. Sachse, and D. E. Hagen. Sources and chemistry of nox in the upper troposphere over the united states. *Geophys. Res. Lett.*, 25(10):1705–1708, 1998. doi: 10.1029/97GL03591.

M. N. Juckes and M. E. McIntyre. A high-resolution one-layer model of breaking planetary waves in the stratosphere. *Nature*, 328:590–595, 1987.

Jülich Supercomputing Centre. JURECA: General-purpose supercomputer at Jülich Supercomputing Centre. *Journal of large-scale research facilities*, 2(A62), 2016. doi: 10.17815/jlsrf-2-121.

L. Krasauskas, J. Ungermann, S. Ensmann, I. Krisch, E. Kretschmer, P. Preusse, and M. Riese. 3-D tomographic limb sounder retrieval techniques: irregular grids and Laplacian regularisation. *Atmos. Meas. Tech.*, 12(2):853–872, 2019. doi: 10.5194/amt-12-853-2019.

I. Krisch, P. Preusse, J. Ungermann, A. Dörnbrack, S. D. Eckermann, M. Ern, F. Friedl-Vallon, M. Kaufmann, H. Oelhaf, M. Rapp, C. Strube, and M. Riese. First tomographic observations of gravity waves by the infrared limb imager gloria. *Atmos. Chem. Phys.*, 17 (24):14937–14953, 2017. doi: 10.5194/acp-17-14937-2017.

A. Kullmann, M. Riese, F. Olschewski, F. Stroh, and K. U. Grossmann. Cryogenic Infrared Spectrometers and Telescopes for the Atmosphere - New Frontiers. In *Proc. SPIE*, volume 5570, pages 423–432, 2004. doi: 10.1117/12.564856.

D. Kunkel, P. Hoor, T. Kaluza, J. Ungermann, B. Kluschat, A. Giez, H.-C. Lachnitt, M. Kaufmann, and M. Riese. Evidence of small-scale quasi-isentropic mixing in ridges of extratropical baroclinic waves. *Atmos. Chem. Phys.*, 19(19):12607–12630, 2019. doi: 10.5194/acp-19-12607-2019.

A. Kunz, P. Konopka, R. Müller, and L. L. Pan. Dynamical tropopause based on isentropic potential vorticity gradients. *J. Geophys. Res. Atmos.*, 116(D1), 2011. doi: 10.1029/2010JD014343.

S. Lim and L. Teo. Generalized Whittle–Matérn random field as a model of correlated fluctuations. *Journal of Physics A: Mathematical and Theoretical*, 42(10):105202, 2009.

N. J. Livesey and W. G. Read. Direct retrieval of line-of-sight atmospheric structure from limb sounding observations. *Geophys. Res. Lett.*, 27:891–894, 2000.

D. W. Marquardt. An algorithm for least-squares estimation of nonlinear parameters. *J. Soc. Ind. Appl. Math.*, 11:431–441, 1963.

M. E. McIntyre and T. N. Palmer. Breaking planetary waves in the stratosphere. *Nature*, 305:593–600, 1983.

M. E. McIntyre and T. N. Palmer. The "surf zone" in the stratosphere. *J. Atm. Terr. Phys.*, 46:825–849, 1984.

D. S. McKenna, P. Konopka, J.-U. Grooß, G. Günther, R. Müller, R. Spang, D. Offermann, and Y. Orsolini. A new chemical lagrangian model of the stratosphere (CLaMS) 1. formulation of advection and mixing. *J. Geophys. Res.*, 107, 2002. doi: 10.1029/2000JD000114.

M. G. Mlynczak. Energetics of the mesosphere and lower thermosphere and the SABER experiment. *Adv. Space Res.*, 20:1177–1183, 1997.

T. Narita, E. Wanke, M. Sato, T. Sakanoi, A. Kumada, M. Kamogawa, I. Hirohiko, S. Harada, T. Kameda, F. Tsuchiya, and E. Kaneko. A study of lightning location system (blitz) based on VLF sferics. *2018 34th International Conference on Lightning Protection (ICLP)*, pages 1–7, 2018.

S. Nesbitt, R. Zhang, and R. Orville. Seasonal and global NOx production by lightning estimated from the optical transient detector (OTD). *Tellus B*, 52:1206 – 1215, 11 2000. doi: 10.1034/j.1600-0889.2000.01121.x.

G. Nolet. Solving or resolving inadequate and noisy tomographic systems. *J. Comput. Phys.*, 61(3):463–482, 1985. ISSN 0021-9991. doi: 10.1016/0021-9991(85)90075-0.

D. Offermann, K.-U. Grossmann, P. Barthol, P. Knieling, M. Riese, and R. Trant. Cryogenic Infrared Spectrometers and Telescopes for the Atmosphere (CRISTA) experiment and middle atmosphere variability. *J. Geophys. Res.*, 104:16311–16325, 1999. doi: 10.1029/1998JD100047.

L. L. Pan, W. J. Randel, B. L. Gary, M. J. Mahoney, and E. J. Hintsa. Definitions and sharpness of the extratropical tropopause: A trace gas perspective. *J. Geophys. Res.*, 109: D23103, 2004. doi: 10.1029/2004JD004982.

L. L. Pan, W. J. Randel, J. C. Gille, W. D. Hall, B. Nardi, S. Massie, V. Yudin, R. Khosravi, P. Konopka, and D. Tarasick. Tropospheric intrusions associated with the sec-

ondary tropopause. *J. Geophys. Res. Atmos.*, 114, MAY 20 2009. ISSN 2169-897X. doi: 10.1029/2008JD011374.

F. Ploeger, G. Günther, P. Konopka, S. Fueglistaler, R. Müller, C. Hoppe, A. Kunz, R. Spang, J.-U. Grooß, and M. Riese. Horizontal water vapor transport in the lower stratosphere from subtropics to high latitudes during boreal summer. *J. Geophys. Res.*, 118(14):8111–8127, 2013. ISSN 2169-8996. doi: 10.1002/jgrd.50636.

L. M. Polvani and R. A. Plumb. Rossby wave breaking, microbreaking, filamentation, and secondary vortex formation: The dynamics of a perturbed vortex. *J. Atmos. Sci.*, 49: 462–476, 1992.

P. J. Popp, T. P. Marcy, R. S. Gao, L. A. Watts, D. W. Fahey, E. C. Richard, S. J. Oltmans, M. L. Santee, N. J. Livesey, L. Froidevaux, B. Sen, G. C. Toon, K. A. Walker, C. D. Boone, and P. F. Bernath. Stratospheric correlation between nitric acid and ozone. *J. Geophys. Res. Atmos.*, 114(D3), 2009. doi: 10.1029/2008JD010875.

G. A. Postel and M. H. Hitchman. A climatology of Rossby wave breaking along the subtropical tropopause. *J. Atmos. Sci.*, 56:359–373, 1999. doi: 10.1175/1520-0469(1999)056⟨0359:ACORWB⟩2.0.CO;2.

P. Preusse, S. D. Eckermann, and M. Ern. Transparency of the atmosphere to short horizontal wavelength gravity waves. *J. Geophys. Res.*, 113(D24104), 2008. doi: 10.1029/2007JD009682.

C. Price, J. Penner, and M. Prather. NOx from lightning: 1. Global distribution based on lightning physics. *J. Geophys. Res. Atmos.*, 102(D5):5929–5941, 1997. doi: 10.1029/96JD03504.

M. H. Proffitt, J. J. Margitan, K. K. Kelly, M. Loewenstein, J. R. Pdolske, and K. R. Chan. Ozone loss in the arctic polar vortex inferred from high-altitude aircraft measurements. *Nature*, 347:31–36, 1990.

M. Riese, R. Spang, P. Preusse, M. Ern, M. Jarisch, D. Offermann, and K. U. Grossmann. Cryogenic infrared spectrometers and telescopes for the atmosphere (CRISTA) data processing and atmospheric temperature and trace gas retrieval. *J. Geophys. Res.*, 104:349–367, 1999.

M. Riese, F. Ploeger, A. Rap, B. Vogel, P. Konopka, M. Dameris, and P. Forster. Impact of uncertainties in atmospheric mixing on simulated utls composition and related radiative effects. *J. Geophys. Res. Atmos.*, 117(D16):n/a–n/a, 2012. ISSN 2156-2202. doi: 10.1029/2012JD017751.

M. Riese, H. Oelhaf, P. Preusse, J. Blank, M. Ern, F. Friedl-Vallon, H. Fischer, T. Guggenmoser, M. Hoepfner, P. Hoor, M. Kaufmann, J. Orphal, F. Ploeger, R. Spang, O. Suminska-Ebersoldt, J. Ungermann, B. Vogel, and W. Woiwode. Gimballed Limb Observer for Radiance Imaging of the Atmosphere (GLORIA) scientific objectives. *Atmos. Meas. Tech.*, 7 (7):1915–1928, 2014. ISSN 1867-1381. doi: 10.5194/amt-7-1915-2014.

A. E. Roche, J. B. Kumer, J. L. Mergenthaler, G. A. Ely, W. G. Uplinger, J. F. Potter, T. C. James, and L. W. Sterritt. The cryogenic limb array etalon spectrometer (CLAES) on UARS: Experiment description and performance. *J. Geophys. Res.*, 98:10763–10775, 1993.

C. D. Rodgers. *Inverse Methods for Atmospheric Sounding: Theory and Practice*, volume 2 of *Series on Atmospheric, Oceanic and Planetary Physics*. World Scientific, Singapore, 2000.

J. M. Russell and S. R. Drayson. The inference of atmospheric ozone using satellite horizon measurements in the 1042 cm^{-1} band. *J. Atmos. Sci.*, 29:376–390, 1972.

Y. Saad. *Iterative Methods for Sparse Linear Systems*. S.I.A.M., Philadelphia, 2nd edition, 2003.

M. Salby. Survey of planetary-scale traveling waves - the state of theory and observations. *Rev. Geophys.*, 22(2):209–236, 1984. ISSN 8755-1209. doi: 10.1029/RG022i002p00209.

R. Scott and J. Cammas. Wave breaking and mixing at the subtropical tropopause. *J. Atmos. Sci.*, 59(15):2347–2361, 2002.

S. Skiena. *The algorithm design manual*. TELOS–the Electronic Library of Science, Santa Clara, CA, 1998. ISBN 9780387948607.

L. C. Sparling, J. C. Wei, and L. M. Avallone. Estimating the impact of small-scale variability in satellite measurement validation. *J. Geophys. Res.*, 111(D20), 2006. doi: 10.1029/2005JD006943.

T. Steck, M. Höpfner, T. von Clarmann, and U. Grabowski. Tomographic retrieval of atmospheric parameters from infrared limb emission observations. *Appl. Optics*, 44(16):3291–3301, 2005. doi: 10.1364/AO.44.003291.

A. Tarantola. *Inverse Problem Theory Methods for Data Fitting and Model Parameter Estimation*. Elsevier Science, 2013.

X. Tie, R. Zhang, G. Brasseur, L. Emmons, and W. Lei. Effects of lightning on reactive nitrogen and nitrogen reservoir species in the troposphere. *J. Geophys. Res. Atmos.*, 106 (D3):3167–3178, 2001. doi: 10.1029/2000JD900565.

A. N. Tikhonov and V. Y. Arsenin. *Solutions of ill-posed problems*. Winston, Washington D.C., USA, 1977.

J. Ungermann. Improving retrieval quality for airborne limb-sounders by horizontal regularisation. *Atmos. Meas. Tech.*, 6(1):15–32, 2013. doi: 10.5194/amt-6-15-2013.

J. Ungermann, L. Hoffmann, P. Preusse, M. Kaufmann, and M. Riese. Tomographic retrieval approach for mesoscale gravity wave observations by the PREMIER infrared limb-sounder. *Atmos. Meas. Tech.*, 3(2):339–354, 2010a. doi: 10.5194/amt-3-339-2010.

J. Ungermann, M. Kaufmann, L. Hoffmann, P. Preusse, H. Oelhaf, F. Friedl-Vallon, and M. Riese. Towards a 3-D tomographic retrieval for the air-borne limb-imager GLORIA. *Atmos. Meas. Tech.*, 3(6):1647–1665, 2010b. doi: 10.5194/amt-3-1647-2010.

J. Ungermann, J. Blank, J. Lotz, K. Leppkes, L. Hoffmann, T. Guggenmoser, M. Kaufmann, P. Preusse, U. Naumann, and M. Riese. A 3-D tomographic retrieval approach with ad-

vection compensation for the air-borne limb-imager GLORIA. *Atmos. Meas. Tech.*, 4(11): 2509–2529, 2011. doi: 10.5194/amt-4-2509-2011.

J. Ungermann, L. L. Pan, C. Kalicinsky, F. Olschewski, P. Knieling, J. Blank, K. Weigel, T. Guggenmoser, F. Stroh, L. Hoffmann, and M. Riese. Filamentary structure in chemical tracer distributions near the subtropical jet following a wave breaking event. *Atmos. Chem. Phys.*, 13(20):10517–10534, 2013. ISSN 1680-7316. doi: 0.5194/acp-13-10517-2013.

B. Vogel, G. Günther, R. Müller, J.-U. Grooß, A. Afchine, H. Bozem, P. Hoor, M. Krämer, S. Müller, M. Riese, C. Rolf, N. Spelten, G. P. Stiller, J. Ungermann, and A. Zahn. Long-range transport pathways of tropospheric source gases originating in Asia into the northern lower stratosphere during the asian monsoon season 2012. *Atmos. Chem. Phys.*, 16(23): 15301–15325, 2016. doi: 10.5194/acp-16-15301-2016.

T. von Clarmann, C. De Clercq, M. Ridolfi, M. Höpfner, and J.-C. Lambert. The horizontal resolution of MIPAS. *Atmos. Meas. Tech.*, 2:47–54, 2009. doi: 10.5194/amt-2-47-2009.

G. Voronoi. Nouvelles applications des paramètres continus à la théorie des formes quadratiques. Deuxième mémoire. Recherches sur les parallélloèdres primitifs. *Journal für die reine und angewandte Mathematik*, 1908(134), 1908. URL `https://www.degruyter.com/view/journals/crll/1908/134/article-p198.xml`.

D. Waugh, R. Plumb, R. Atkinson, M. Schoeberl, L. Lait, P. Newman, M. Loewenstein, D. Toohey, L. Avallone, C. Webster, et al. Transport out of the lower stratospheric arctic vortex by rossby wave breaking. *J. Geophys. Res. Atmos.*, 99(D1):1071–1088, 1994.

K. Weigel, M. Riese, L. Hoffmann, S. Hoefer, C. Kalicinsky, P. Knieling, F. Olschewski, P. Preusse, F. Stroh, R. Spang, and C. M. Volk. CRISTA-NF measurements during the AMMA-SCOUT-O_3 aircraft campaign. *Atmos. Meas. Tech.*, 3(2):1437–1455, 2010. doi: 10.5194/amt-3-1437-2010.

M. P. Weinreb and A. C. Neuendorffer. Method to apply homogeneous-path transmittance models to inhomogeneous atmospheres. *J. Atmos. Sci.*, 30:662–666, 1973. doi: 10.1175/1520-0469(1973)030⟨0662:MTAHPT⟩2.0.CO;2.

W. Woiwode, H. Oelhaf, T. Gulde, C. Piesch, G. Maucher, A. Ebersoldt, C. Keim, M. Höpfner, S. Khaykin, F. Ravegnani, A. E. Ulanovsky, C. M. Volk, E. Hösen, A. Dörnbrack, J. Ungermann, C. Kalicinsky, and J. Orphal. MIPAS-STR measurements in the arctic UTLS in winter/spring 2010: instrument characterization, retrieval and validation. *Atmos. Meas. Tech.*, 5(6):1205–1228, 2012. doi: 10.5194/amt-5-1205-2012.

A. Zahn, J. Weppner, H. Widmann, K. Schlote-Holubek, B. Burger, T. Kühner, and H. Franke. A fast and precise chemiluminescence ozone detector for eddy flux and airborne application. *Atmos. Meas. Tech.*, 5(2):363–375, 2012. doi: 10.5194/amt-5-363-2012.

R. Zhang, N. T. Sanger, R. E. Orville, X. Tie, W. Randel, and E. R. Williams. Enhanced NOx by lightning in the upper troposphere and lower stratosphere inferred from the UARS global NO2 measurements. *Geophys. Res. Lett.*, 27(5):685–688, 2000. doi: 10.1029/1999GL010903.

R. Zhang, X. Tie, and D. W. Bond. Impacts of anthropogenic and natural NOx sources over the U.S. on tropospheric chemistry. *Proc. Natl. Acad. Sci.*, 100(4):1505–1509, 2003. ISSN 0027-8424. doi: 10.1073/pnas.252763799.

M. Zöger, A. Afchine, N. Eicke, M. T. Gerhards, E. Klein, D. S. McKenna, U. Morschel, U. Schmidt, V. Tan, F. Tuitjer, T. Woyke, and C. Schiller. Fast in situ stratospheric hygrometers: A new family of balloon-borne and airborne lyman alpha photofragment fluorescence hygrometers. *J. Geophys. Res.*, 104(D1):1807–1816, 1999. doi: 10.1029/1998JD100025.

Band / Volume 592
Evaluation von Reaktorkonzepten für die CO_2-basierte Methanolsynthese aus Wasserstoff und Kohlendioxid mithilfe von CFD-Simulationen
S. Weiske (2022), x, 369 pp
ISBN: 978-3-95806-661-8

Band / Volume 593
Spectral Induced Polarization of Biochar in Soil
Z. Gao (2022), XXVI, 155 pp
ISBN: 978-3-95806-662-5

Band / Volume 594
Eignung von nickelhaltigen Katalysatorsystemen in sauren Medien zur Nutzung im Betrieb von Brennstoffzellen
A. Karaca (2022), iv, 249 pp
ISBN: 978-3-95806-663-2

Band / Volume 595
Seasonal Comparison of the Chemical Composition and Source Apportionment of Aerosols during the Year-Long JULIAC Campaign
L. Liu (2022), VIII, 189 pp
ISBN: 978-3-95806-668-7

Band / Volume 596
Nanoscale Understanding and Control of Metal Exsolution in Perovskite Oxides
M. L. Weber (2022), ix, 160 pp
ISBN: 978-3-95806-669-4

Band / Volume 597
Nanostructures of Transition Metal Sulfides for Anion Exchange Membrane Water Electrolysis
L. Xia (2022), 161 pp
ISBN: 978-3-95806-670-0

Band / Volume 598
Recycling- und Defossilisierungsmaßnahmen der Energieintensiven Industrie Deutschlands im Kontext von CO_2-Reduktionsstrategien
F. Kullmann (2022), XII, 237 pp
ISBN: 978-3-95806-672-4

Band / Volume 599
IEK-14 Report 2022
Research contributions for the energy transition and structural change in the Rhineland
B. Emonts (Ed.) (2022), 83 pp
ISBN: 978-3-95806-676-2

Band / Volume 600
Development of Glass-based Sealants for the Joining of Oxygen Transport Membranes
X. Li (2022), IV, 159 pp
ISBN: 978-3-95806-677-9

Band / Volume 601
High-resolution imaging of transport processes with GPR full-waveform inversion
P. Haruzi (2022), iv, 173 pp
ISBN: 978-3-95806-678-6

Band / Volume 602
Synthesis of optimized cathode materials for all-solid-state lithium batteries
C. Roitzheim (2022), xv, 221 pp
ISBN: 978-3-95806-679-3

Band / Volume 603
Development of components based on Ti_2AlC/fiber composites for aggressive environmental conditions
S. Badie (2023), x, 161 pp
ISBN: 978-3-95806-680-9

Band / Volume 604
Multiregionales Energiesystemmodell mit Fokus auf Infrastrukturen
T. M. Groß (2023), xx, 235 pp
ISBN: 978-3-95806-681-6

Band / Volume 605
Temporal Aggregation Methods for Energy System Modeling
M. A. C. Hoffmann (2023), XXVI, 341 pp
ISBN: 978-3-95806-683-0

Band / Volume 606
Examining transport in the Upper Troposphere – Lower Stratosphere with the infrared limb imager GLORIA
L. Krasauskas (2023), v, 107 pp
ISBN: 978-3-95806-691-5

Weitere ***Schriften des Verlags im Forschungszentrum Jülich*** unter
http://wwwzb1.fz-juelich.de/verlagextern1/index.asp

Energie & Umwelt / Energy & Environment
Band / Volume 606
ISBN 978-3-95806-691-5

Mitglied der Helmholtz-Gemeinschaft

JÜLICH
Forschungszentrum